

# INDUCER ANALYSIS/PUMP MODEL DEVELOPMENT

*IN-37-CR*  
*12614*  
*74 P*

**Contract No. NAS8-38868**

**Final Report**

Prepared for

National Aeronautics & Space Administration  
George C. Marshall Space Flight Center  
Marshall Space Flight Center, AL 35812

By

Gary C. Cheng

SECA, Inc.  
3313 Bob Wallace Ave., Suite 202  
Huntsville, AL 35805

March, 1994

N94-34963

Unclas

G3/37 0012614

(NASA-CR-196005) INDUCER  
ANALYSIS/PUMP MODEL DEVELOPMENT  
Final Report (SECA) 74 P

## ABSTRACT

Current design of high performance turbopumps for rocket engines requires effective and robust analytical tools to provide design information in a productive manner. The main goal of this study was to develop a robust and effective computational fluid dynamics (CFD) pump model for general turbopump design and analysis applications. A finite difference Navier-Stokes flow solver, FDNS, which includes an extended  $k-\epsilon$  turbulence model and appropriate moving zonal interface boundary conditions, was developed to analyze turbulent flows in turbomachinery devices. In the present study, three key components of the turbopump, the inducer, impeller, and diffuser, were investigated by the proposed pump model, and the numerical results were benchmarked by the experimental data provided by Rocketdyne. For the numerical calculation of inducer flows with tip clearance, the turbulence model and grid spacing are very important. Meanwhile, the development of the cross-stream secondary flow, generated by curved blade passage and the flow through tip leakage, has a strong effect on the inducer flow. Hence, the prediction of the inducer performance critically depends on whether the numerical scheme of the pump model can simulate the secondary flow pattern accurately or not. The impeller and diffuser, however, are dominated by pressure-driven flows such that the effects of turbulence model and grid spacing (except near leading and trailing edges of blades) are less sensitive. The present CFD pump model has been proved to be an efficient and robust analytical tool for pump design due to its very compact numerical structure (requiring small memory), fast turnaround computing time, and versatility for different geometries.

**TABLE OF CONTENTS**

<b>ABSTRACT</b> .....	<b>i</b>
<b>1.0 INTRODUCTION</b> .....	<b>1</b>
<b>2.0 NUMERICAL METHODOLOGY</b> .....	<b>3</b>
2.1 GOVERNING EQUATIONS .....	3
2.2 NUMERICAL SCHEMES .....	5
2.3 BOUNDARY CONDITIONS .....	9
<b>3.0 INDUCER FLOW STUDY</b> .....	<b>10</b>
3.1 INDUCER INLET FLOW .....	10
3.2 INDUCER FLOW .....	11
<b>4.0 CONSORTIUM IMPELLER FLOW STUDY</b> .....	<b>17</b>
4.1 BASELINE IMPELLER .....	17
4.2 ADVANCED CONCEPT IMPELLER .....	34
<b>5.0 SSME HPFTP IMPELLER FLOW STUDY</b> .....	<b>38</b>
<b>6.0 CONSORTIUM VANED DIFFUSER FLOW STUDY</b> .....	<b>50</b>
<b>7.0 CONCLUSIONS AND RECOMMENDATIONS</b> .....	<b>66</b>
<b>REFERENCES</b> .....	<b>69</b>

## 1.0 INTRODUCTIONS

In the past, the preliminary designs of pump components have relied on potential flow analysis tools and empirical data. Due to the ever increasing performance requirements of rocket engines, pump designs have been pushed beyond the envelop of past experience. A better analytical tool is therefore called for to provide flow field assessment in the design process before the full scale hardware is built and tested. The greatest challenge to the CFD pump model development is to obtain computation efficiency for complex geometries, turbulence effects, and large source terms generated by Coriolis and centrifugal forces. The complex geometry of the turbopump components, such as inducer, impeller, diffuser, and volute, poses a stringent requirement on numerical grid sizes and hence on the computing time. To provide a good prediction of turbopump efficiency and detailed flow structure, a CFD pump model not only needs to have an accurate numerical scheme which can simulate secondary flow patterns induced by the curved blade passage, but also is required to account for the effect of rotation and curvature on turbulence. Moreover, the presence of tip clearance leakage flows for the unshrouded pump challenges the capability and the validity of the existing turbulence models. Therefore, the capability of solving complex turbulent rotating flows efficiently is essential for an effective CFD pump model.

A pump consortium team, which consists of government research centers, industries, and universities, was organized by NASA/MSFC to establish data bases for code benchmarking, to exchange ideas, and to improve and verify numerical models for the advanced turbopump design. Tremendous effort has been made by members of the pump consortium to contribute, both numerically and experimentally to this study. Under this contract, SECA has been involved in the pump consortium activities and has conducted numerical studies of (1) a pump inducer designed by Rocketdyne, (2) the SSME HPFTP (High Pressure Fuel Turbopump) impeller, (3) a consortium designed impeller, and (4) a consortium designed vaned diffuser based on the proposed CFD pump model-- the FDNS code. The numerical results of these investigations are detailed in this report. Through extensive investigation, a better understanding of flow

characteristics in the turbopump has been reached, and thus suggestions were made to modify the pump design and to improve turbopump performance. Meanwhile, some recommendations to improve the present CFD pump model were proposed, based on these numerical studies in this report.

## 2.0 NUMERICAL METHODOLOGY

The framework of the proposed CFD pump model, FDNS, is a finite difference Navier-Stokes flow solver<sup>1-3</sup>, which employs a predictor plus multi-corrector pressure-based solution method so that compressible and incompressible flow problems can be analyzed by using the same method. High-order (second- or third-order) upwind or central difference schemes plus adaptive second-order and fourth-order dissipation terms are used to approximate the convection terms of the transport equations. Second-order central differencing schemes are used for the viscous and source terms of the governing equations. A vectorized point iteration matrix solver is currently employed to insure a stable and fast convergence rate. A multi-block, multi-zone capability is incorporated into the FDNS code such that problems with complex geometries can be analyzed efficiently. Furthermore, centrifugal and Coriolis forces are introduced into the momentum equations as source terms, and are solved implicitly for the computation of rotating machinery. An extended k-ε turbulence model<sup>4</sup> with a modified near-wall boundary treatment is utilized in the code as the base model for turbulent flow computations. The modified near-wall treatment, in which the near-wall velocity profile is approximated with Liakopoulos' wall damping function<sup>5</sup>, enables the numerical calculation to be less sensitive to the near-wall grid spacing. The employment of the current numerical scheme and turbulence model enables the FDNS code to be an efficient and robust pump model.

### 2.1 GOVERNING EQUATIONS

The FDNS code is employed to solve a set of nonlinear and coupled transport equations (Reynolds-averaged Navier-Stokes equations, and k-ε turbulence transport equations) in curvilinear coordinates. The system of governing equations can be generalized and expressed as

$$\frac{1}{J} \frac{\partial \rho \phi}{\partial t} = \frac{-\partial \rho U_i \phi}{\partial \xi_i} + \frac{\partial}{\partial \xi_i} \left[ \mu_e G_{ij} \frac{\partial \phi}{\partial \xi_j} \right] + S_q \quad (1)$$

where  $\rho$  and  $\phi$  ( $= 1, u, v, w, k,$  and  $\varepsilon$ ) denote the fluid density and the flow primitive variables for each governing equations.  $J$ ,  $U_i$  and  $G_{ij}$  represent the Jacobian of the coordinate transformation, volume-weighted contravariant velocities and diffusion metrics, respectively. Centrifugal and Coriolis forces are included in the source terms  $S_\phi$ , where the axis of rotation is assumed to be in the  $x$ -axis direction. The source terms  $S_\phi$  in the governing equations can be written as

$$S_\phi = \frac{1}{J} \left\{ \begin{array}{l} 0 \\ -P_x + \nabla[\mu_e(u_j)_x] - \frac{2}{3}(\mu_e \nabla u)_x \\ -P_y + \nabla[\mu_e(u_j)_y] - \frac{2}{3}(\mu_e \nabla u)_y + F_y \\ -P_z + \nabla[\mu_e(u_j)_z] - \frac{2}{3}(\mu_e \nabla u)_z + F_z \\ \rho(P_r - \varepsilon) \\ \frac{\rho \varepsilon}{k} [C_1 P_r - C_2 \varepsilon] + \frac{C_3 \rho P_r^2}{k} \end{array} \right. \quad (2)$$

$F_y$  ( $= 2w\Omega + y\Omega^2$ ) and  $F_z$  ( $= -2v\Omega + z\Omega^2$ ) are the forces in  $y$ - and  $z$ -axis directions, respectively, where  $\Omega$  denotes the rotational speed of a zone. Since eddy viscosity concept is employed in the proposed model, the effective viscosity  $\mu_e$  is defined as  $\mu_e = (\mu + \mu_t)/\sigma_\phi$ , where  $\mu$  and  $\mu_t$  are the fluid viscosity and turbulence eddy viscosity.  $\sigma_\phi$  denotes the modeling constant for the governing equations, and its value is given in Table 1.

Table 1  $\sigma_\phi$  Values of the Governing Equations

Governing Equations	Laminar	Turbulent
Momentum Equation	1.0	1.0
k-equation (standard)	---	0.89
$\varepsilon$ -equation (standard)	---	1.15

In the  $k$ - $\varepsilon$  model, the turbulence eddy viscosity  $\mu_t$  is correlated as  $\mu_t = \rho C_\mu k^2/\varepsilon$ , and  $C_\mu = 0.09$ . In the present study, the extended  $k$ - $\varepsilon$  model<sup>4</sup> were used as the baseline model, in which the modeling constants are tuned to be  $C_1 = 1.15$ ,  $C_2 = 1.92$  and  $C_3 = 0.25$ . The extended  $k$ - $\varepsilon$  model has shown the capability of providing good predictions for complex turbulent flows such as mixing shear layers, and effects of curvature and separation<sup>4,6</sup>.  $P_r$  stands for the turbulence kinetic energy production rate and is calculated in a full form, which can be expressed as

$$P_r = \frac{\mu_t}{\rho} \left\{ \frac{1}{2} \left[ \frac{\partial u_j}{\partial x_i} + \frac{\partial u_i}{\partial x_j} \right]^2 - \frac{2}{3} \left[ \frac{\partial u_k}{\partial x_k} \right]^2 \right\} \quad (3)$$

A modified wall function approach is employed to provide good near-wall approximation which is less sensitive to the near-wall grid spacing. Unlike the conventional wall function treatment, in which the non-dimensionalized quantities ( $y^+ \equiv \rho u_\tau y/\mu$  and  $u^+ \equiv u/u_\tau$ ) are not well defined in regions with flow separation, the present approach adopts the profile of the non-dimensionalized velocity  $u^+$  suggested by Liakopoulos<sup>5</sup>. The formulation for the wall function can be expressed as

$$u^+ = \ln \left[ \frac{(y^+ + 11)^{4.02}}{(y^{+2} - 7.37y^+ + 83.3)^{0.79}} \right] + 5.63 \tan^{-1}(0.12y^+ - 0.441) - 3.81 \quad (4)$$

This velocity profile provides a smooth transition between logarithmic law of the wall and linear viscous sublayer variation. Based on the profile, the turbulent shear stress and near-wall turbulence energy production rate can be calculated properly.

## 2.2 NUMERICAL SCHEMES

In the proposed model, finite difference approximations are employed to discretize the transport equations on non-staggered grid systems. The FDNS code utilizes a second-order time-centered or an implicit Euler time-marching scheme to solve the transient or steady state flow problems. For the space discretization, upwind/central difference scheme plus adaptive dissipation terms are adopted to model the convection term; while second-order central

difference schemes are used for viscous and source terms. There are three types of upwind difference schemes: first, second, and third order, coded in the FDNS. However, a first-order upwind scheme is designated for the convection term of the transport equation of positive-definite scalar quantities (e.g. turbulence quantities). The adaptive dissipation terms are controlled by the flow field, and can be switched to either second order or third order. In this approach, a fourth-order damping is activated in smooth flow regions, while a second-order damping (becomes a first-order upwind scheme) is used near flow discontinuities such as flows through shocks. Hence, the stability of this damping scheme improves the computation convergence.

To demonstrate this methodology, the convection flux in the  $\xi$ -axis direction, in Eq. (1), can be discretized as

$$\frac{\partial \rho U_i \phi}{\partial \xi} = (F_{i+1/2} - F_{i-1/2}) - \alpha_d (d_{i+1/2} - d_{i-1/2}) \quad (5)$$

In Eq. (5), the first term on the right hand side represents the baseline first-order upwind difference scheme in which the second-order damping terms are added. That is

$$F_{i+1/2} = 0.5 [(\rho U)_{i+1/2} + |\rho U|_{i+1/2}] \phi_i + 0.5 [(\rho U)_{i+1/2} - |\rho U|_{i+1/2}] \phi_{i+1} \quad (6a)$$

$$F_{i-1/2} = 0.5 [(\rho U)_{i-1/2} + |\rho U|_{i-1/2}] \phi_{i-1} + 0.5 [(\rho U)_{i-1/2} - |\rho U|_{i-1/2}] \phi_i \quad (6b)$$

The second term on the right hand side of Eq. (5) is the adaptive dissipation term, which includes the fourth-order dissipation term (D) and the anti-damping term (A) which is employed to achieve high-order upwind or central difference schemes. The presence of the adaptive dissipation term is controlled by the shock monitoring parameter,  $\alpha_d$ , which is defined as

$$\alpha_d = \max [0, 1 - 25 \max (\alpha_{i-1}, \alpha_i, \alpha_{i+1})] \quad (7)$$

$$\text{where } \alpha_i = \frac{p_{i-1} - 2p_i + p_{i+1}}{p_{i-1} + 2p_i + p_{i+1}}$$

It can be easily seen that  $\alpha_d$  will have a value of zero whenever a very large pressure gradient occurs, and thus the baseline first-order upwind difference scheme would be utilized. The adaptive dissipation term is modeled as

$$d_{i+1/2} = 0.5 |\rho U|_{i+1/2} [\alpha_u A_{i+1/2} + 0.25 D_{i+1/2}] \quad (8a)$$

$$d_{i-1/2} = 0.5 |\rho U|_{i-1/2} [\alpha_u A_{i-1/2} + 0.25 D_{i-1/2}] \quad (8b)$$

where

$$\begin{aligned} D_{i+1/2} &= -[\phi_{\xi\xi\xi}]_{i+1/2} = 2\Delta\phi_{i+1/2} - \Delta\phi_{i+3/2} - \Delta\phi_{i-1/2} \\ D_{i-1/2} &= -[\phi_{\xi\xi\xi}]_{i-1/2} = 2\Delta\phi_{i-1/2} - \Delta\phi_{i+1/2} - \Delta\phi_{i-2/3} \\ \text{and } \Delta\phi_{i+1/2} &= \phi_{i+1} - \phi_i; \Delta\phi_{i-1/2} = \phi_i - \phi_{i-1}; \text{ etc.} \end{aligned} \quad (9)$$

In Eqs. (8),  $\alpha_u$  is a user-specified parameter to select a high-order upwind or a second-order central difference scheme. The anti-damping term (A) can be in different forms such that it can be combined with the baseline first-order upwind difference scheme to obtain high-order upwind difference schemes or a second-order central difference scheme. For example, to simulate a second-order upwind difference scheme, the anti-damping term will be formed as

$$A_{i+1/2} = \begin{cases} -\Delta\phi_{i-1/2}, & \text{if } U_{i+1/2} > 0 \\ -\Delta\phi_{i+3/2}, & \text{if } U_{i+1/2} < 0 \end{cases} \quad (10a)$$

$$A_{i-1/2} = \begin{cases} -\Delta\phi_{i-3/2}, & \text{if } U_{i-1/2} > 0 \\ -\Delta\phi_{i+1/2}, & \text{if } U_{i-1/2} < 0 \end{cases} \quad (10b)$$

To approximate the third-order upwind difference scheme, the anti-damping term will be expressed as:

$$A_{i+1/2} = \begin{cases} -\frac{2}{3} \Delta \phi_{i+1/2} - \frac{1}{3} \Delta \phi_{i-1/2}, & \text{if } U_{i+1/2} > 0 \\ -\frac{2}{3} \Delta \phi_{i+1/2} - \frac{1}{3} \Delta \phi_{i+3/2}, & \text{if } U_{i+1/2} < 0 \end{cases} \quad (11a)$$

$$A_{i-1/2} = \begin{cases} -\frac{2}{3} \Delta \phi_{i-1/2} - \frac{1}{3} \Delta \phi_{i-3/2}, & \text{if } U_{i-1/2} > 0 \\ -\frac{2}{3} \Delta \phi_{i-1/2} - \frac{1}{3} \Delta \phi_{i+1/2}, & \text{if } U_{i-1/2} < 0 \end{cases} \quad (11b)$$

However, if the second-order central difference scheme is selected, then the anti-damping term is formulated as

$$A_{i+1/2} = -\Delta \phi_{i+1/2}; \text{ and } A_{i-1/2} = -\Delta \phi_{i-1/2} \quad (12)$$

A pressure based solution procedure is employed in the present flow solver. The momentum equations and other necessary transport equations (e.g. turbulence transport equations) are first solved in the predictor step, and then the pressure is updated in the correction equation. The pressure-correction equation is constructed by combining a simplified momentum equation and the continuity equation, which can be expressed as

$$\frac{1}{RT} \frac{\partial p'}{\partial t} + \frac{\partial}{\partial x_i} \left[ \frac{u_i^n}{RT} p' \right] - \frac{\partial}{\partial x_i} \left[ \beta D_p \frac{\partial p'}{\partial x_i} \right] = -\frac{\partial \rho^n}{\partial t} - \frac{\partial}{\partial x_i} (\rho u_i^n) \quad (13)$$

where  $p' = p^{n+1} - p^n$  is the pressure correction,  $R$  is the gas constant, and  $\beta$  is a pressure-correction relaxation parameter. The superscripts  $n$  and  $n+1$  represent the current and the next time levels, respectively.  $D_p$  is proportional to the magnitude of the matrix coefficients of the momentum equations for a given grid point. An adaptive dissipation term, similar to that in the momentum equations, is also added into the pressure-correction equation to reduce oscillations of pressure near areas with large pressure gradients. After the solution of Eq. (13) is obtained, the pressure field will be updated, and the velocity field is then modified based on

$$u_i' = u_i^{n+1} - u_i^n \approx -\beta D_p \frac{\partial p'}{\partial x_i} \quad (14)$$

For the multi-corrector procedure, the above correction steps are repeated for few times to ensure a divergence-free flow field at the end of each time-marching step.

### 2.3 BOUNDARY CONDITIONS

The proposed CFD model is equipped to treat various type of boundary conditions such as inlet, outlet, symmetry (non-slip), periodic, freestream, singularity line, solid wall (with/without transpiration), and zonal interface boundary conditions. In the present pump model, the periodic boundary condition is treated explicitly, i.e. the circumferential velocity at the periodic boundary is extrapolated from the interior points, calculated from the matrix solver of the governing equations, due to the coupling effect of the two components of the circumferential velocity in the Cartesian coordinates. It was found from the present study that the explicit treatment may cause some oscillation in numerical convergence, and some possible improvement will be stated later in this report. At the subsonic or incompressible inlet boundaries, only pressure waves are extrapolated upstream. For exit boundaries, all variables are extrapolated downstream in the first step. This is typical treatment for supersonic outlets. Next, for subsonic or incompressible outlet boundaries, two options are provided: 1) to perform exit velocity corrections based on the global mass conservation condition; and 2) to assign a pressure profile at the exit boundary for a given outlet/inlet pressure ratio. In the present study, the first method was used for all test cases.

### 3.0 INDUCER FLOW STUDY

The first test case for the present CFD pump model was to benchmark an unshrouded inducer of Rocketdyne with a design flow coefficient of 0.3<sup>7</sup>. Key parameters of this test case are summarized in Table 2. Water was used as the working medium. The inducer upstream boundary conditions, such as boundary layer thickness and turbulence intensity level, are very critical in the numerical calculation of this type of flow field, and were not well defined in the test program. Hence, an axisymmetrical inducer inlet flow study was conducted by assuming a fully developed turbulent pipe flow condition far upstream.

Table 2 Design Parameters of the Inducer Flow Study

Inlet Flow Coefficient	0.3
Number of Blades	6
Tip Diameter (inches)	6.0
Radial Tip Clearance (inches)	0.008
Design Flow (GPM)	2236
Design Rotating Speed (rpm)	2600
Inlet Hub Diameter (inches)	1.8
Averaged inlet Axial Velocity (ft/sec)	28.274
Reynolds Number (per inch)	$1.917 \times 10^5$

### 3.1 INDUCER INLET FLOW

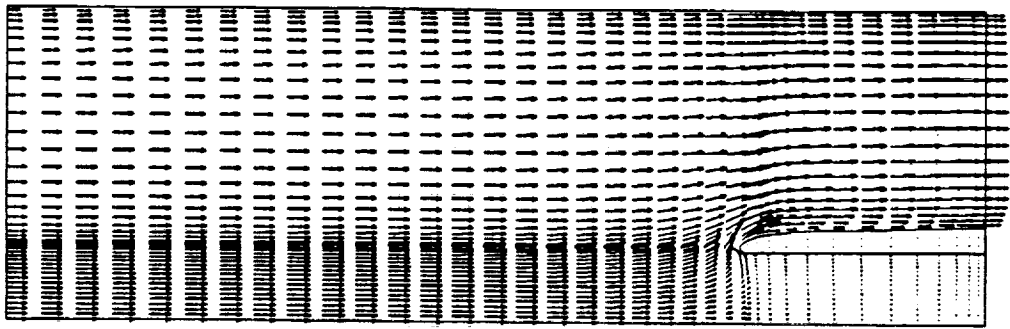
The rotating hub and bull-nose cavity geometry, located upstream of inducer blades, were modeled in the computation to properly simulate inlet flow conditions to the inducer. A 191 x 81 mesh system was employed to describe the inlet upstream section. The numerical result for

the inlet pipe flow to the inducer is plotted as shown in Figure 1. Numerical solutions near the exit of this analysis were then used as the inducer inlet flow boundary conditions. The inlet boundary in the computational domain for the inducer calculation was located half way between the leading edge of the inducer blade and the lip of the bull nose. The velocity and turbulence kinetic energy profiles at the inlet plane were computed and plotted as shown in Figure 2.

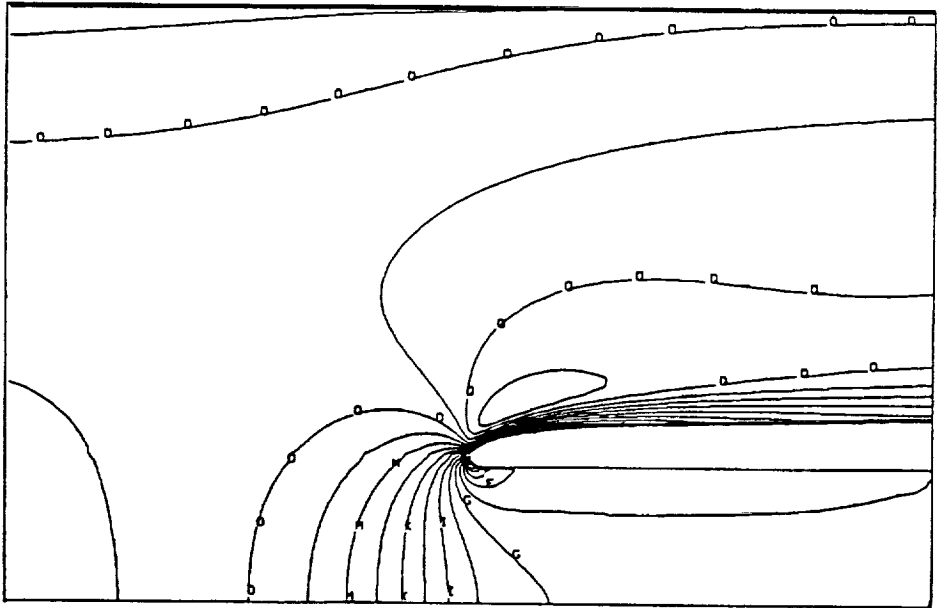
### 3.2 INDUCER FLOW

A 71 x 41 x 35 mesh system was constructed to represent a blade-to-blade passage, which is considered to be coarse for the rotating flow with tip clearance. A small tip clearance region was included and was resolved by six grid points in radial direction. A periodic boundary condition in the circumferential direction was imposed to avoid modeling the full geometry. The numerical result obtained by the proposed CFD model is shown in Figure 3, in which flow velocity vectors are plotted in the unwrapped view. The predicted result was also compared to the experimental data which were measured at four different axial planes, and various radial locations at each axial plane, as indicated in Figure 4. The comparison of calculated and measured axial velocity profile at these four sections are shown in Figure 5. The results of this study were also detailed in Ref. 3 and 8. The predicted velocity distributions show good agreement with test data. However, discrepancies occurred in the data comparisons for downstream sections, D and A, which were caused by inadequate representations of the inducer tip leakage flow and of the wake flow downstream of the trailing edge. One of the discrepancies is the shift in the wake locations which may be due to different angular clocking between the CFD solution and the experimental measurements. This concern is due to the fact that there are some uncertainties about the LDV measurement at the inducer trailing edge. Therefore, the test data were found to be suitable for only a qualitative evaluation of numerical models. The predicted magnitude of the wake can be further improved through grid refinement as indicated by a fine grid solution performed by Rocketdyne<sup>9</sup>. However, the tip leakage flow representations may require better treatment of the turbulence model, and more grid points in the tip clearance region. Fortunately, the overall inducer performance (e.g. head rise and efficiency) was not greatly influenced by the tip leakage flow. This is usually true for inducers

with thin blades and small tip clearances. The averaged predicted inducer efficiency of 0.89 compares well with the data calculated value of 0.95.

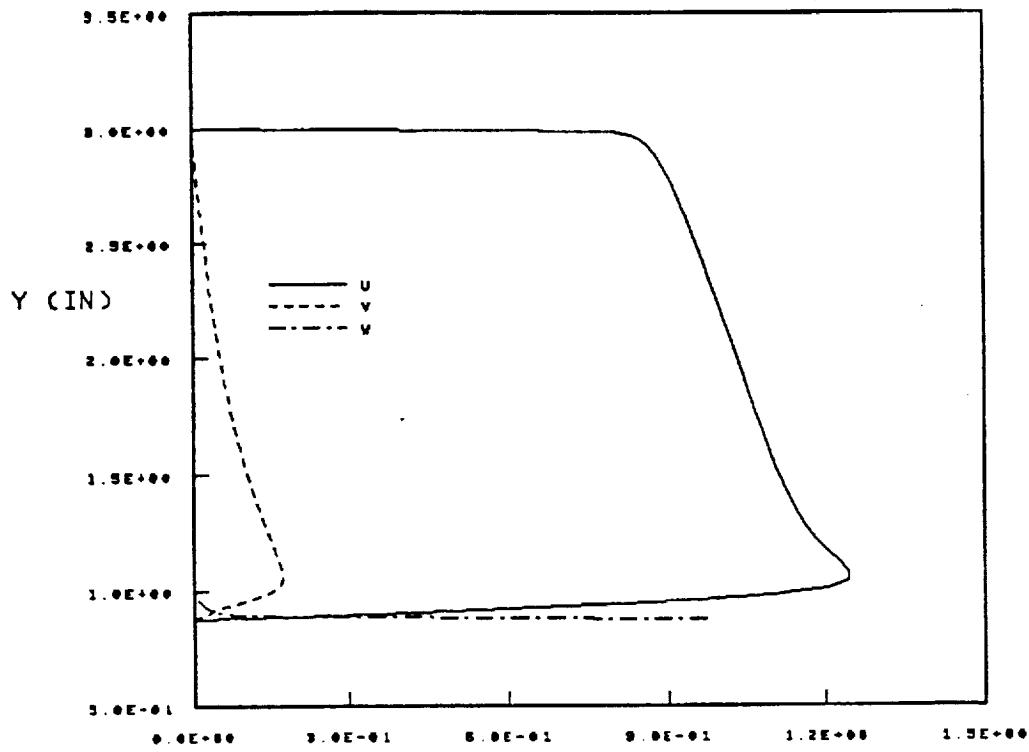


(a) Velocity Vectors

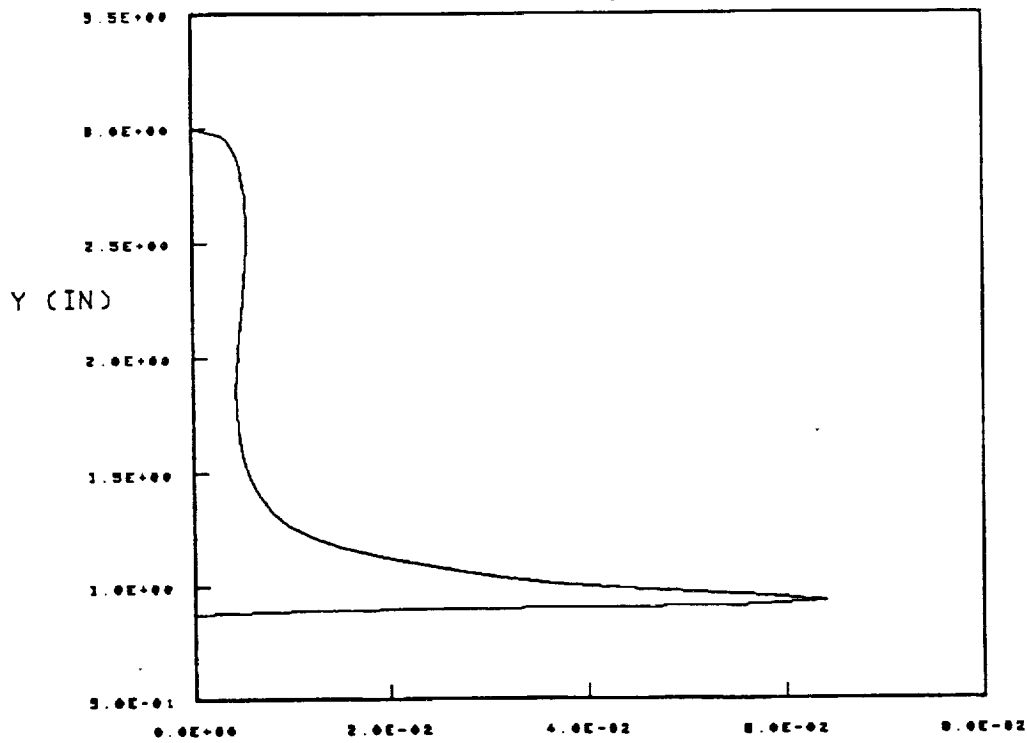


(b) Axial Velocity Contours

Figure 1 The Flowfield of the Inducer Upstream Pipe Flow Study (Axisymmetric)

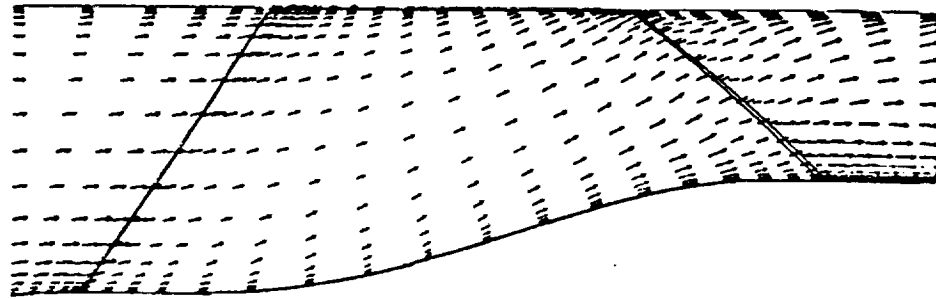


(a) Velocity Profile

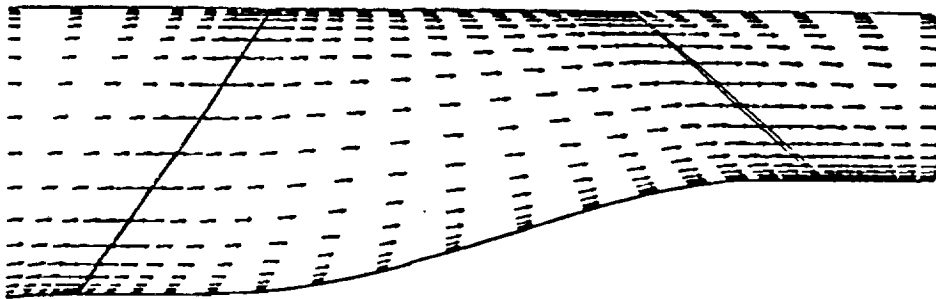


(b) Turbulence Kinetic Energy Profile

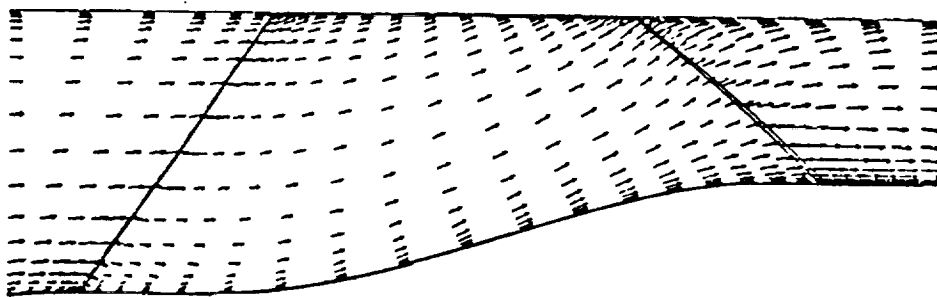
Figure 2 Inlet Boundary Conditions for the Inducer Flow Study



(a) Near Pressure Side



(b) At the Mid Plane



(c) Near Suction Side

Figure 3 Velocity Vectors along the Inducer Passage

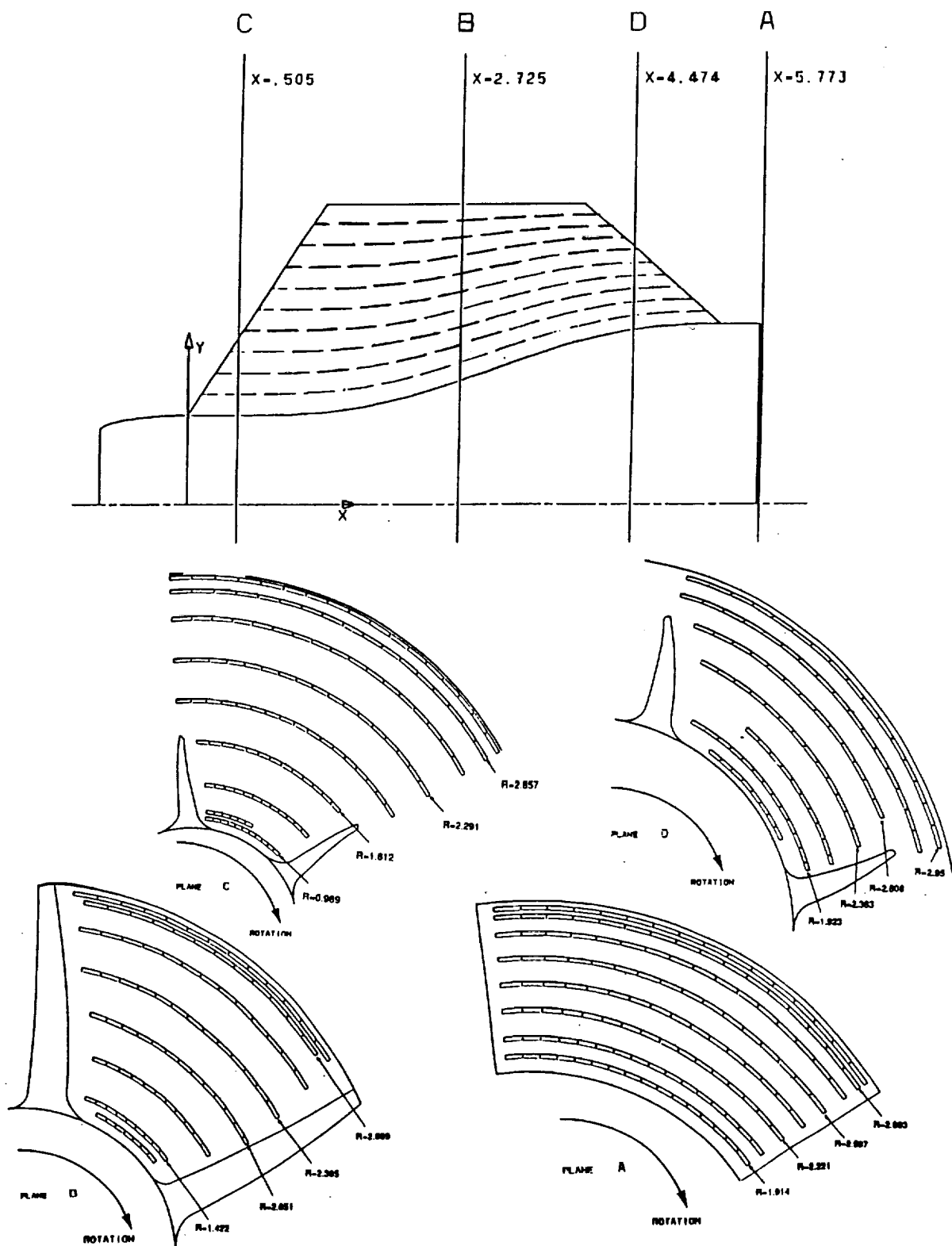
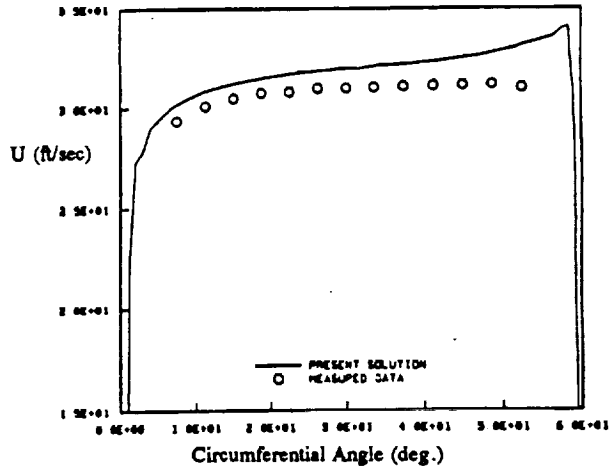
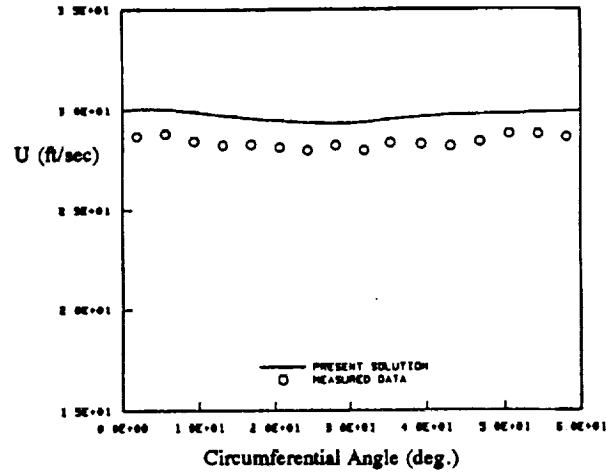


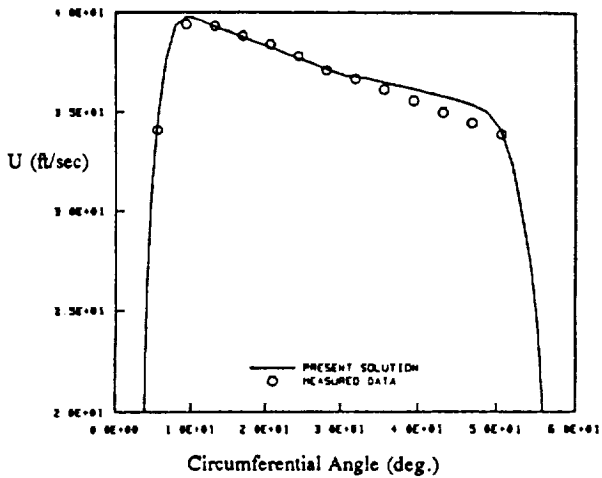
Figure 4 Sketch of the Data Measurement Planes of the Inducer Flow Study



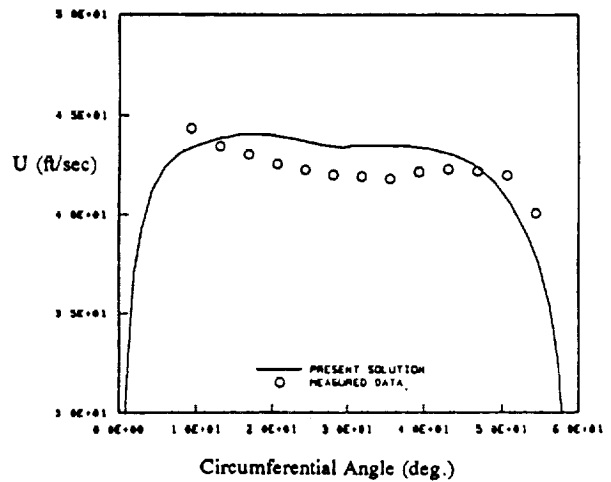
(a) Plane C, R = 1.12 in.



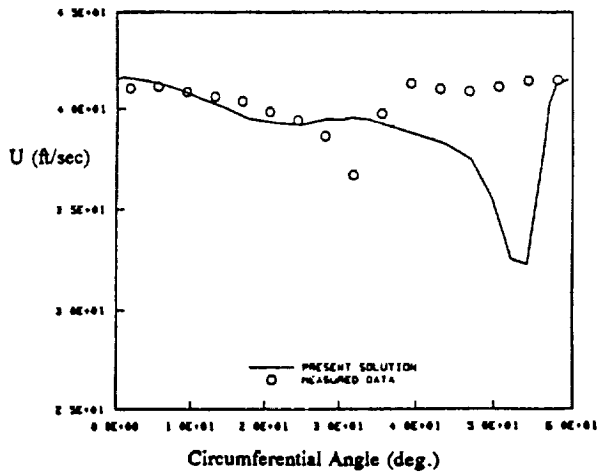
(b) Plane C, R = 2.291 in.



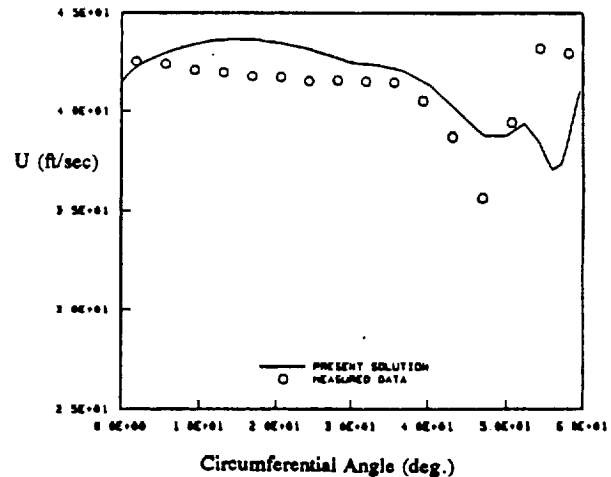
(c) Plane B, R = 2.051 in.



(d) Plane D, R = 2.068 in.



(e) Plane A, R = 1.914 in.



(f) Plane A, R = 2.587 in.

Figure 5 Data Comparisons of Meridional Velocity for the Inducer Flow Study

## 4.0 CONSORTIUM IMPELLER FLOW STUDY

The pump consortium designed a baseline impeller (shrouded) with the basic layout listed as shown in Table 3, and utilized CFD analyses of the baseline impeller from the consortium members to provide the guideline for design improvement. Several numerical studies were conducted for the baseline impeller such as the effect of boundary conditions, and geometry modifications, and some conclusions for design modification were then obtained. Based on the recommendation, an advanced concept impeller was designed and tested by the pump consortium.

Table 3 Configuration and Operating Conditions of the Consortium Impeller

Number of Full Blades/Partial Blades	6/6
Shaft Speed	6322 rpm
Exit Tip Diameter	9.045 inches
Inlet Hub Diameter	3.9 inches
Inlet Tip Diameter	6.0 inches
Mass Flow Rate	160.8 lb/sec

### 4.1 BASELINE IMPELLER

At the beginning of numerical analyses for the baseline impeller, the boundary conditions at the hub and the shroud surfaces downstream of the impeller blades were not well defined due to the presence of a downstream cavity. Hence, numerical computations of the baseline impeller were performed to investigate the effect of various upstream and downstream hub/shroud boundary conditions.

### Boundary Condition Effect

There were five test cases to examine the boundary condition effect, and they are listed in Table 4, where the hub surface in the upstream section to the impeller blade has a rotating wall boundary condition. A single zone, 103 x 23 x 30 mesh system as shown in Figure 6 was employed for the baseline impeller in these analyses. Simulated inlet velocity profiles, calculated based on a 1-D Euler solution of the upstream inducer flow, were utilized in these analyses. The results from these numerical studies confirmed that the upstream and downstream hub/shroud surface boundary conditions have prominent effects on the flow structure inside the impeller passage. Especially the inlet shroud boundary condition greatly affects the inlet flow velocities and flow angles entering the impeller blade passages. The inlet rotating wall boundary condition introduced a larger flow angle entering the impeller passage such that the pressure surface was more highly loaded and the flow separated more severely near the suction surface. The flow reversal on the suction surface thus created a blockage effect near the shroud such that the flow was push towards the hub and caused a more non-uniform impeller exit flow. Hence, in case 3 the mass flow rate through the suction side was reduced, and caused a more non-uniform flow split at the impeller exit. This can be easily seen from the flow split between the suction and pressure sides at the exit of impeller full blades, which is summarized in Table 5. The dominant effect of inlet shroud boundary condition also can be seen in Figures 7-8, the plots of meridional velocity and relative flow angle along the hub and shroud surfaces, which clearly shows there are two distinct trends for two different inlet shroud conditions (cases 1-2 vs. cases 3-5). The detailed flowfields of these numerical analyses were reported in Ref. 10, and some of them were plotted as shown in Figures 9-12. However, the effect on the overall impeller performance is minor as shown in Figure 13. The boundary conditions, including rotating wall and fixed wall for upstream hub and shroud surfaces, respectively, and slip boundary for downstream hub and shroud surfaces, were selected to be a better combination for the numerical simulation of the consortium impeller. The numerical analyses of the consortium impeller herein were conducted based on this set of boundary conditions.

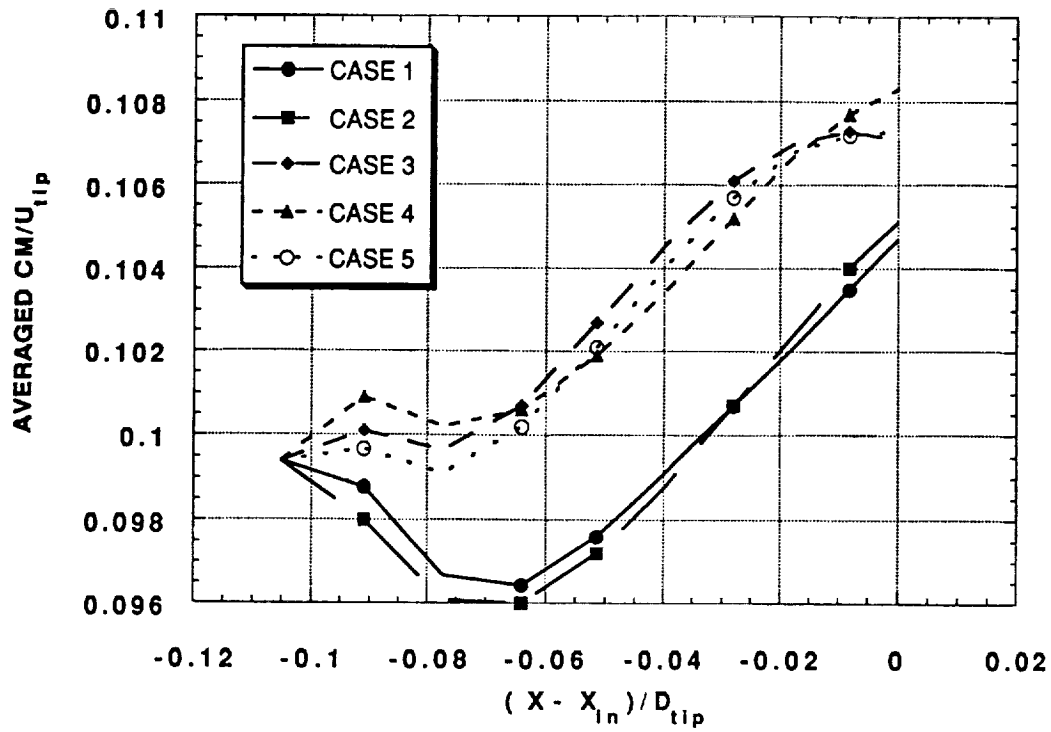
Table 4 Baseline Impeller Upstream/downstream Hub/Shroud Boundary Conditions

		Downstream Hub/Shroud Surfaces		
		Fixed Wall	Rotating Wall	Slip Surface
Upstream Shroud Surface	Fixed Wall	Case 1	N/A	Case 2
	Rotating Wall	Case 3	Case 4	Case 5

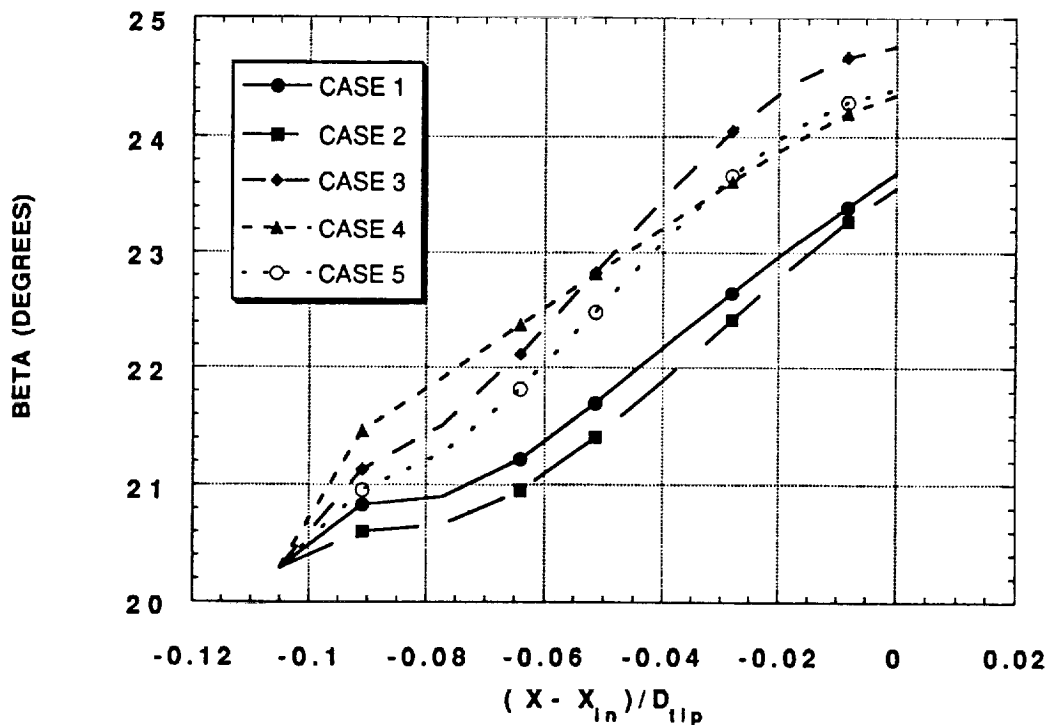
Table 5 Exit Flow Split of the Consortium Baseline Impeller with Various Boundary Conditions

	Case 1	Case 2	Case 3	Case 4	Case 5
Suction/Pressure	50.4/49.6	49/51	43.2/56.8	42.4/57.6	40.6/59.4



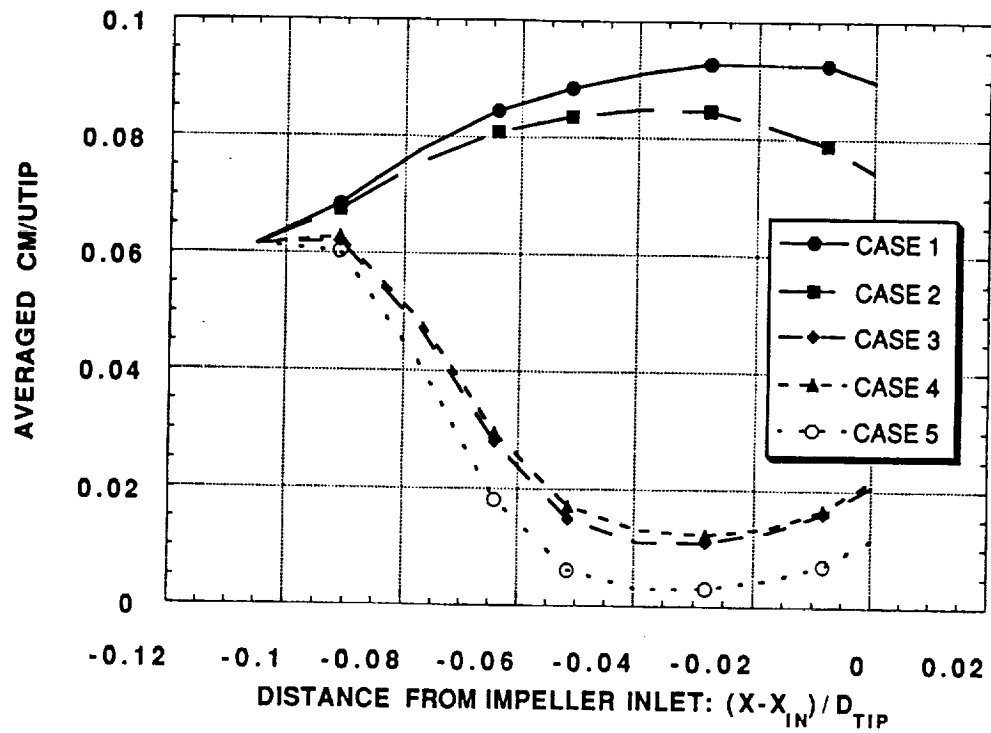


(a) Meridional Velocity

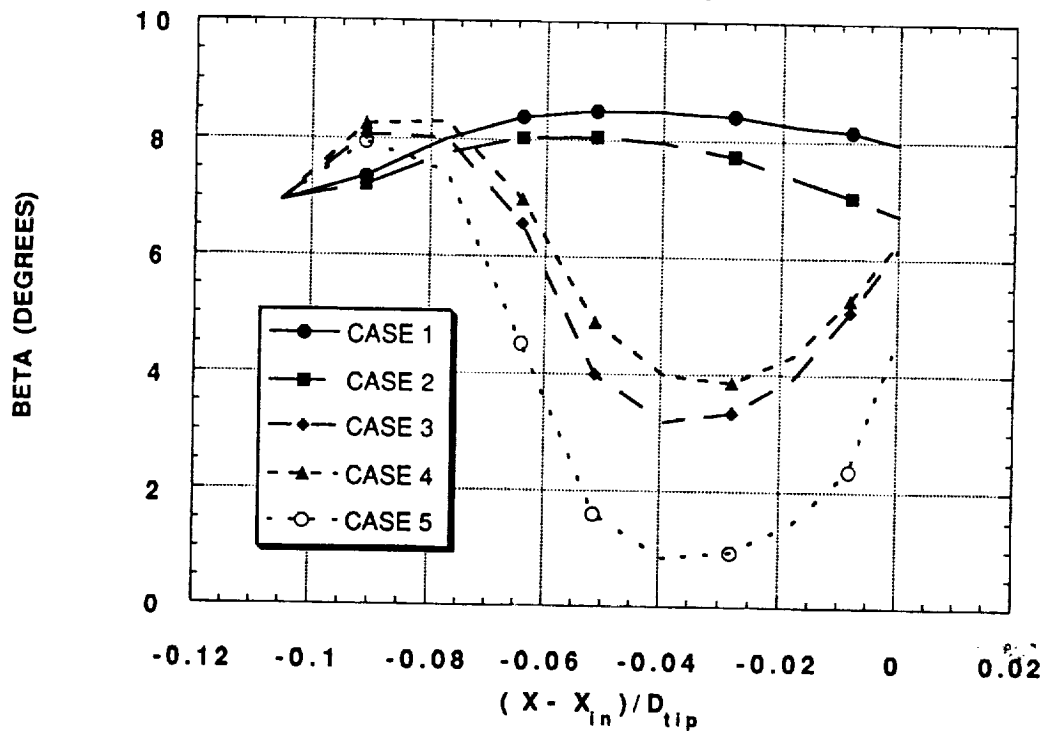


(b) Relative Flow Angle

Figure 7 The Meridional Velocity and Flow Angle Distributions Along the Hub Surface

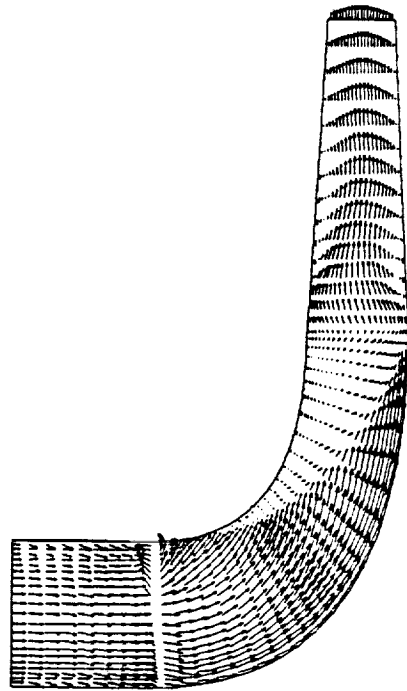


(a) Meridional Velocity

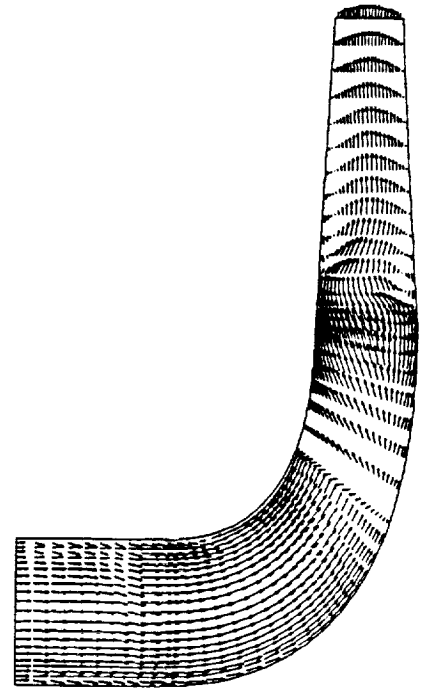


(b) Relative Flow Angle

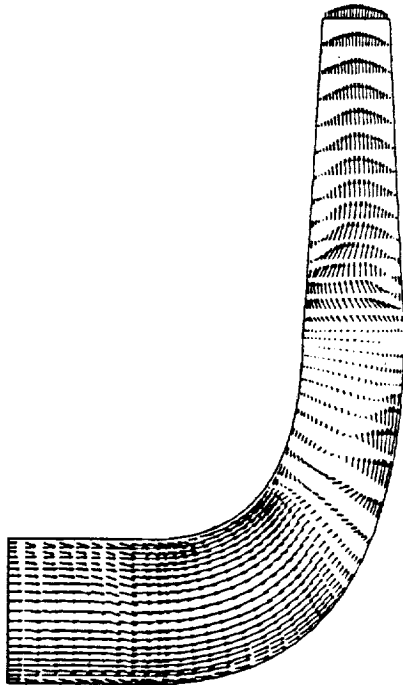
Figure 8 The Meridional Velocity and Flow Angle Distributions Along the Shroud Surface



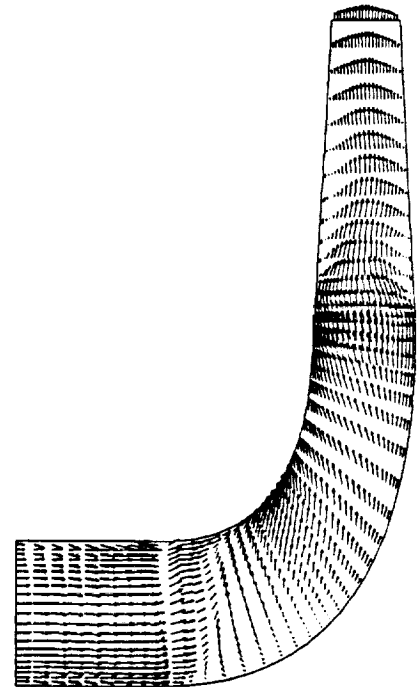
(a) Suction Side of Full Blade



(b) Pressure Side of Splitter

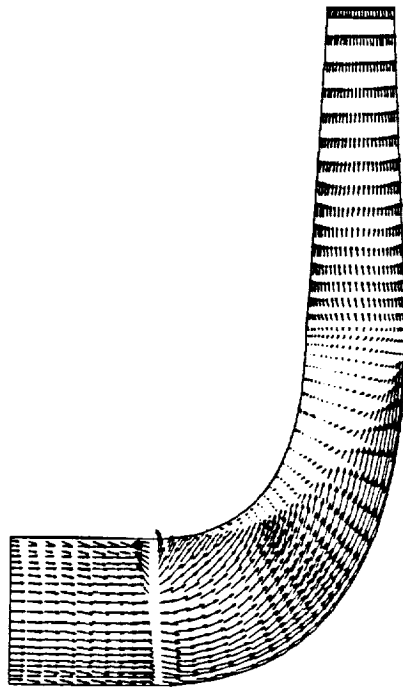


(c) Suction Side of Splitter

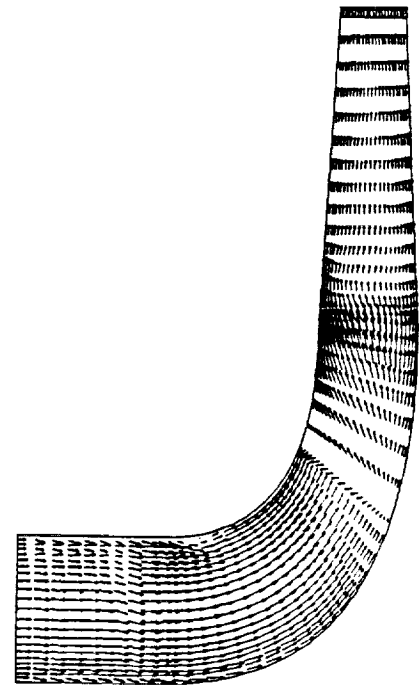


(d) Pressure Side of Full Blade

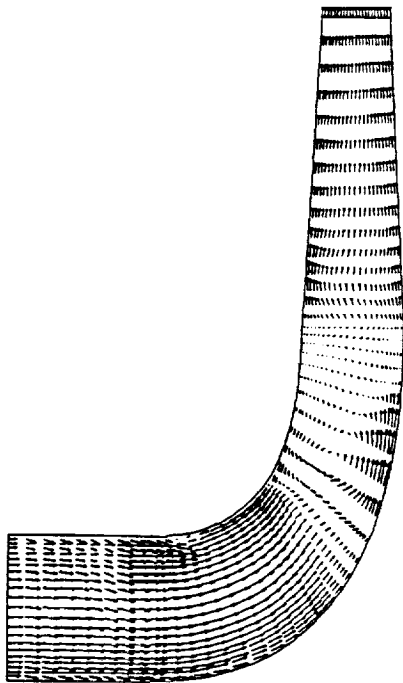
Figure 9 Velocity Vectors of the Consortium Baseline Impeller Flow, Case 1



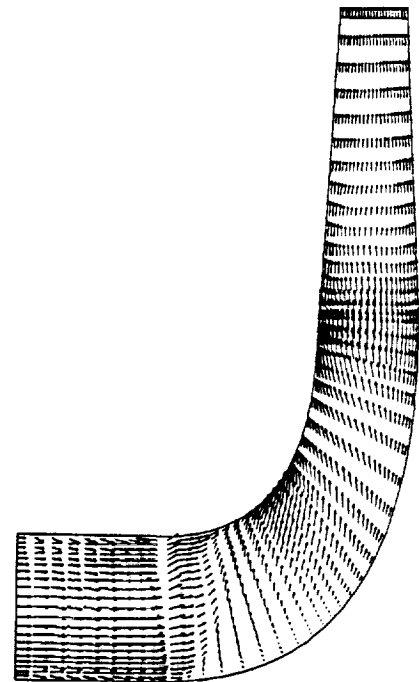
(a) Suction Side of Full Blade



(b) Pressure Side of Splitter

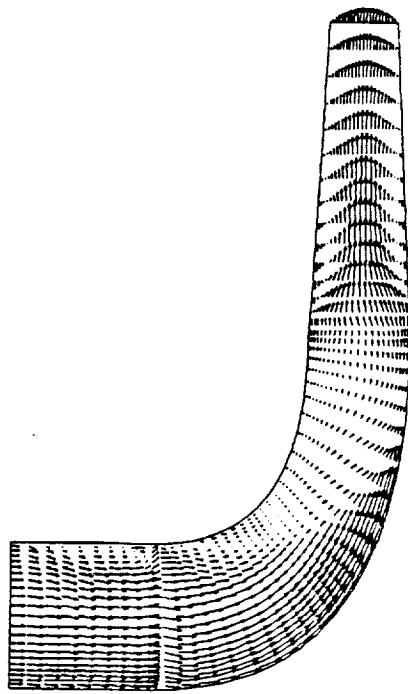


(c) Suction Side of Splitter

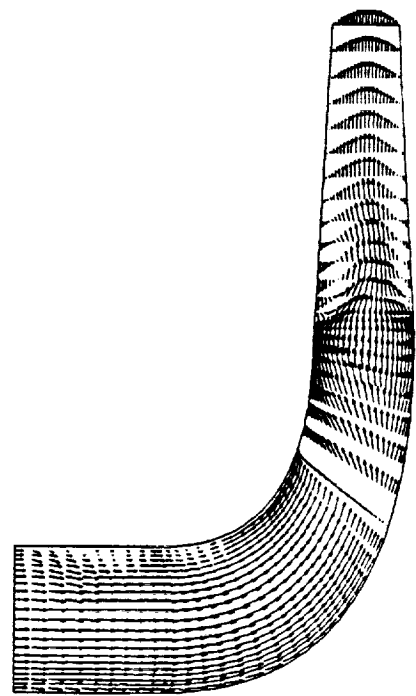


(d) Pressure Side of Full Blade

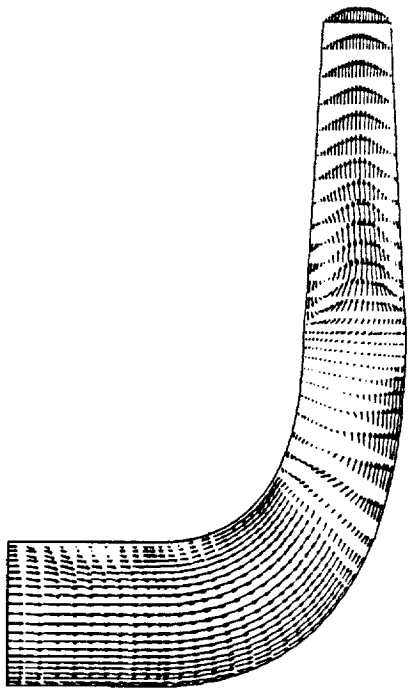
Figure 10 Velocity Vectors of the Consortium Baseline Impeller Flow, Case 2



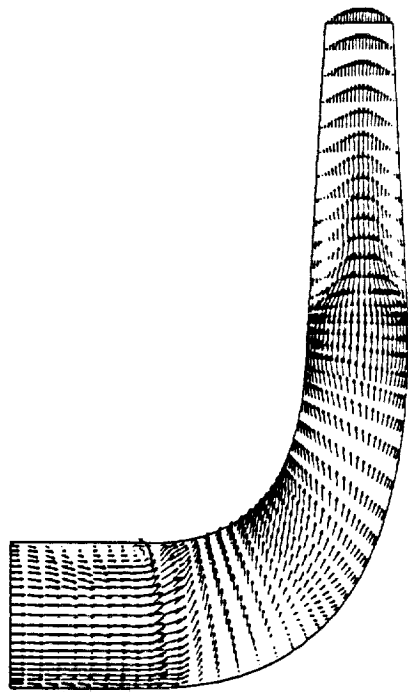
(a) Suction Side of Full Blade



(b) Pressure Side of Splitter

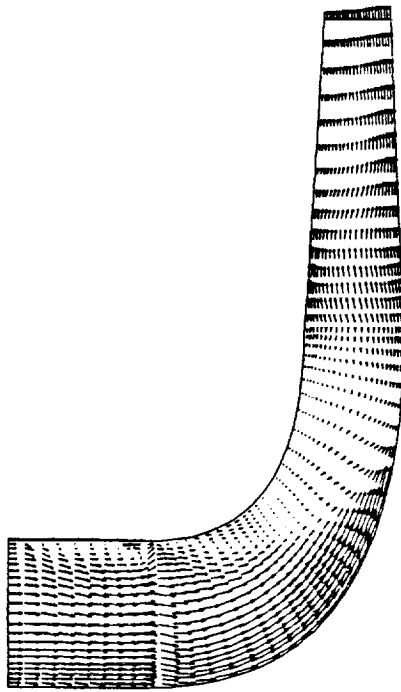


(c) Suction Side of Splitter

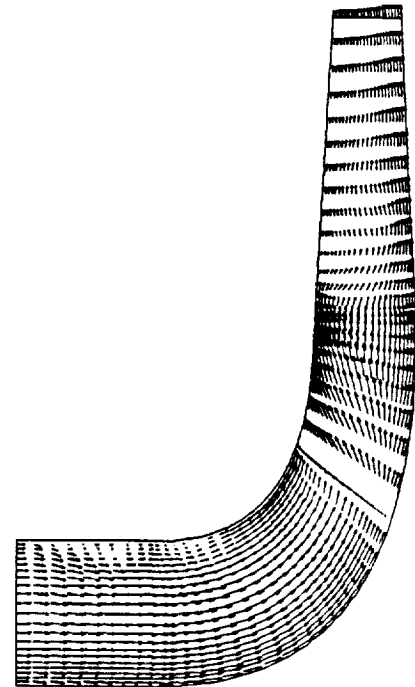


(d) Pressure Side of Full Blade

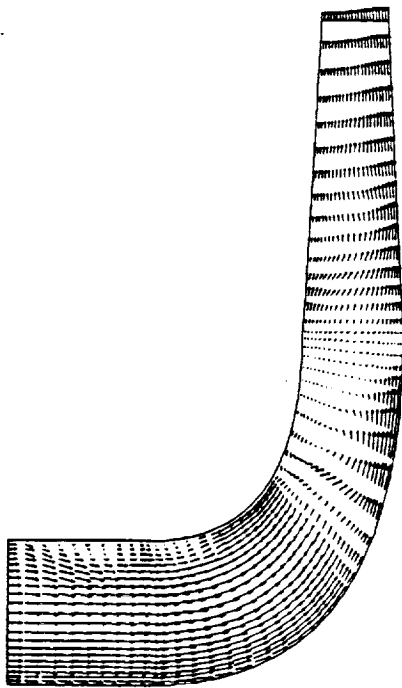
Figure 11 Velocity Vectors of the Consortium Baseline Impeller Flow, Case 3



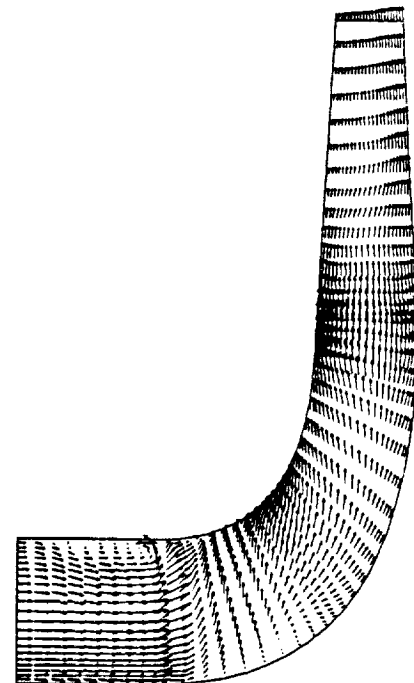
(a) Suction Side of Full Blade



(b) Pressure Side of Splitter



(c) Suction Side of Splitter



(d) Pressure Side of Full Blade

Figure 12 Velocity Vectors of the Consortium Baseline Impeller Flow, Case 5

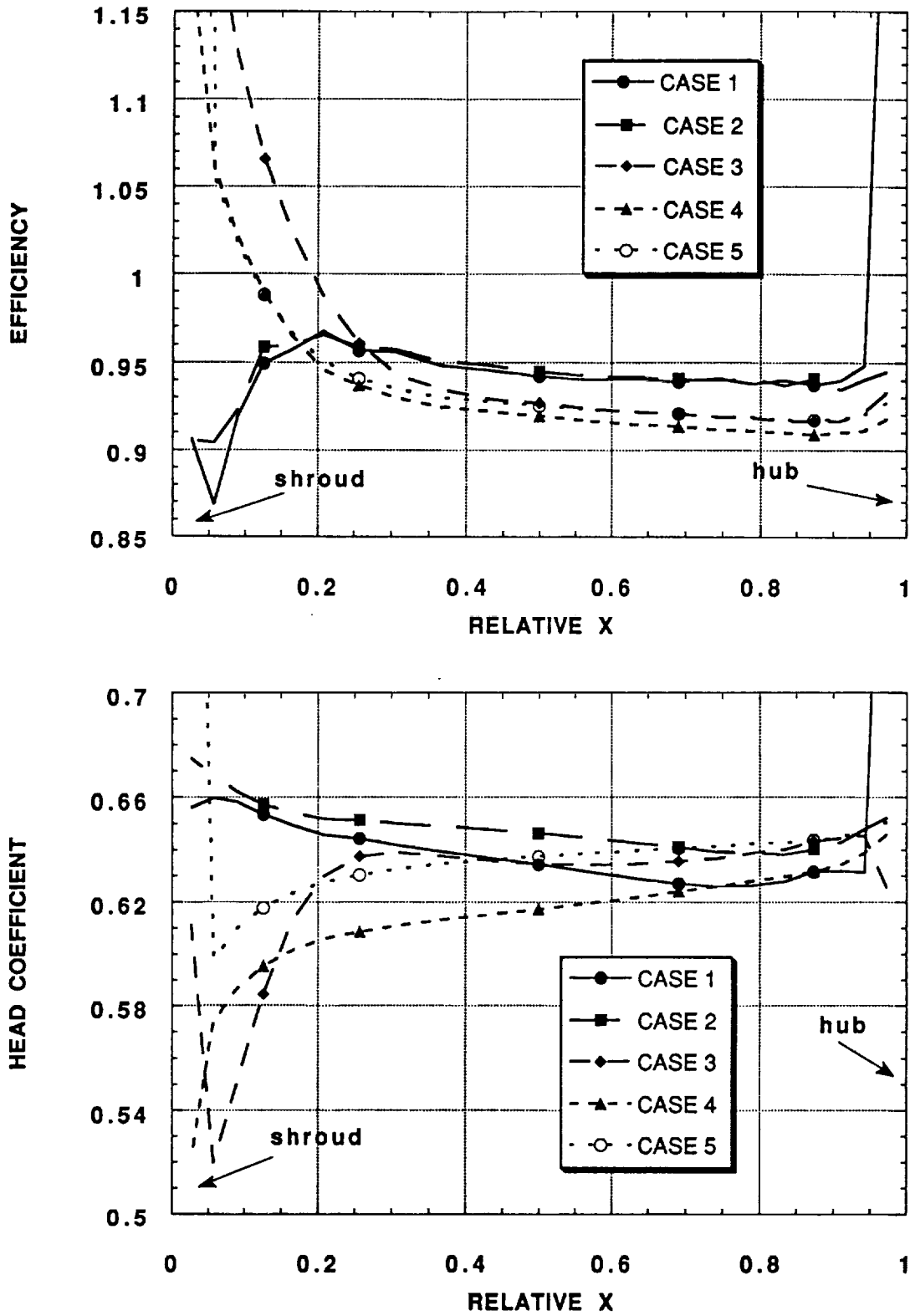
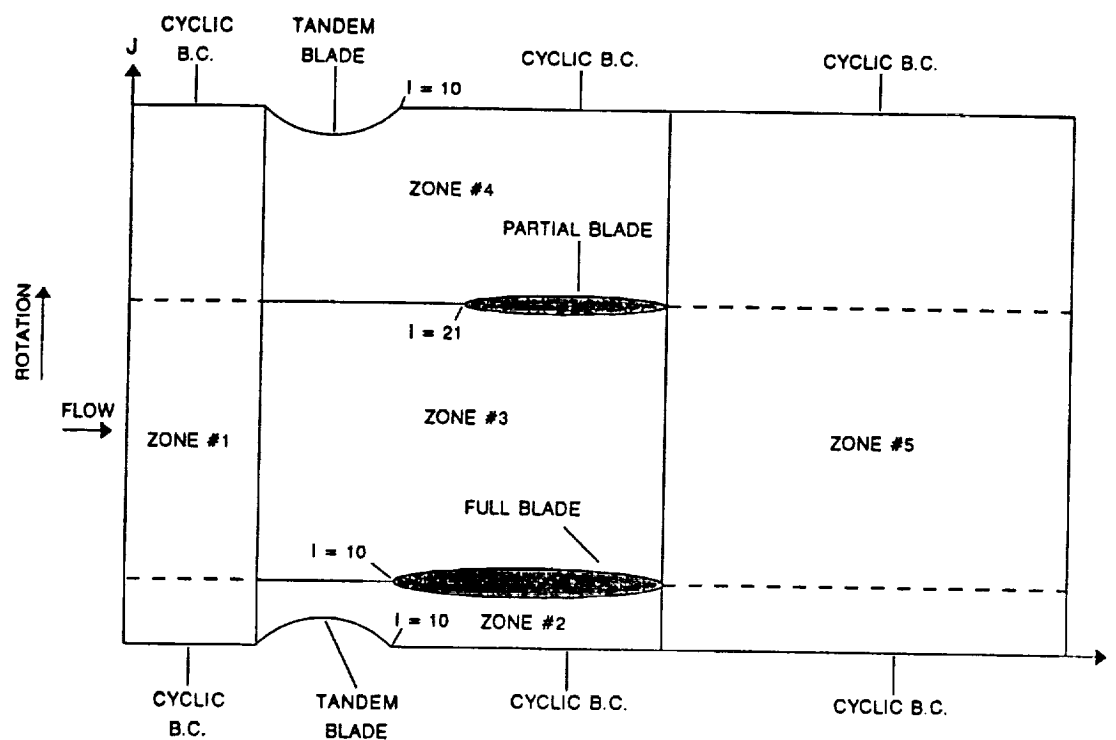


Figure 13 The Consortium Baseline Impeller Performance for Various Boundary Conditions

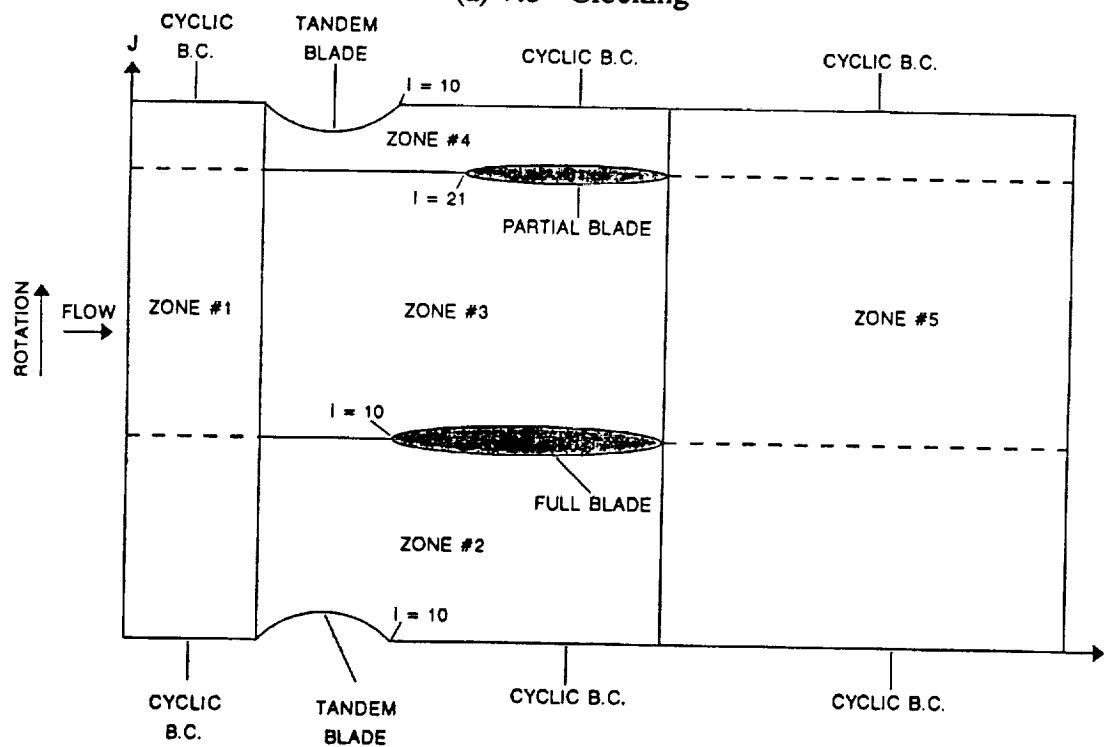
### Tandem Blade Effects

The numerical analyses of the consortium baseline impeller indicated that the flow separation near the shroud along the suction surface of the full blade caused the impeller exit flow to be highly non-uniform. There were several concepts proposed to modify the geometry and improve the impeller performance, such as TANDEM blade, increasing the length of partial blades, changing the leading edge angle of partial blades, offset of the partial blade location, changing the trailing edge blade lean angle, and etc. SECA was assigned to study the effect of TANDEM blade on impeller performance. The concept of TANDEM blade is to cut a portion of the full blade and clock it with a certain angle such that some flow can bleed through the gap and energize the area with high-loss flow. There were two TANDEM blade cases examined in this study, where the full blade was cut around 20% from the leading edge. The first case is a 7.5° clocking opposite to the rotation direction, while the second case is a 22.5° clocking opposite to the rotation direction which is the same as a 7.5° clocking in the rotation direction.

The numerical mesh systems for both TANDEM blade test cases were constructed to have five grid zones. Zone #1 represents the upstream section, and consists a 15 x 33 x 22 grid system for both cases. The downstream section is denoted as zone #5 and employs a 31 x 33 x 23 mesh system in both cases. Zones #2-#4 are designated for the blade passage. For the 7.5° clocking case, zones #2-#4 were discretized to have the 51 x 7 x 23, 51 x 17 x 23, and 51 x 11 x 23 grid points; whereas, a 51 x 13 x 23, a 51 x 17 x 23 and a 51 x 5 x 23 mesh system were used to describe zones #2-#4 in the 22.5° clocking case. The layout of mesh system and boundary conditions is demonstrated in Figure 14. The inlet flow conditions in the numerical calculations were based on the circumferentially averaged laser measurements. The numerical results of these two test cases indicated that the TANDEM blade concept did not improve the impeller performance<sup>11</sup>. As indicated in Figures 15-17, the 7.5° and 22.5° clockings of tandem blades not only distort the flow near leading edge, but also over-load the pressure side of impeller blades. The flow split at the exit of impeller blades was highly non-uniform, and thus the impeller efficiency was very low as shown in Figure 18. The numerical analysis of the 7.5° clocking case was shown to have a 56/44 percent flow split between suction and pressure sides



(a) 7.5° Clocking



(b) 22.5° Clocking

Figure 14 Mesh System and Boundary Condition Layout for TANDEM Blade Impeller Study

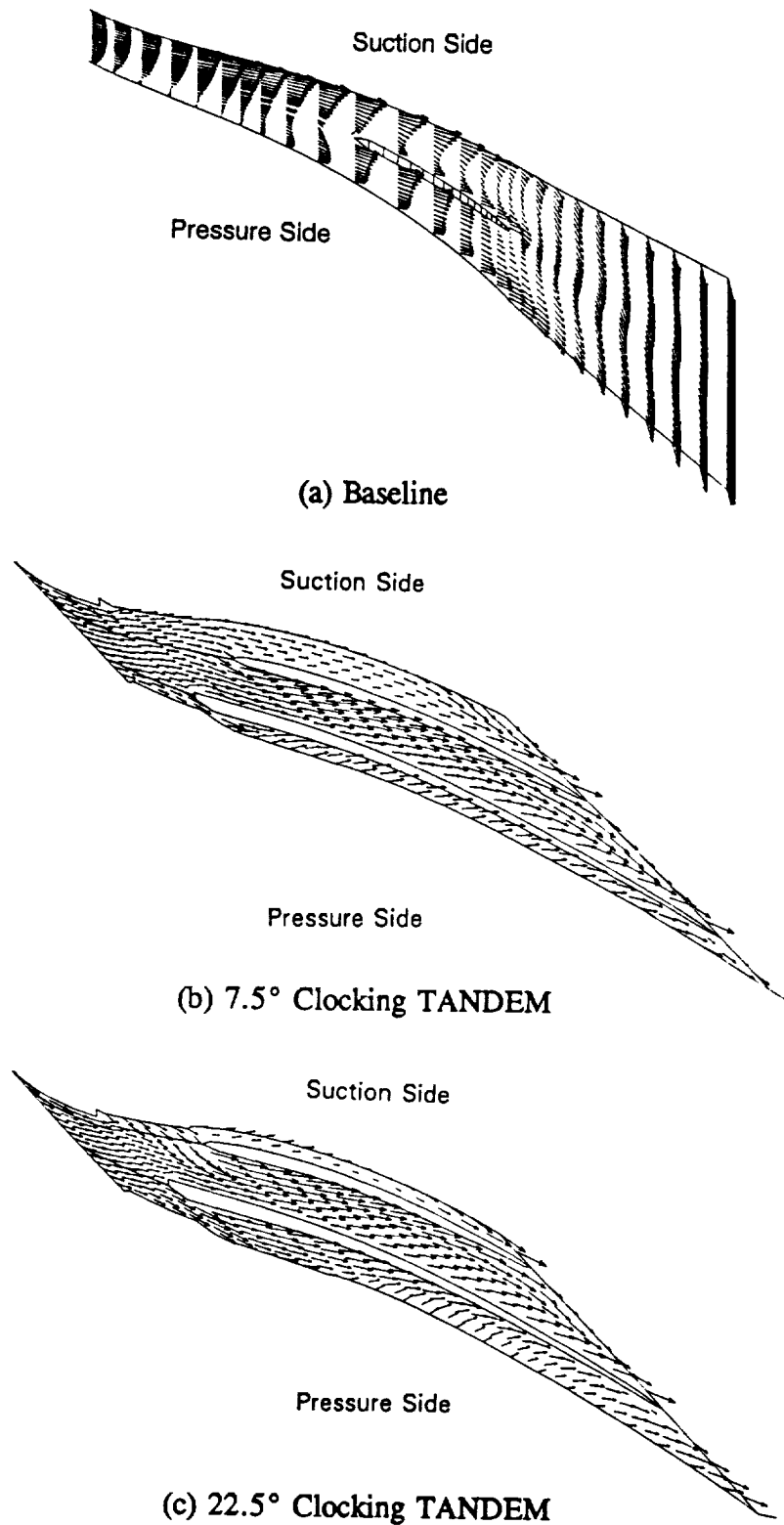


Figure 15 Velocity Vectors Near the Hub Surface of the Impeller (Blade-to-Blade)

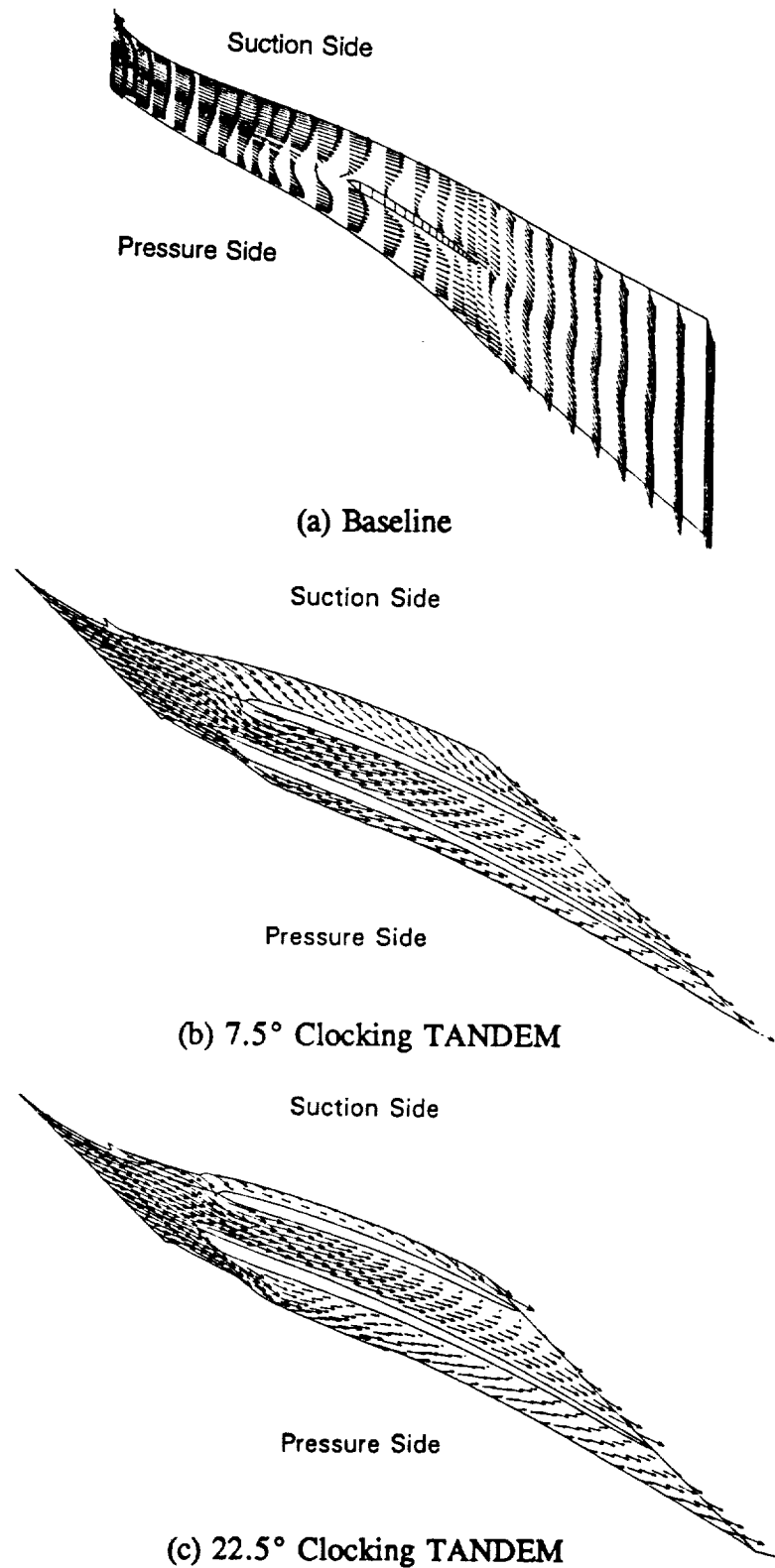


Figure 16 Velocity Vectors at the Mid Plane of the Impeller (Blade-to-Blade)

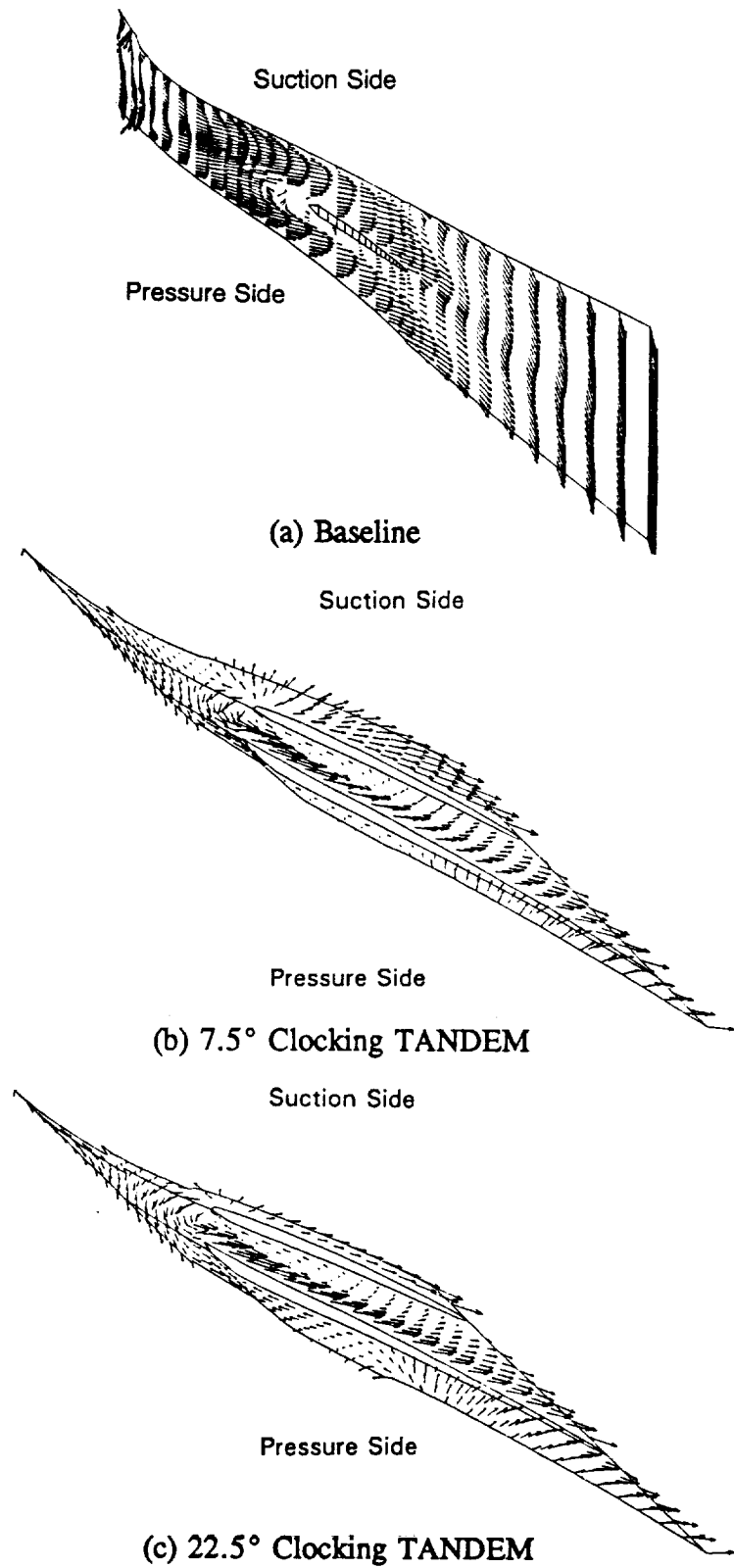


Figure 17 Velocity Vectors Near the Shroud Surface of the Impeller (Blade-to-Blade)

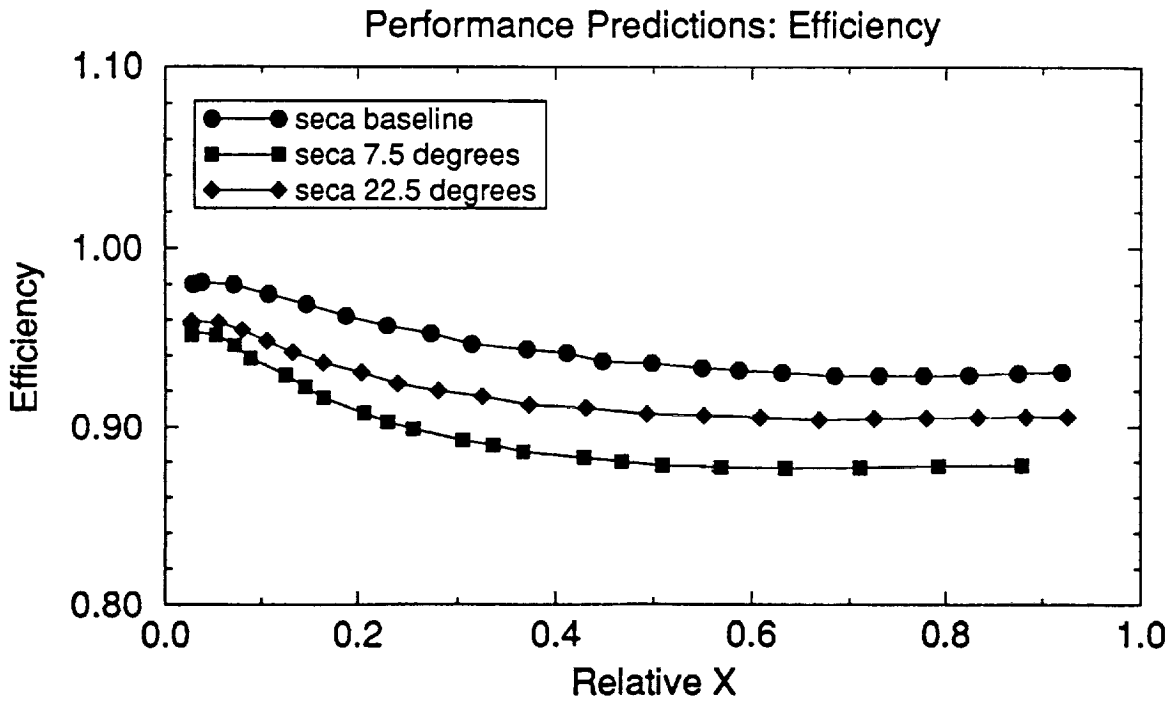
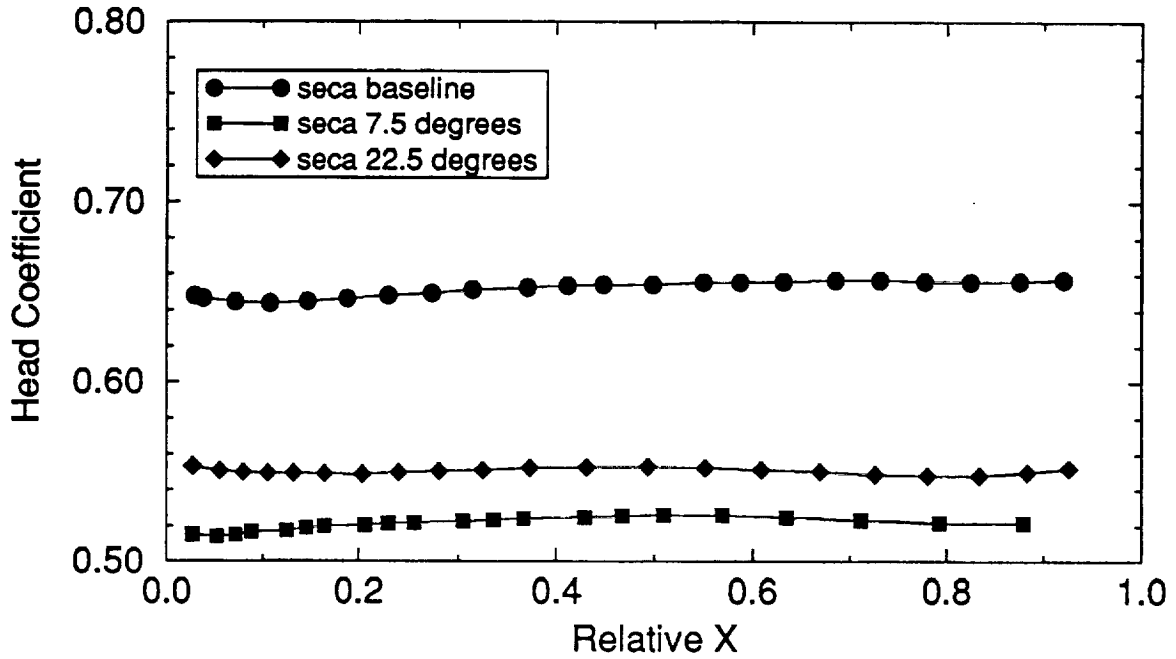


Figure 18 Comparisons of the Impeller Performance for Various Geometry Modification

of full blades, while it had a 60/40 percent flow split for the 22.5° clocking case comparing to a 48/52 percent flow split for the baseline case. However, due to the grid skewness and coarseness, the result can only provide the qualitative trend, not a quantitative assessment. Meanwhile, 7.5° clocking of the TANDEM blade in both directions is probably too large such that the flow is perturbed too far away from the design condition.

Although the TANDEM blade concept did not show the improvement to the baseline impeller, some modification concepts were shown to improve the impeller flow split and performance. The key observations from the parametric studies which could implement the consortium baseline impeller were: 1) the change of lean angle at the blade trailing edge can reduce the blade-to-blade distortion, 2) the variation of discharge blade angle can improve impeller performance, 3) the offset of partial blade location can help the uniformity of exit flow splits, and 4) the increase of impeller axial length and the reduction of impeller exit cavity width can improve the overall efficiency. An advanced concept impeller was then designed based on the conclusion of consortium baseline impeller studies.

#### 4.2 ADVANCED CONCEPT IMPELLER

The major changes from the baseline impeller to the advanced concept impeller were detailed in Ref. 12, and can be briefly identified as: 1) impeller axial length is increased from 1.8' to 2.32', 2) exit cavity width is reduced from 0.716' to 0.575', 3) impeller discharge angle is increased from 38° and 38° (for tip and hub), to 60° and 74°, 4) total wrap angle is reduced from 83° and 105° (for tip and hub) to 62° and 58°, 5) discharge blade lean angle is changed from 16° to -29°, and 6) partial blade leading edge offset 5° towards full blade pressure side. The numerical results show that both the head coefficient and the efficiency of the impeller are improved by the new design, which is consistent with the conclusion from previous parametric studies. However, the calculated flow split of the present impeller was quite non-uniform; 59% of the mass flow rate passes through the suction side of the full blade and 41% through the suction side. The numerical analysis of the baseline impeller revealed a 48/52 percent split between the pressure and the suction sides. It was suspected that 5° offset of the partial blade

could be too much and reversed the trend of the flow split. This case was then denoted as Acd. #1 impeller. Meanwhile, the backflow near the impeller leading edge occurred in baseline impeller was not eliminated by the advanced design.

A second advanced concept impeller (Acd. #2) was designed by removing the  $5^\circ$  offset of the partial blade from the Acd. #1 impeller. The numerical result indicated that both the head coefficient and the efficiency of the second impeller were very close to those of the Acd. #1 impeller, while the flow split of the Acd. #2 impeller was more uniform (55/45 for suction/pressure side). Meanwhile, the unacceptable backflow near impeller leading edge was still present in the Acd. #2 impeller. Hence, the pump consortium furnished the third (Acd. #3) and fourth (Acd. #4) designs of the advanced concept impeller. The configuration of Acd. #3 impeller is identical to that of Acd. #2, except the total wrap angle was increased and the leading edge lean was added; while the Acd. #4 impeller is similar to the Acd. #3 impeller with a slightly higher hub-to-shroud angle variation at the trailing edge. The performance of both the Acd. #3 and Acd. #4 impellers were computed to be very good and almost identical, and were close to the Acd. #2 impeller; however, the flow separation near the leading edge of impeller of the third and fourth designs is much smaller than that of the Acd. #2 impeller.

The fifth advanced concept impeller configuration (Acd. #5) was also issued by the pump consortium. The Acd. #5 impeller is the same as the Acd. #4 impeller with the exception of a  $2.5^\circ$  offset of the partial blade towards the pressure side of full blades. The Acd. #5 impeller was analyzed with two mesh systems, one is constructed by Rocketdyne (Acd. #5-1), and the other is a modification of the first one by stretching the grid towards the wall (Acd. Final). The stretched grid system provides better convergence rate and more uniform flow field than the uniform one. This is consistent with a great variety of numerical studies of turbulent flows, and is because the  $k-\epsilon$  turbulence model is sensitive to the near-wall grid spacing. The numerical results of both cases demonstrated that the Acd. #5 impeller has better performance with respect to more uniform flow split, lower flow distortion, and higher head coefficient than the previous four impeller designs. The numerical analyses of all pump consortium impellers are summarized

as shown in Table 6. The comparison of efficiency and head coefficient for all numerical analyses of consortium impellers are demonstrated in Figure 19.

Table 6 Performance Summary of the Pump Consortium Impeller Study

	Flow Split (Suction/Pressure)	Blade-to-Blade Distortion	Hub-to-Shroud Distortion	Efficiency (%)
Baseline	48/52	0.095	2.387	96.4
Acid. #1	58.6/41.4	0.1024	3.497	96.5
Acid. #2	54.1/45.9	0.0819	4.799	97.3
Acid. #3	57.4/42.6	0.0627	7.632	97.5
Acid. #4	56.1/43.9	0.0592	6.08	97.8
Acid. #5-1	48.5/51.5	0.0571	6.18	98.7
Acid. Final	51/49	0.0579	7.1	98

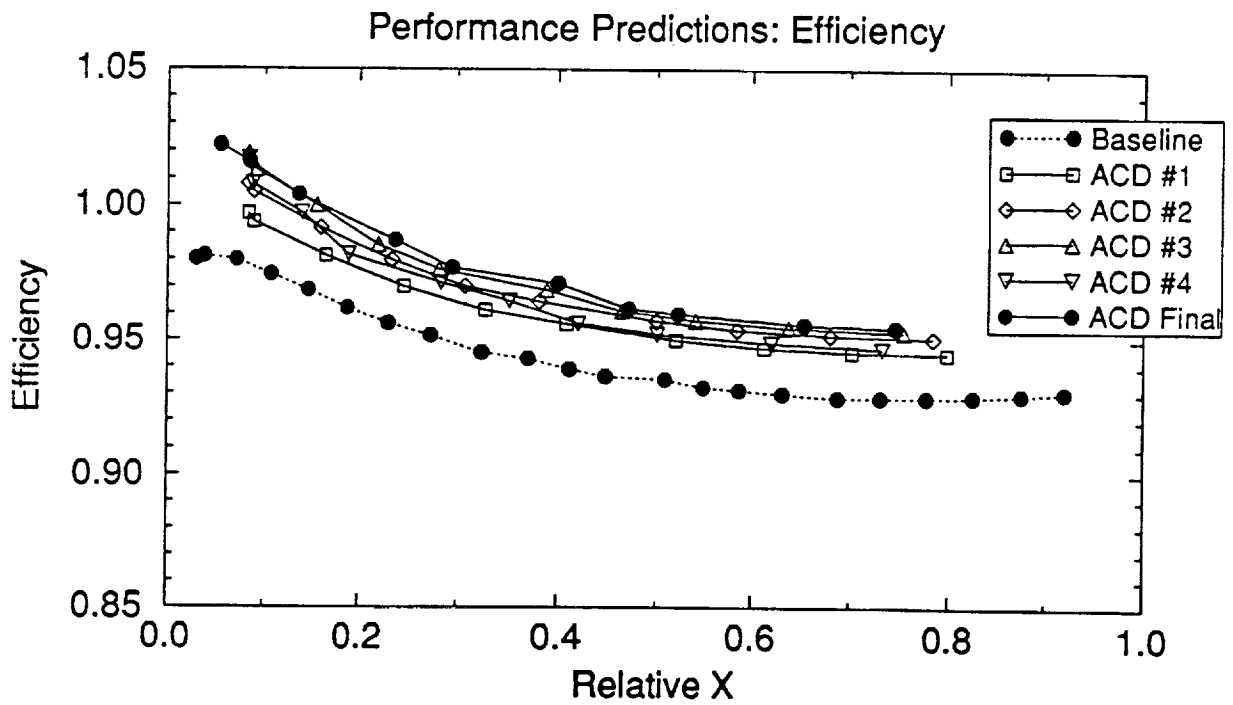
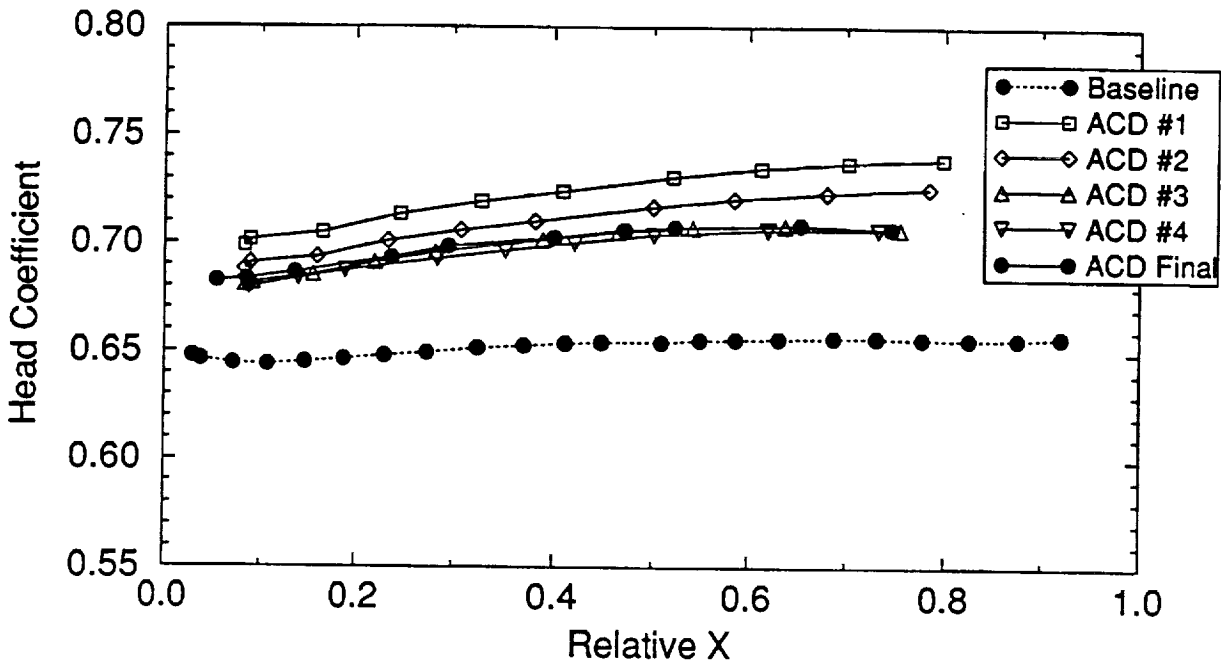


Figure 19 The Performance Comparison of All Consortium Impellers

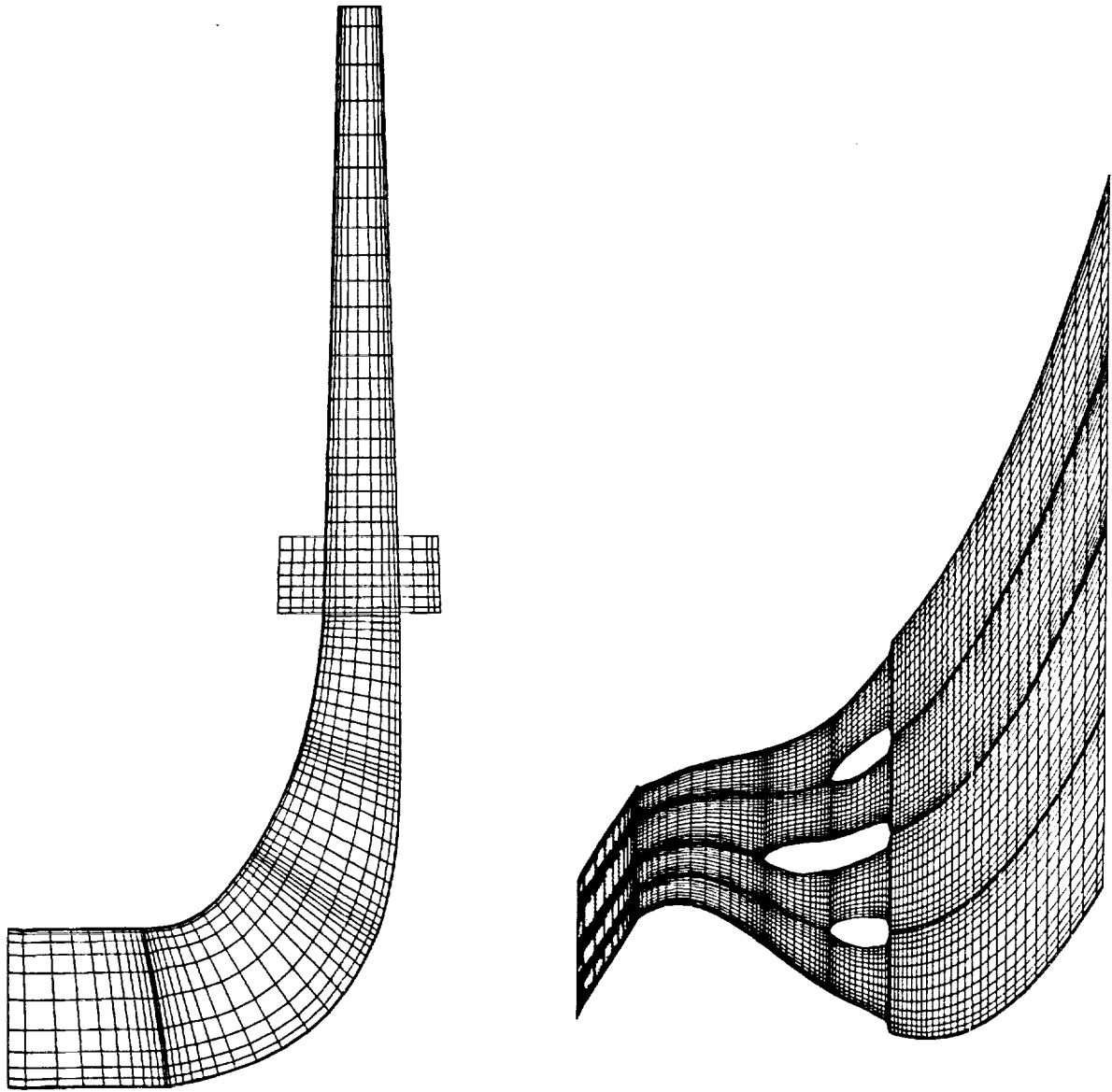
## 5.0 SSME-HPFTP IMPELLER FLOW STUDY

Another test case to benchmark the proposed CFD pump model is the SSME HPFTP impeller<sup>13</sup>. The geometry of this impeller is very complicated because there are six full blades along with six long partial blades and twelve short partial blades. The SSME impeller is a shrouded impeller, and its test conditions are listed in Table 7. A periodic boundary condition in the circumferential direction was used such that the computational domain consisted of only one full blade, one long splitter blade and two short splitter blades (i.e. within 60° angle in the cross section). A downstream cavity region at the exit of the impeller blades was modeled in the present investigation to include the effect of the vaneless space downstream of the impeller. In the present study, the original grid mesh was generated by Rocketdyne, and then a modification was made to include the downstream cavity geometry and to cut down the grid size in the hub-to-shroud direction.

Table 7 Configuration and Test Conditions of the SSME HPFTP Impeller

Full Blades/Long Splitters/Short Splitters	6/6/12
Working Medium	Water (70 °F)
Shaft Speed (rpm)	6322
Exit Tip Diameter	11 inches
Inlet Hub Diameter	3.95 inches
Inlet Tip Diameter	6.349 inches
Reference Velocity	303.4 ft/sec
Reference Reynolds Number	$2.263 \times 10^7$
Diffuser/Impeller Diameter Ratio	1.136

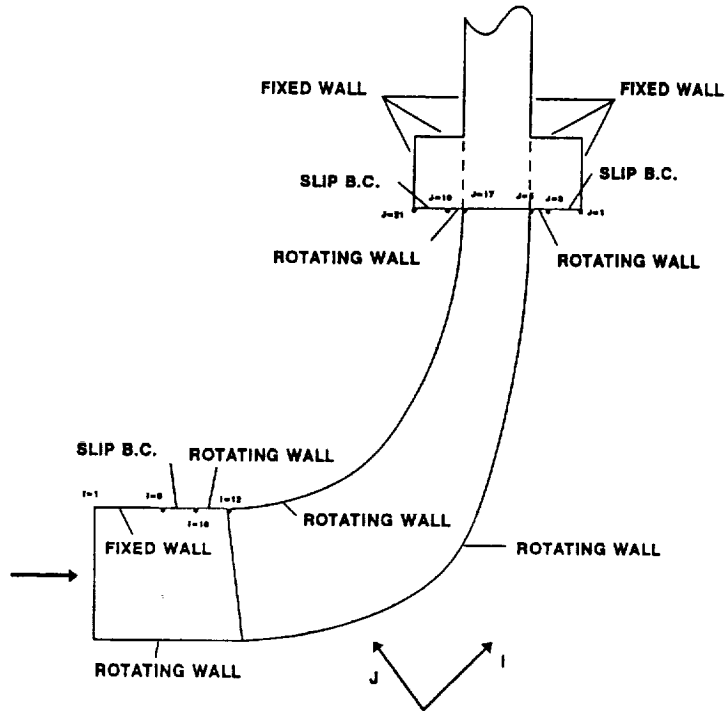
The final mesh system used in this study consisted seven zones; Zone #1: 12 x 13 x 67 for the upstream region from the impeller blades, Zone #2: 48 x 13 x 16 for the flow passage between the suction surface of the full blade and the pressure surface of the short splitter, Zone #3: 48 x 13 x 16 for the flow passage between the suction surface of the short splitter and the pressure surface of the long splitter, Zone #4: 48 x 13 x 22 for the flow domain between the suction surface of the long splitter and the pressure surface of the short splitter, Zone #5: 48 x 13 x 16 for the flow domain between the suction surface of the short splitter and the pressure surface of the full blade, Zone #6: 8 x 21 x 67 for the downstream cavity region at the exit of impeller blades, and Zone #7: 23 x 13 x 67 for the downstream extension region. The mesh system in this study is considered to be very coarse due to the presence of many blade surfaces and an exit cavity. The layout of the grid system and the boundary conditions are shown in Figures 20-21. The computed flow field near the hub, the mid-plane, and the shroud surfaces are plotted in the unwrapped view and is shown in Figure 22. Also, in Figure 23, the flow field near various blade surfaces are plotted. The relative velocity vectors at the exit of impeller blades, as indicated in Figure 24, reveals that more flow tends to exit from the passage near the pressure side of the full blade than that near the suction side of the full blade. The present pump model predicts the flow splits as 31% for the passages of full blade pressure side to short splitter suction side, 26% for that of short splitter pressure side to long splitter suction side, 24% for that of long splitter pressure side to short splitter suction side, and 19% for that of short splitter pressure side to full blade suction, respectively. As shown in Figure 23, a flow separation occurs near the shroud of the full blade suction side, which blocks the flow from passing through the suction side. This is very common in turbopump impeller design, where the full blade is highly loaded, and thus the flow tends to separate on the suction surface. In the advanced impeller design, there are several methodologies to improve such deficiencies, such as using tandem blades, incorporating blade lean, changing partial blade locations, varying the chordwise blade angle distribution to control the high loading location on the full blade, etc. However, the test data show slightly more uniform flow splits at the exit of impeller blades but the trend is as predicted by the numerical analysis. The discrepancy between the numerical prediction and the measurement of flow splits could be caused by the grid coarseness around the leading edge of blades. The actual testing blade has a blunt leading edge, but the numerical mesh



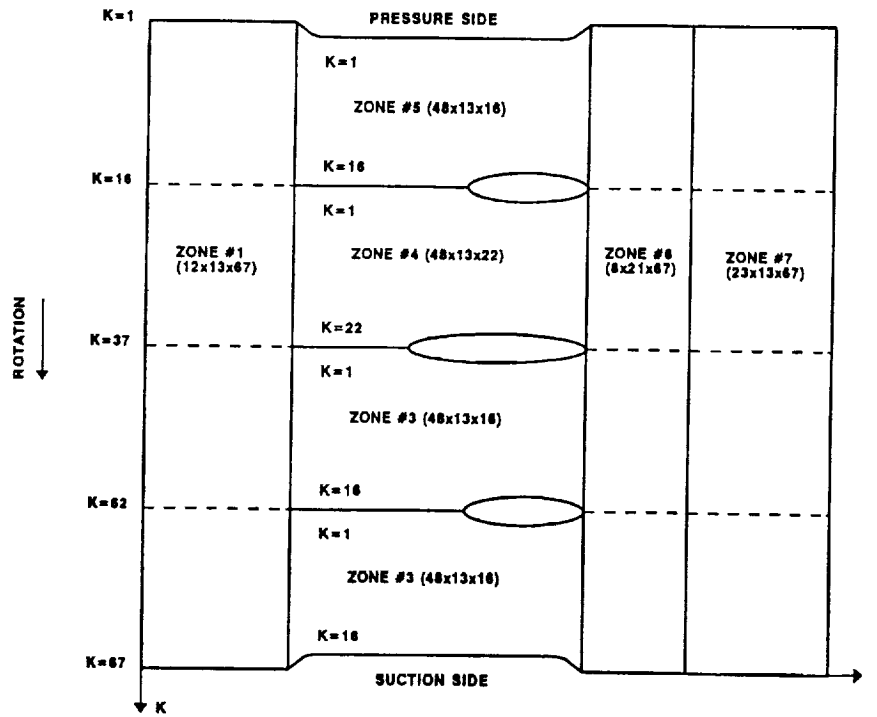
(a) Hub-to-Shroud

Blade-to-Blade

Figure 20 The Mesh System for the SSME HPFTP Impeller Flow Study

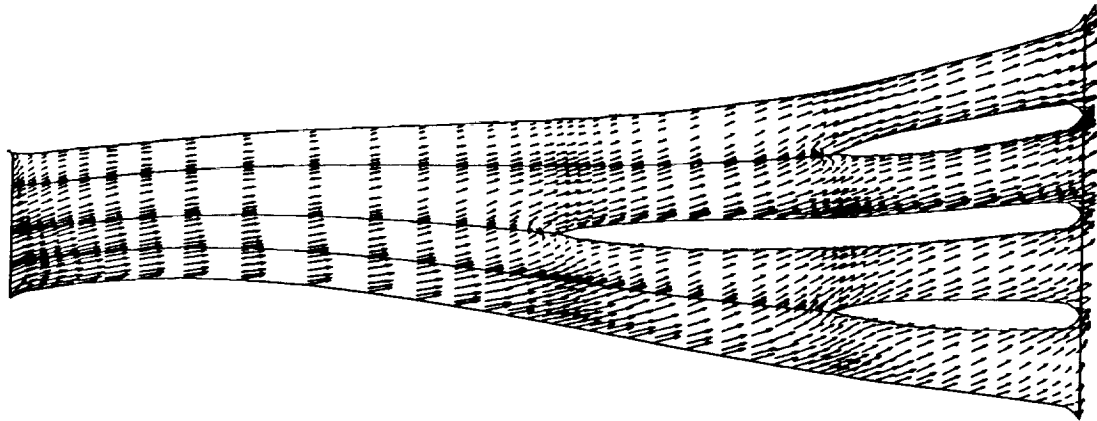


(a) Hub-to-Shroud

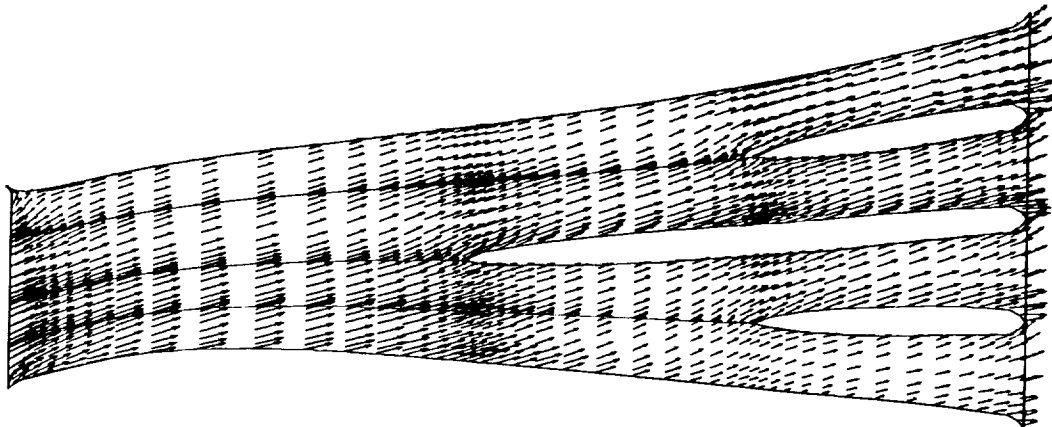


(b) Blade-to-Blade

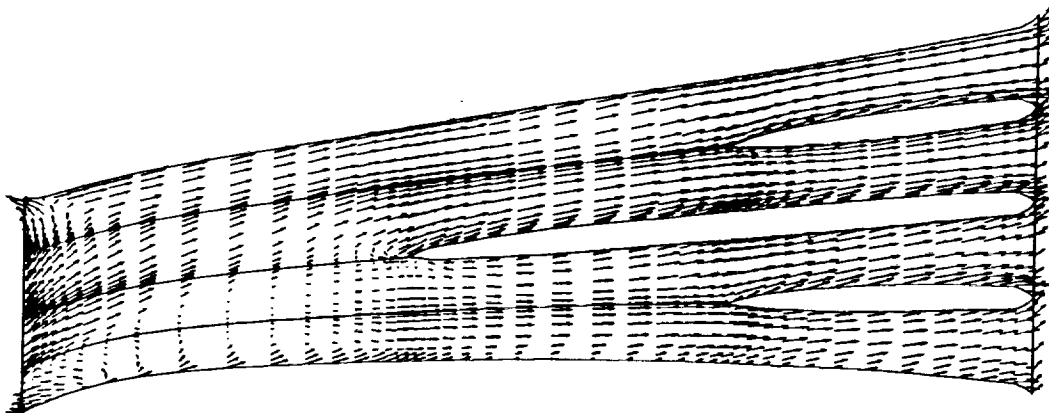
Figure 21 The Boundary Condition Layout for the SSME HPFTP Impeller Flow Study



(a) Near the Hub

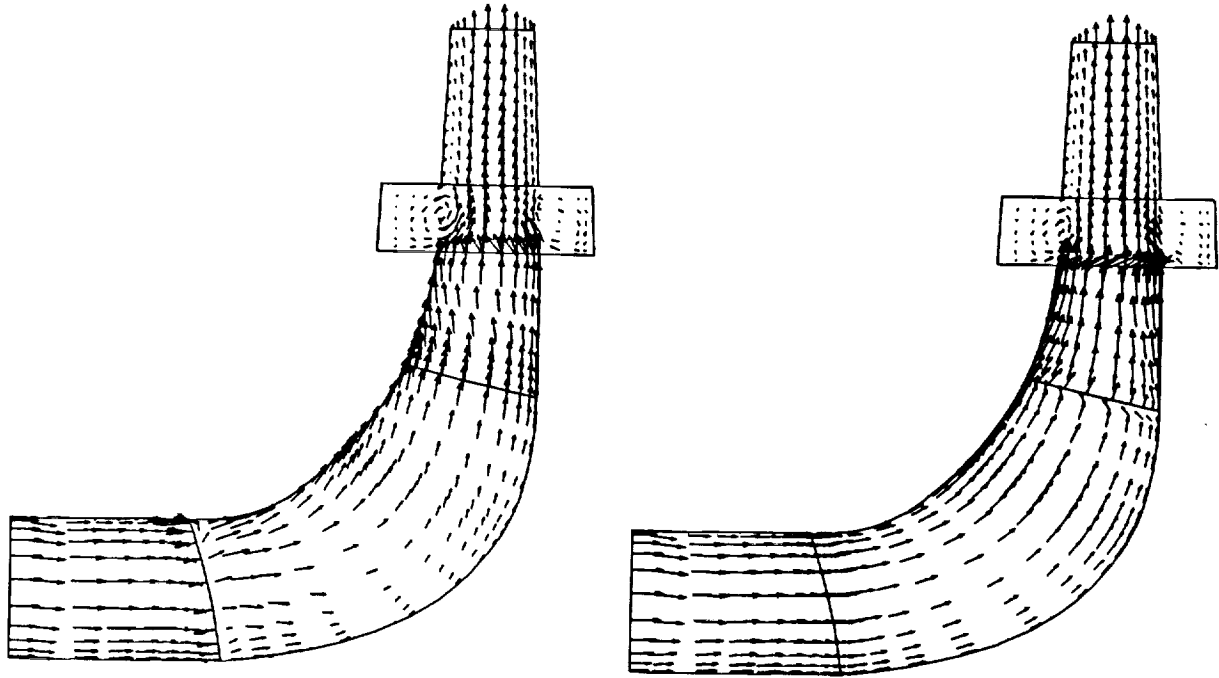


(b) at the Mid Plane

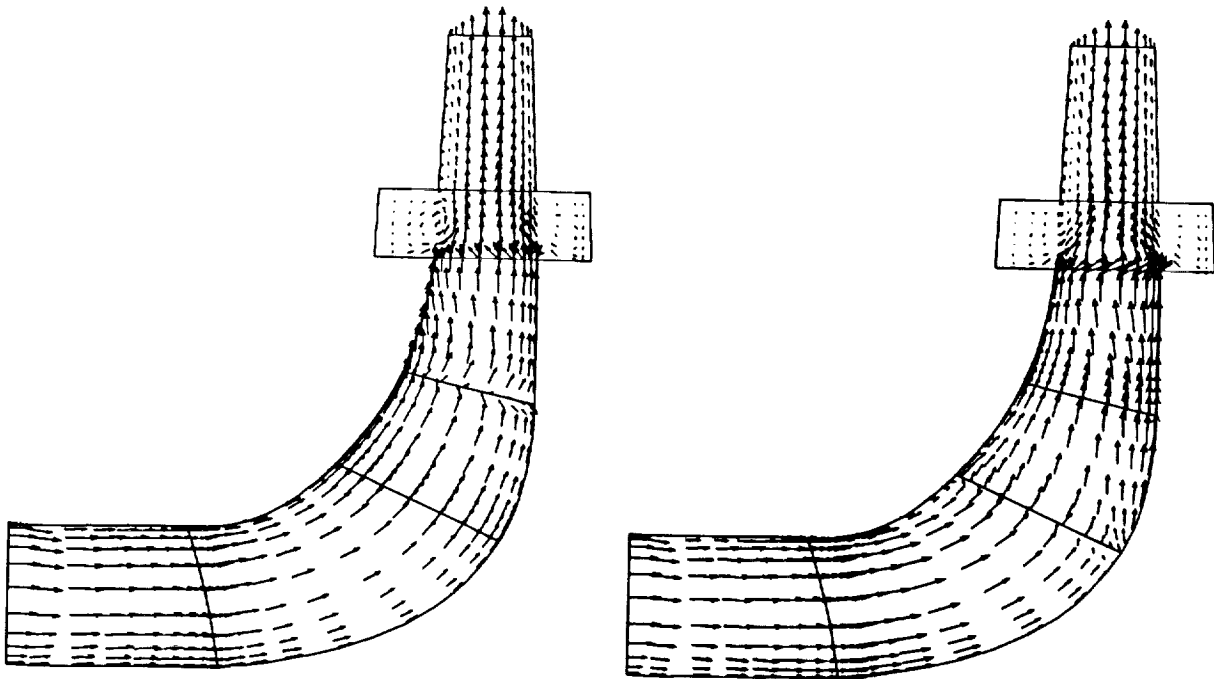


(c) Near the Shroud

Figure 22 Velocity Vectors at Various Blade-to-Blade Surfaces of the SSME HPFTP Impeller

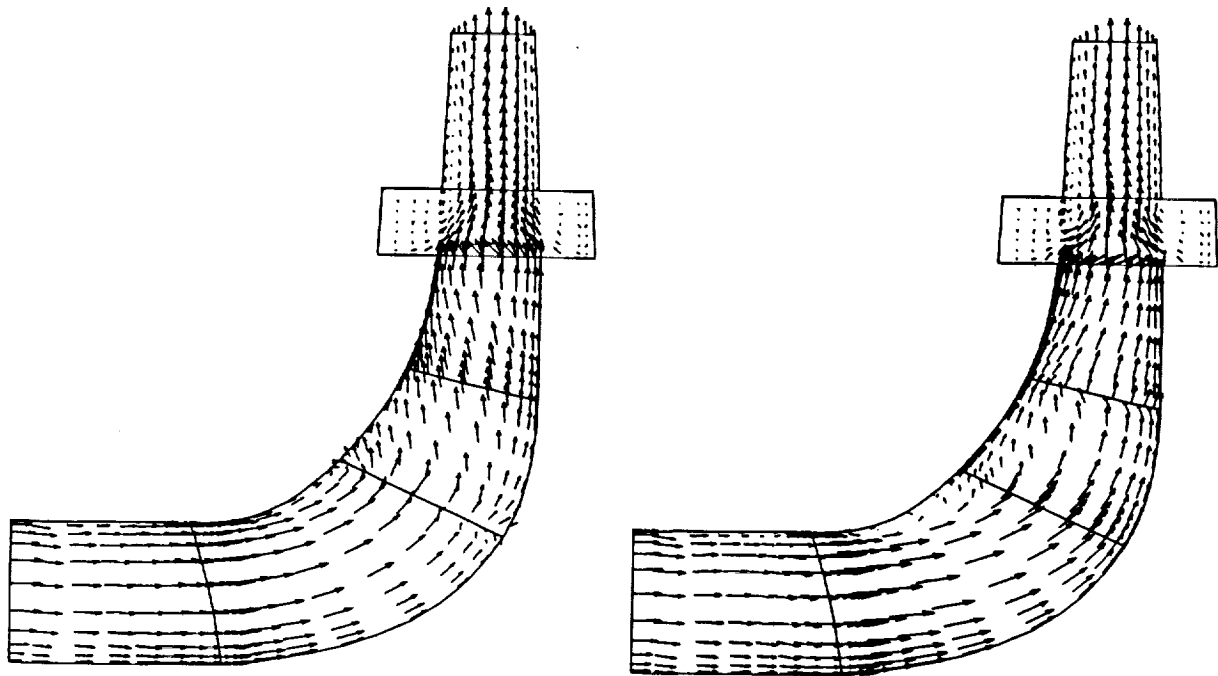


Full Blade Pressure Side ← to → Short Splitter Suction Side

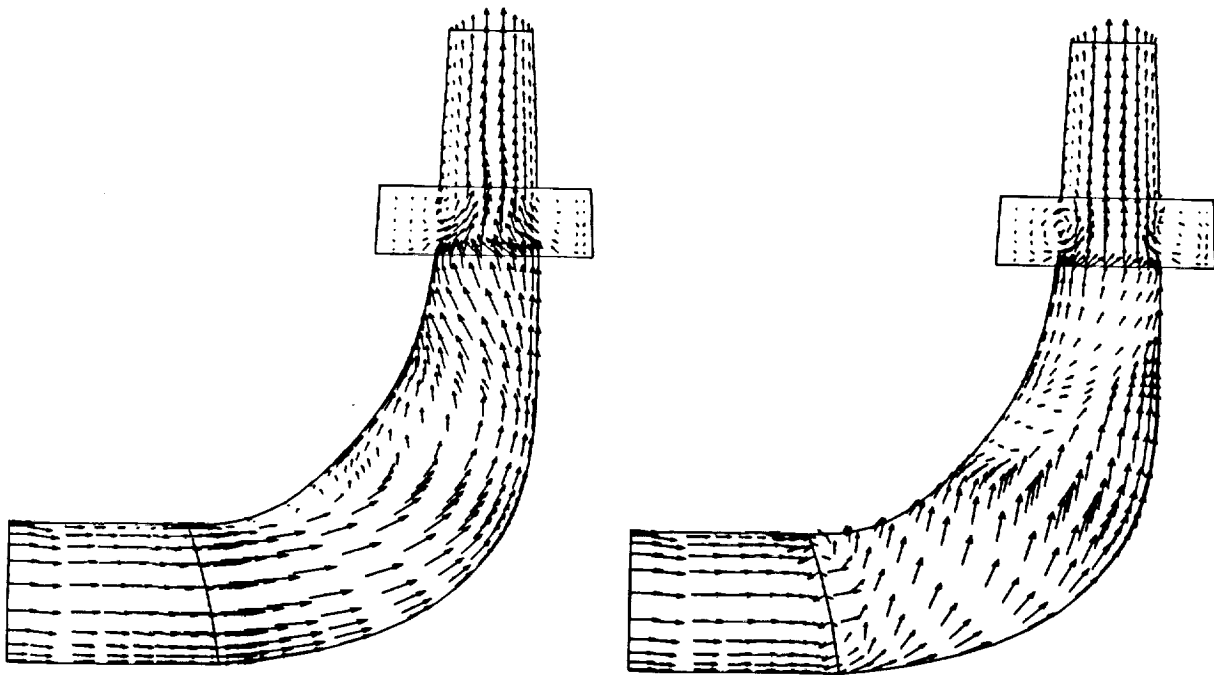


Short Splitter Pressure Side ←to→ Long Splitter Suction Side

Figure 23 Velocity Vectors at Various Hub-to-Shroud Surfaces of the SSME HPFTP Impeller



Long Splitter Pressure Side ←to→ Short Splitter Suction Side



Short Splitter Pressure Side ←to→ Full Blade Suction Side

Figure 23 Continued

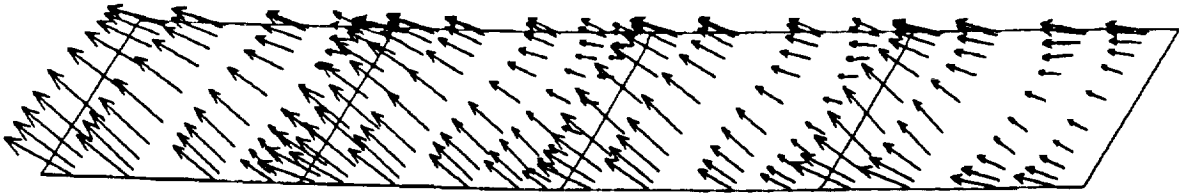


Figure 24 Velocity Vectors at the Exit of SSME HPFTP Impeller

system, generated by Rocketdyne, described the nose region as a knife edge. The wedge-like leading edge actually forces the flow to turn harder at the nose region, and causes a larger flow separation, hence a larger blocking effect near the suction surface.

In the experimental test conducted by Rocketdyne<sup>14</sup>, LDV measurements were taken at three radial planes in the impeller discharge cavity. The location of data points at a given circumferential section is illustrated as shown in Figure 25, in which B2 represents the width between shroud and hub at the impeller blade exit. In this report, the data comparison is made only within the B2 width, because flows were allowed to bleed to the impeller inlet in the actual hardware, as shown in Figure 25. However, in the numerical analysis, a no slip boundary condition for the cavity surface at the impeller discharge was imposed, as indicated in Figure 21. A better treatment of boundary conditions in the discharge cavity region can improve the prediction of the strength of the downstream recirculating flows, and thus will lead to better data comparison. The comparisons between numerical calculations and experimental measurements are performed for both absolute radial ( $C_m$ ) and absolute tangential ( $C_w$ ) velocities at plane #1 ( $r/D_{ip} = 0.5064$ ), plane #2 ( $r/D_{ip} = 0.5183$ ), and plane #3 ( $r/D_{ip} = 0.5303$ ), and are shown in Figures 26-28, respectively. Both radial and tangential velocities are non-dimensionalized by the impeller tip velocity ( $U_{ip}$ ). In Figures 26-28, at each %B2 planes the angular location varies from  $-70^\circ$  to  $-10^\circ$ , which corresponds to the range from the suction side of full blade to the pressure side of full blade, respectively. In Figure 26, the impeller discharge wakes can be clearly observed from the experimental data; however, the numerical analysis predicts less distinct wake profiles, where the trough in radial velocities is due to the blade trailing edge. The

disagreement could be attributed to the sharp trailing edge configuration described by numerical meshes, where in the actual hardware impeller blades have some thickness. The difference of trailing edge geometries provides a faster flow mixing in the numerical calculation than that in the experimental test. Since plane #1 is very close to the impeller discharge, the effect of trailing edge is severe, and thus the discrepancy between numerical calculations and measured data is relatively large. Nevertheless, in the plane #1 the general flow features, such as vortices in the cavity and larger radial velocities near pressure surfaces, are predicted by the numerical simulation. As flows go further downstream, e.g. plane #3, the agreement between numerical predictions and test data is greatly improved due to the decay of wake effect, which can be seen in Figure 28. Although the present model slightly underestimates the wake defect, the magnitudes of both absolute radial and tangential velocities are well predicted. Also note that the discrepancy between numerical and experimental results is getting larger towards the hub and shroud walls, which is due to the inaccuracy in computing the vortices in the cavity region.

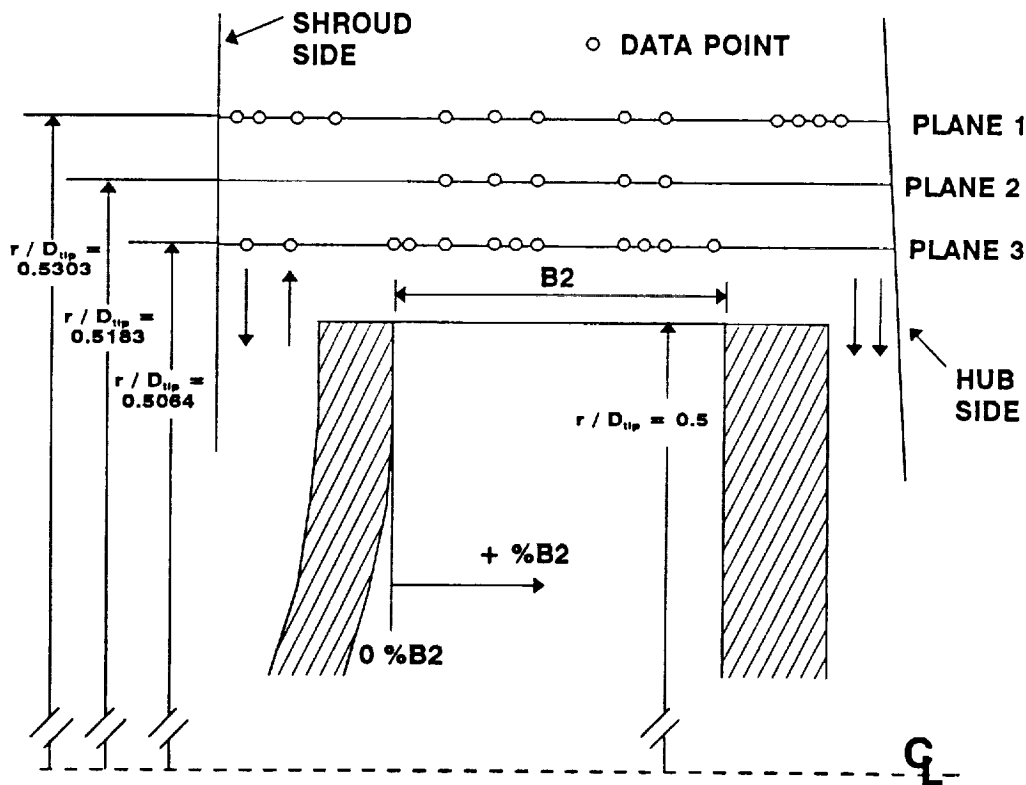


Figure 25 Sketch of Impeller Discharge Geometry and LDV Measurement Locations

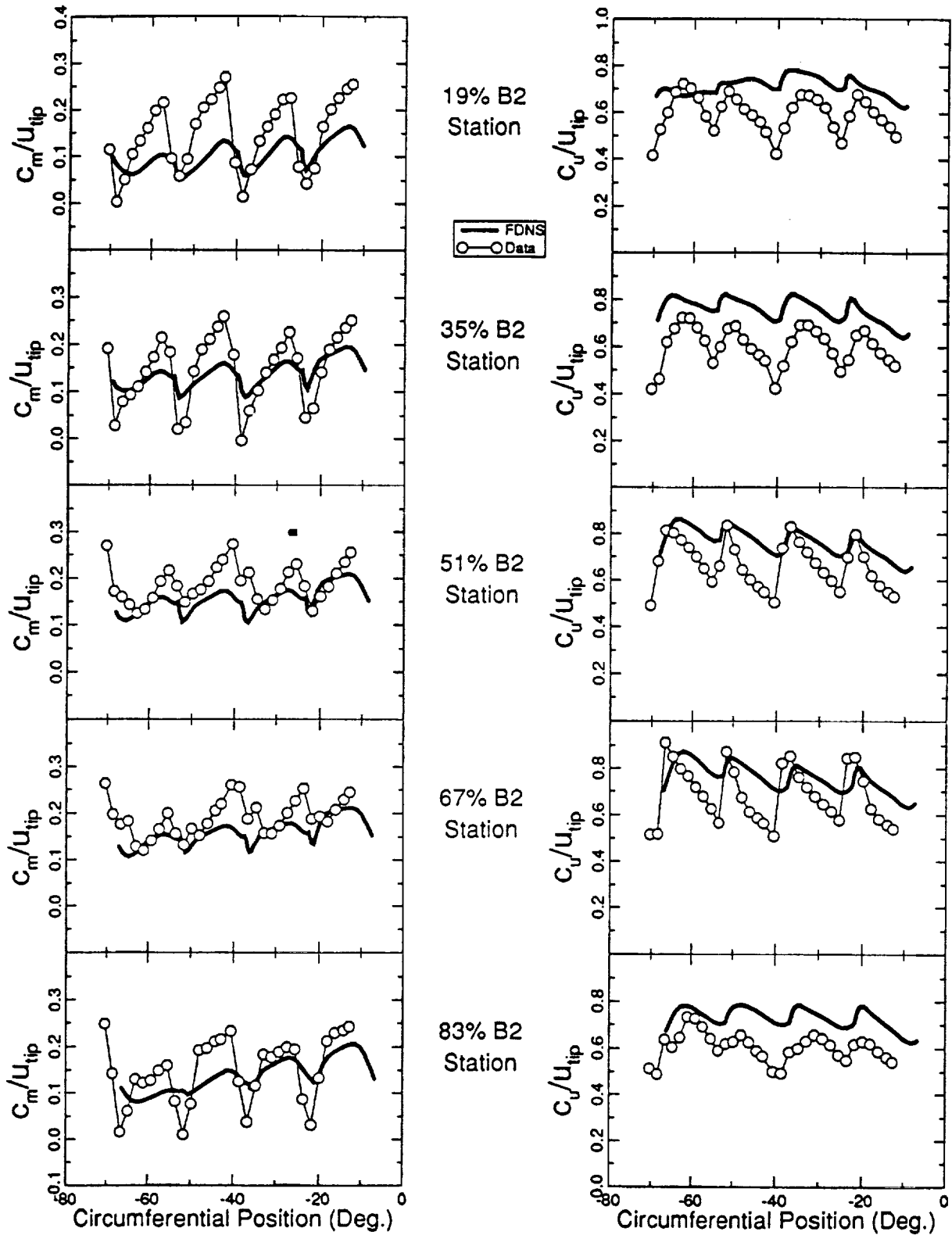


Figure 26 Data Comparisons for SSME HPFTP Impeller at Plane #1 ( $r/D_{tip} = 0.5064$ )

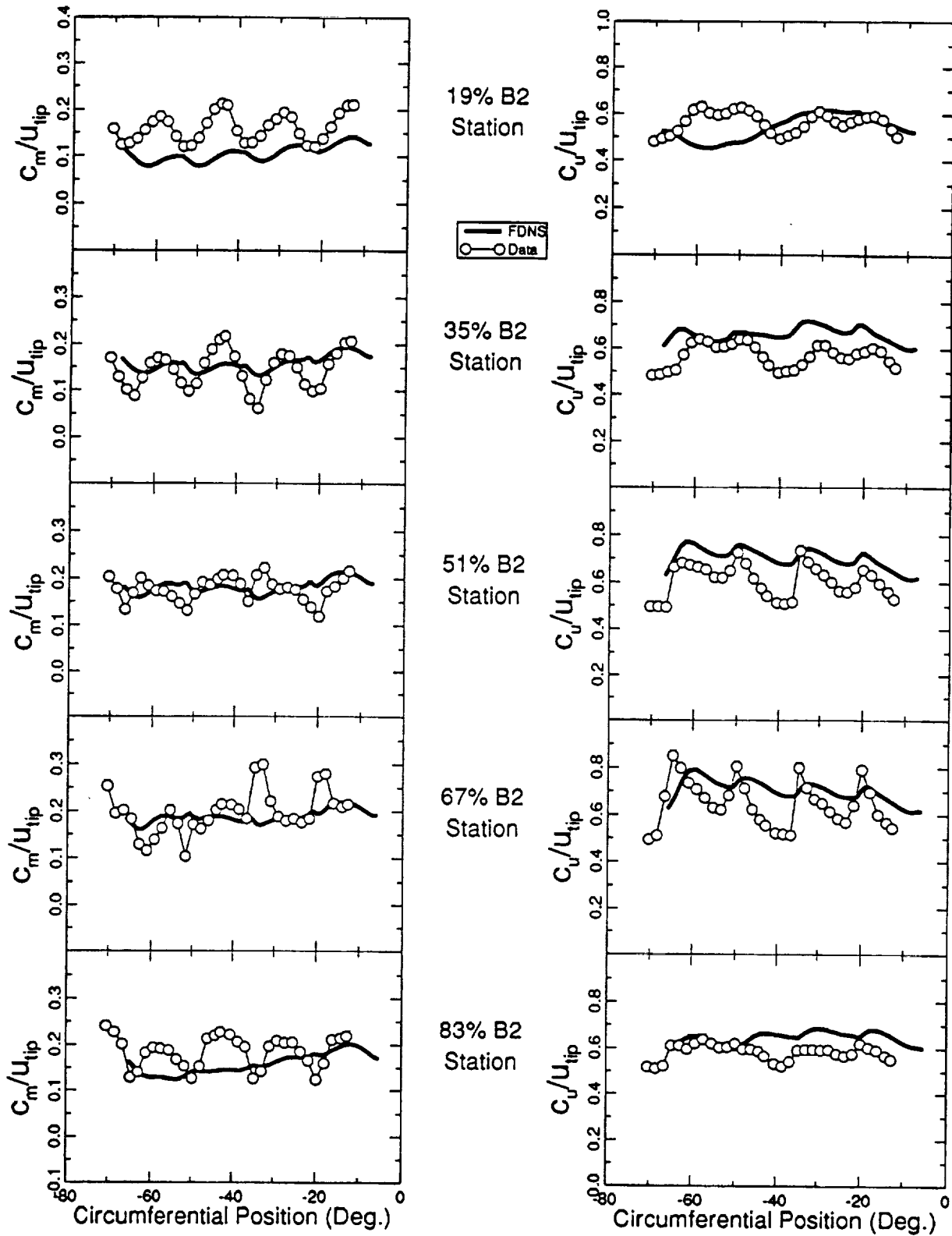


Figure 27 Data Comparisons for SSME HPFTP Impeller at Plane #2 ( $r/D_{tip} = 0.5183$ )

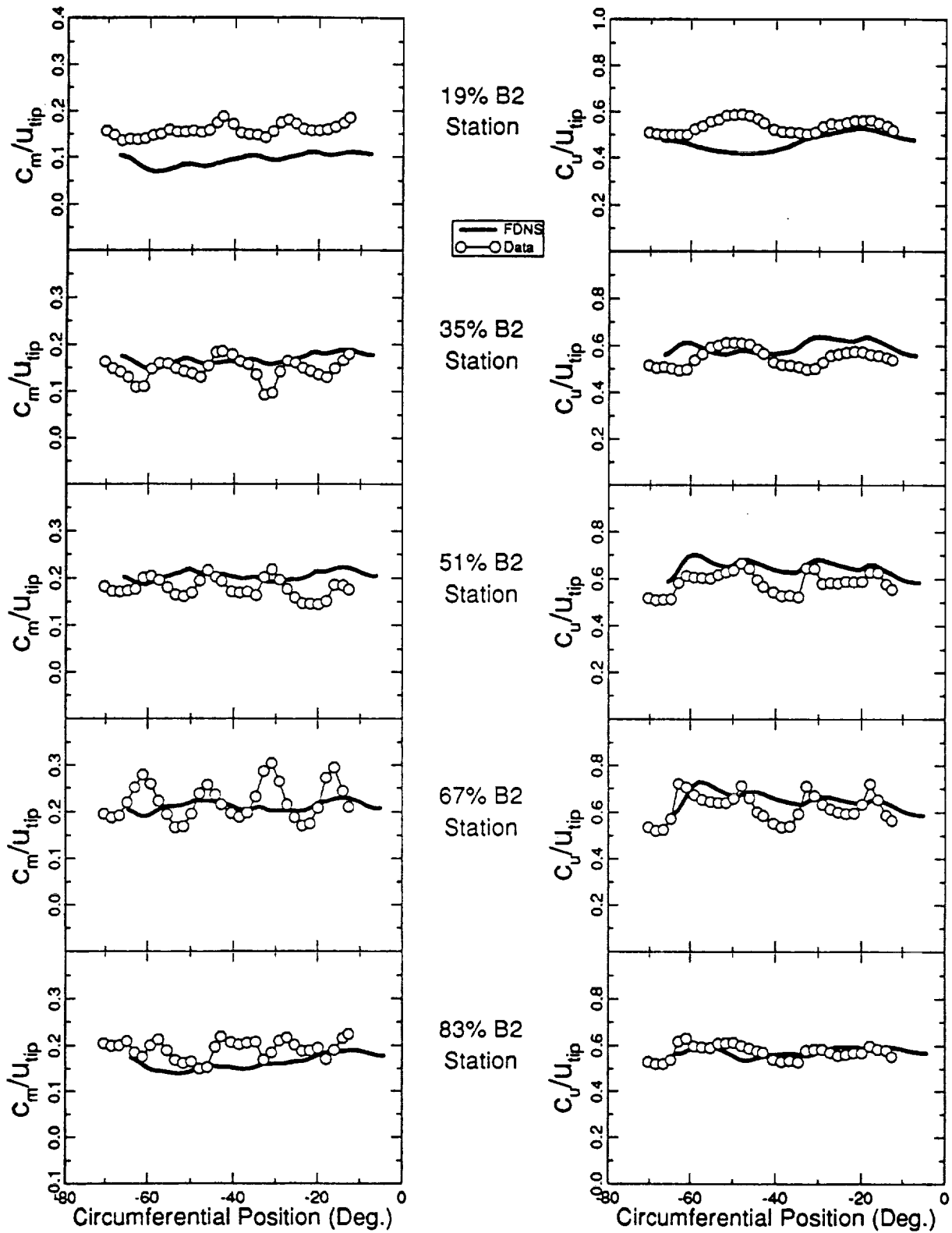


Figure 28 Data Comparisons for SSME HPFTP Impeller at Plane #3 ( $r/D_{tip} = 0.5303$ )

## 6.0 CONSORTIUM BASELINE VANED DIFFUSER FLOW STUDY

The pump consortium baseline vaned diffuser, designed to redirect the flow coming out of an impeller into a volute, consists of 13 vane islands in the circumferential direction. Since the diffuser exit flow will enter the volute, it is very difficult to define a set of proper downstream boundary conditions for the numerical simulation of the vaned diffuser alone without the volute. One way to solve this problem is to simulate impeller/volute interaction, but the required memory of this type of numerical analysis will be so large that it is too costly for the preliminary design. Hence, the effects of various downstream boundary conditions on the diffuser performance were investigated such that a better combination can be found for the numerical simulation of a diffuser without a downstream volute. The geometry of the cavity (hub-to-shroud) between the impeller exit and the diffuser was not defined, thus two different upstream boundary conditions without resolving the cavity were examined. There were seven cases examined for various upstream/downstream conditions in this study, and the boundary conditions for each case are listed in Table 8. The case #7 had identical boundary conditions as those of case #3, except the inlet turbulent kinetic energy was increased with a factor of ten.

Table 8 Numerical Analyses of Consortium Vaned Diffuser with Various Boundary Conditions

	Upstream Hub and Shroud B.C.	Downstream Hub and Shroud B.C.	Downstream Vane-to-Vane B.C.
Case #1	Fixed Wall	Fixed Wall	Fixed Wall
Case #2	Fixed Wall	Slip	Slip
Case #3	Fixed Wall	Fixed Wall	Periodic
Case #4	Fixed Wall	Slip	Periodic
Case #5	Slip	Fixed Wall	Periodic
Case #6	Slip	Slip	Periodic
Case #7	Fixed Wall	Fixed Wall	Periodic

The mesh system for the consortium baseline vaned diffuser was constructed to have three grid zones. Zone #1 consists of a 15 x 19 x 19 grid system and represents the gap between impeller discharge and the leading edge of diffuser vane. A 71 x 19 x 19 grid system was used for the flow passage between diffuser vanes and is denoted as zone #2. The third zone employs either 97 x 19 x 19 (for cases #1 and #2) or 97 x 39 x 39 (for cases #3-#7) grid points to discretize the downstream section of the vaned diffuser. The specification of grid system and boundary conditions for the consortium baseline vaned diffuser is plotted as shown in Figure 29 (hub-to-shroud), and in Figure 30 (vane-to-vane). The inlet flow conditions were simplified to be uniform for both the magnitude and the angle.

All numerical analyses of the vaned diffuser were conducted based on uniform inlet flow velocity (tangential component = 220 ft/sec) and flow angle ( $6.35^\circ$ ). The numerical results of the consortium baseline vaned diffuser indicated the flow separated within the diffuser vane passage near leeward (suction) surface, as can be seen in Figures 31-37. It is obvious that various boundary conditions affected the flow structure within the diffuser passage. The downstream boundary condition in the circumferential (vane-to-vane) direction seems to have a stronger effect on the diffuser flow than other boundary conditions. As can be seen from Figures 31-37, the periodic downstream boundary condition in the circumferential direction allows the diffuser exit flow to move in the circumferential direction, and thus the flow separation within the diffuser passage is reduced comparing to the fixed-wall or slip boundary conditions. In addition, the calculated diffuser exit flow with the periodic downstream boundary condition essentially followed the circumferential direction which is better for a downstream volute. However, the numerical results of all cases revealed that the flow tends to separate near the hub and shroud surfaces towards the leeward side. The primary reason for the flow separation near the suction side is that the vaned diffuser was designed based on  $10^\circ$  flow angle into the diffuser passage; while the present pump model predicted about  $8^\circ$  flow angle entering the vaned diffuser for various cases, which can be see in Figures 38-39. Based on the design condition, the diffusing angle (in the hub-to-shroud direction) on the leeward (suction) side is larger than that on the windward (pressure) side because the diffuser height on the leeward side expands later (pass the 'throat') at the designed flow angle.

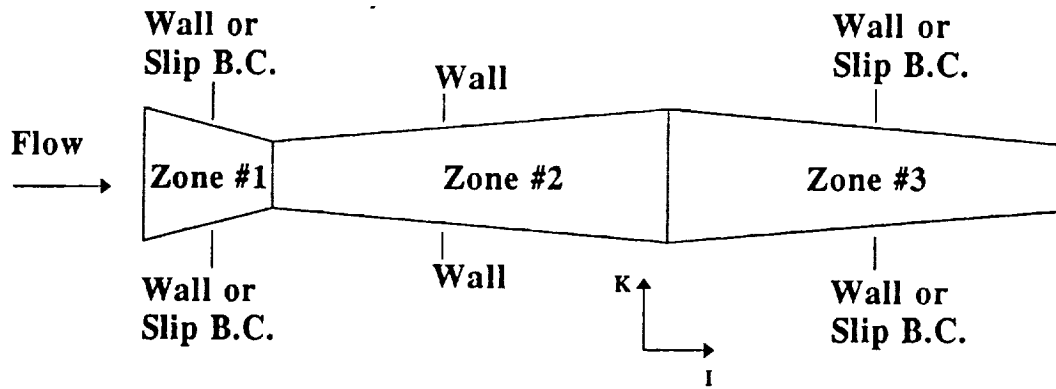
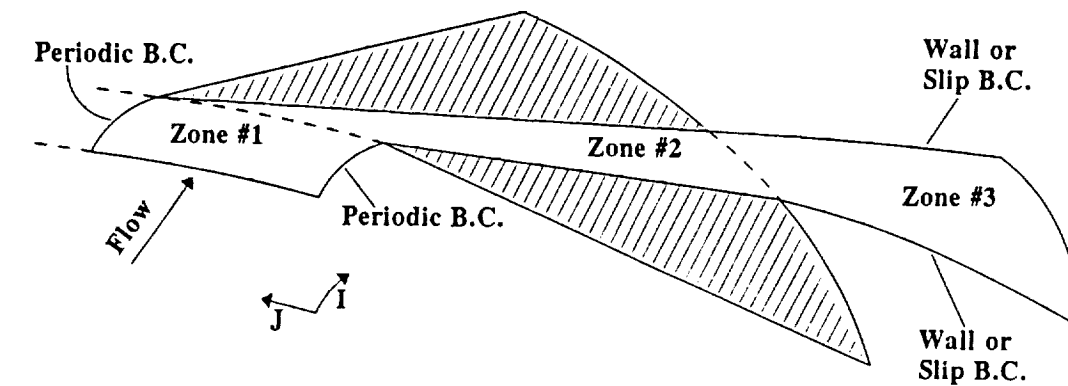
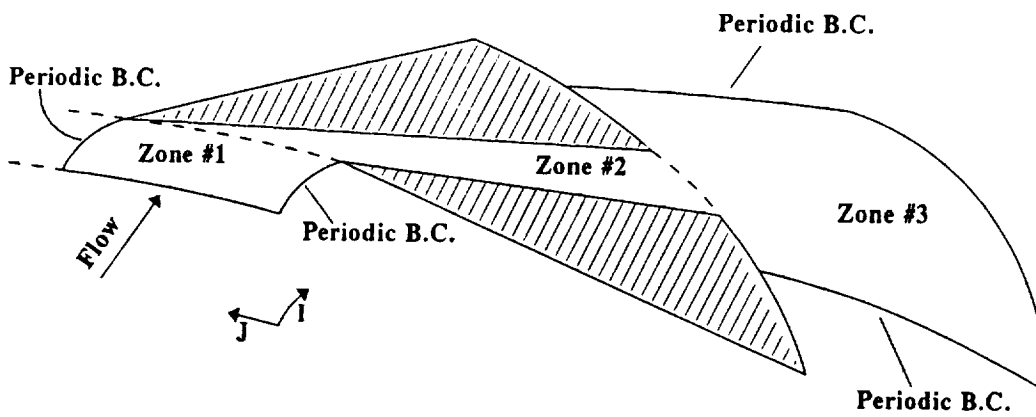


Figure 29 Boundary Condition Layout for the Consortium Vaned Diffuser (Hub-to-Shroud)

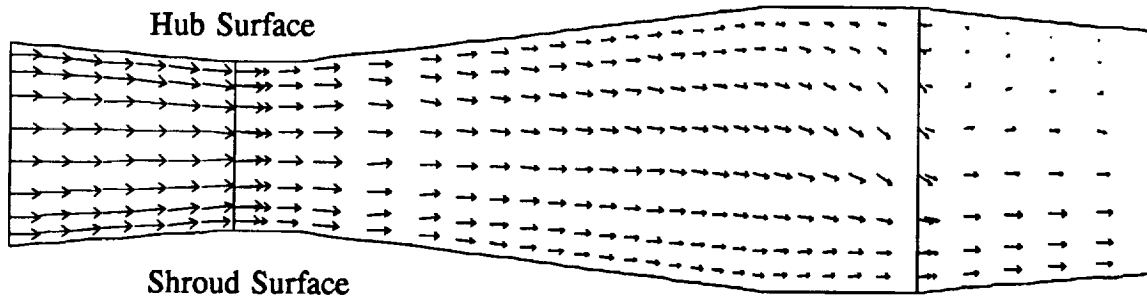


(a) Cases #1 and #2

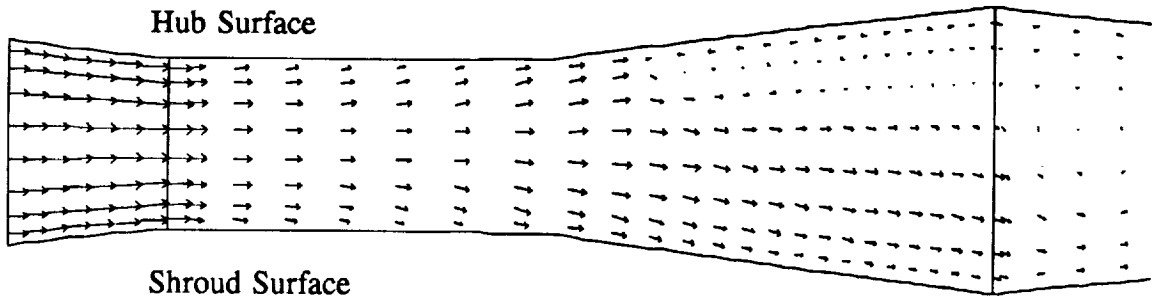


(b) Cases #3-#6

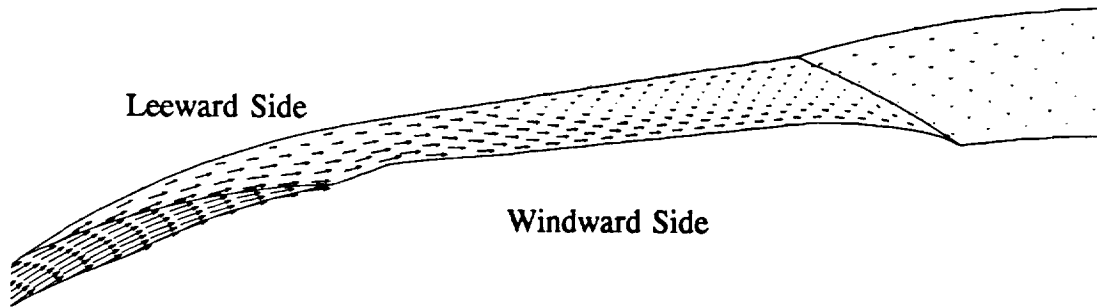
Figure 30 Boundary Condition Layout for the Consortium Vaned Diffuser (Circumferential)



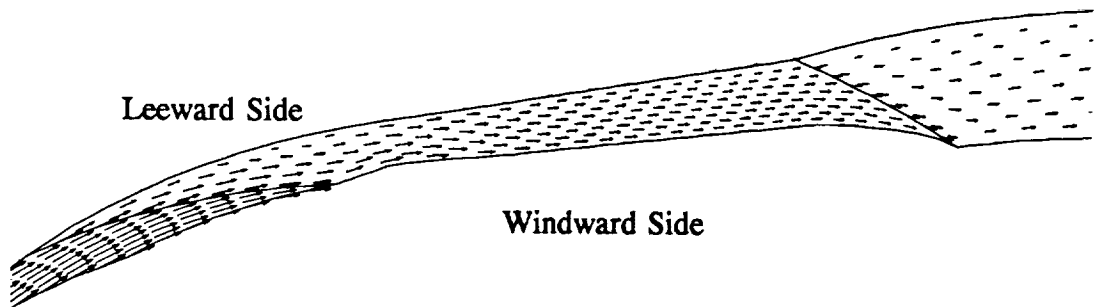
(a) Hub-to-Shroud Near Windward Surface



(b) Hub-to-Shroud Near Leeward Surface

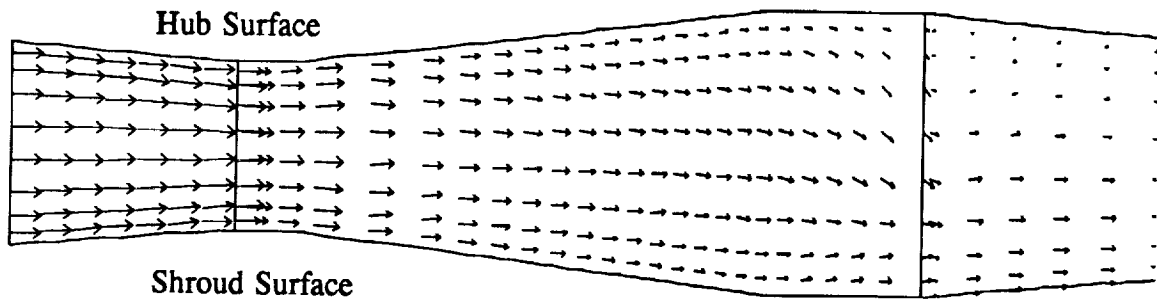


(c) Blade-to-blade Near Hub Surface

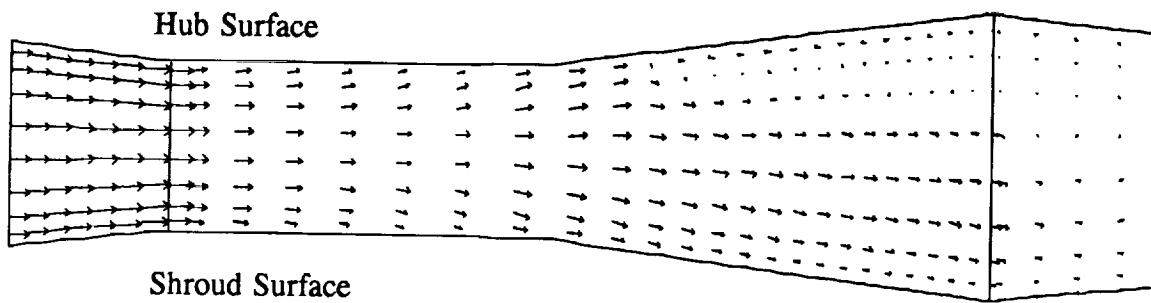


(d) Blade-to-Blade Near Shroud Surface

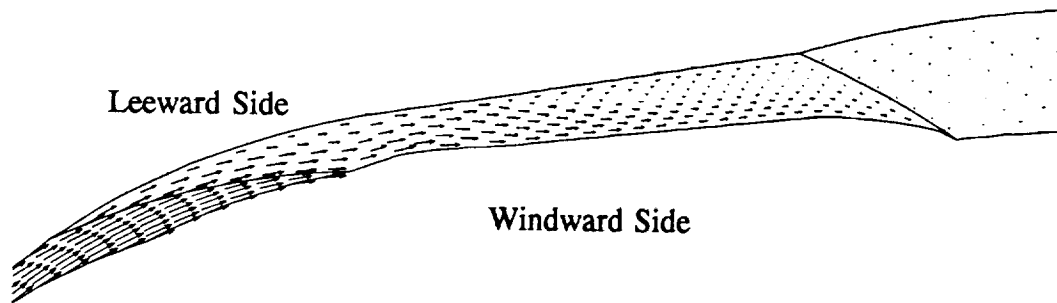
Figure 31 Velocity Vectors of the Consortium Vaned Diffuser Test Case #1



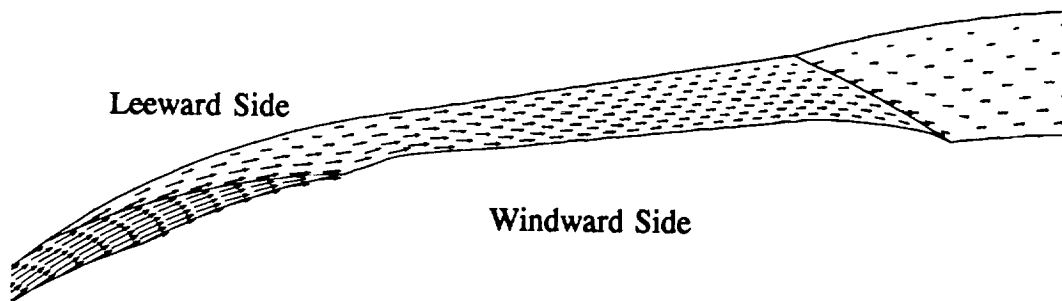
(a) Hub-to-Shroud Near Windward Surface



(b) Hub-to-Shroud Near Leeward Surface

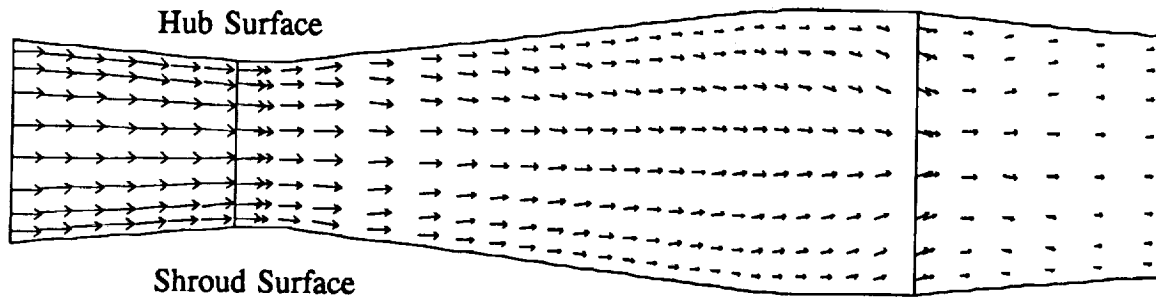


(c) Blade-to-blade Near Hub Surface

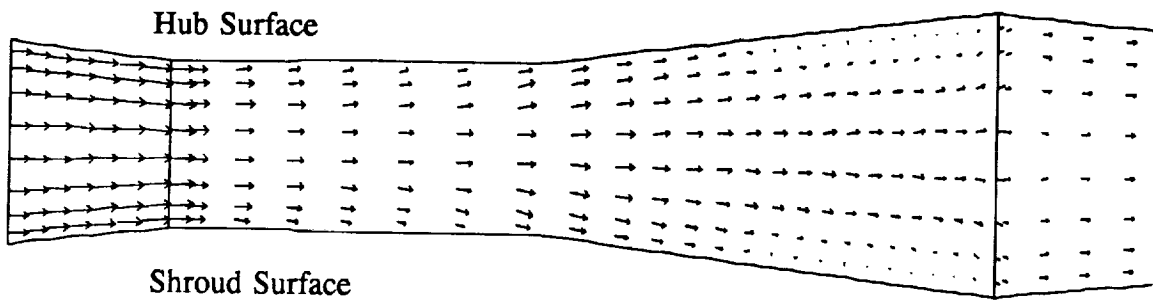


(d) Blade-to-Blade Near Shroud Surface

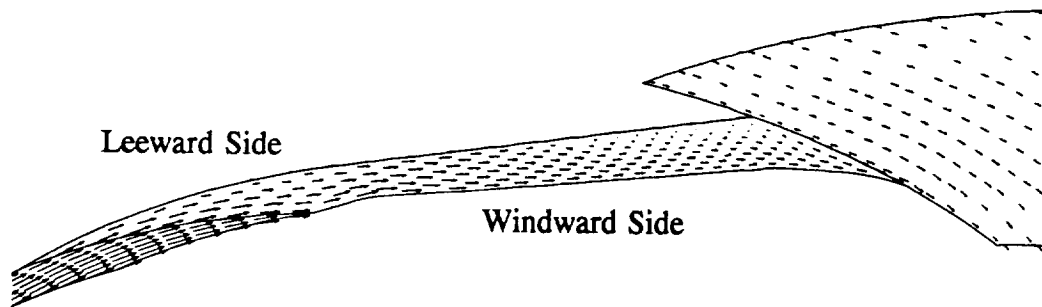
Figure 32 Velocity Vectors of the Consortium Vaned Diffuser Test Case #2



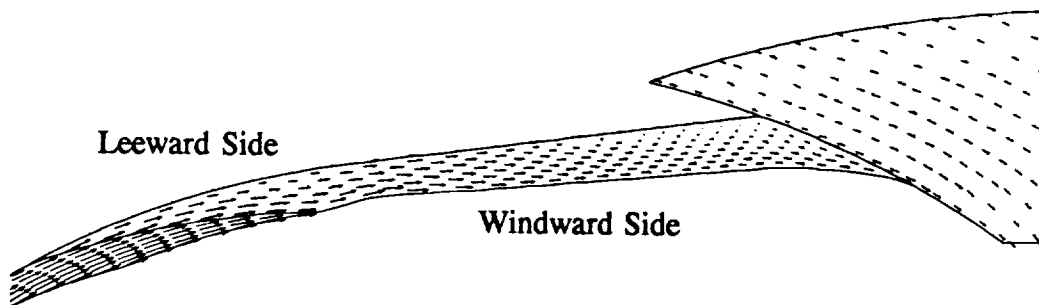
(a) Hub-to-Shroud Near Windward Surface



(b) Hub-to-Shroud Near Leeward Surface

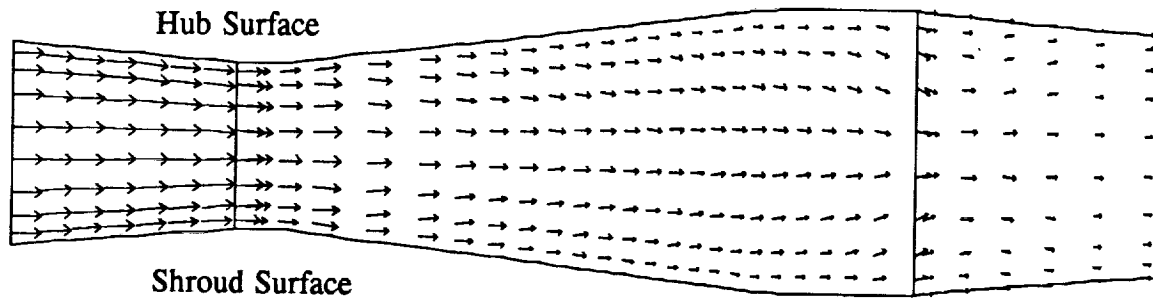


(c) Blade-to-blade Near Hub Surface

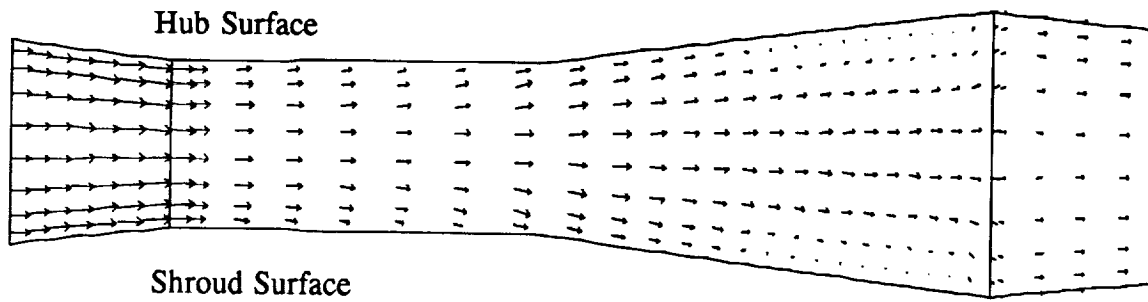


(d) Blade-to-Blade Near Shroud Surface

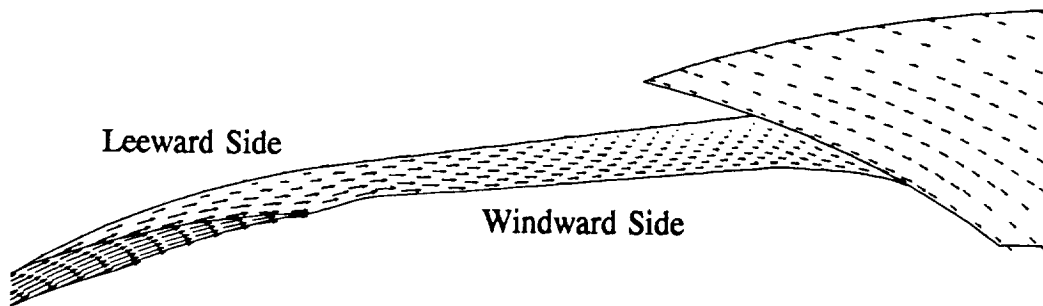
Figure 33 Velocity Vectors of the Consortium Vaned Diffuser Test Case #3



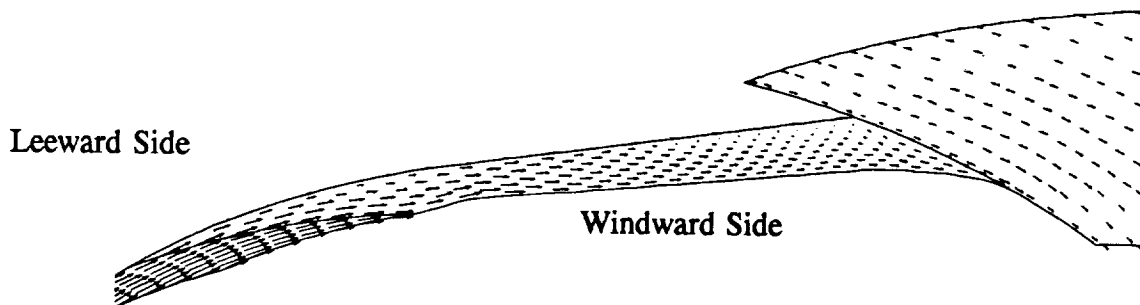
(a) Hub-to-Shroud Near Windward Surface



(b) Hub-to-Shroud Near Leeward Surface

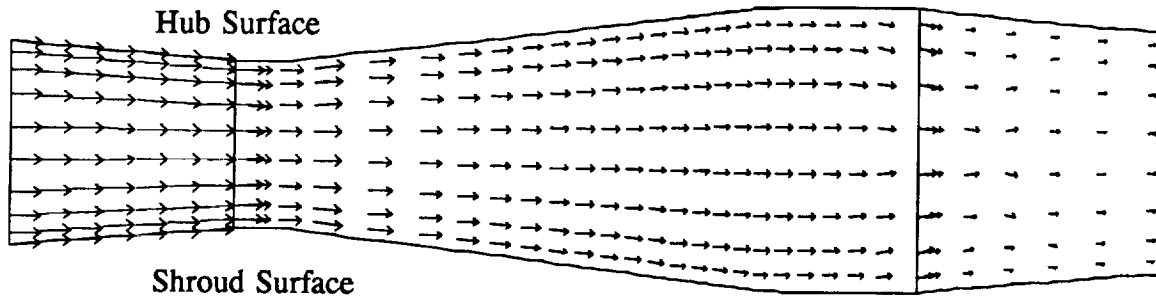


(c) Blade-to-blade Near Hub Surface

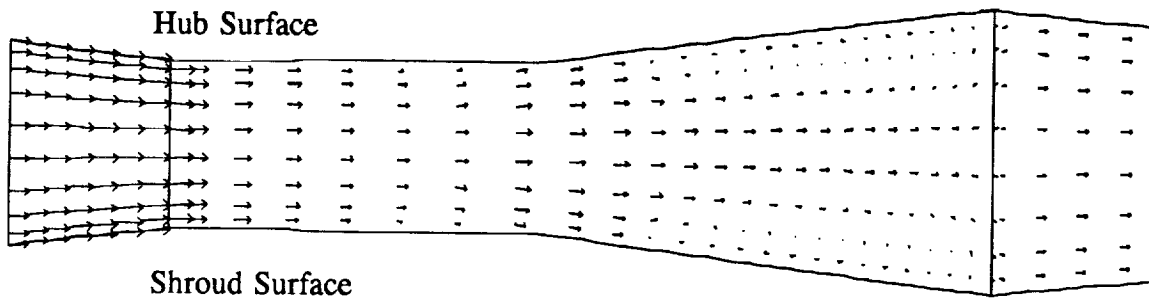


(d) Blade-to-Blade Near Shroud Surface

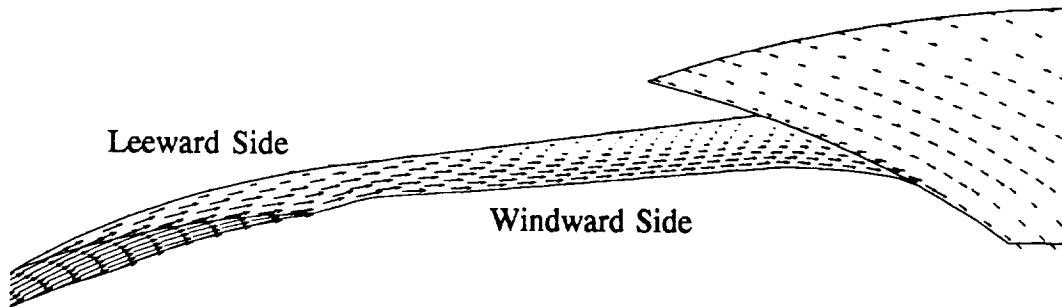
Figure 34 Velocity Vectors of the Consortium Vaned Diffuser Test Case #4



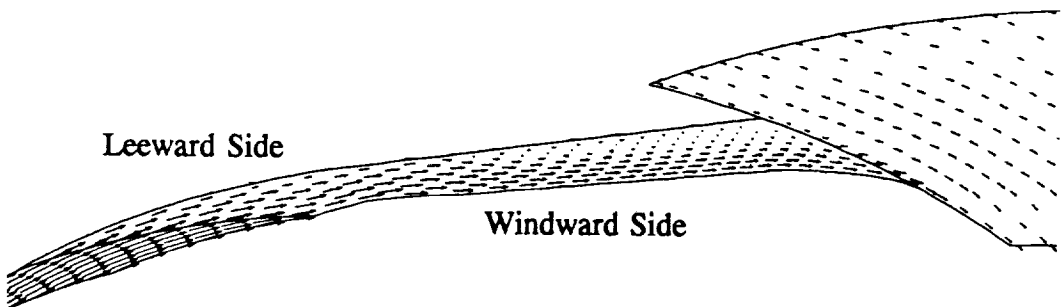
(a) Hub-to-Shroud Near Windward Surface



(b) Hub-to-Shroud Near Leeward Surface

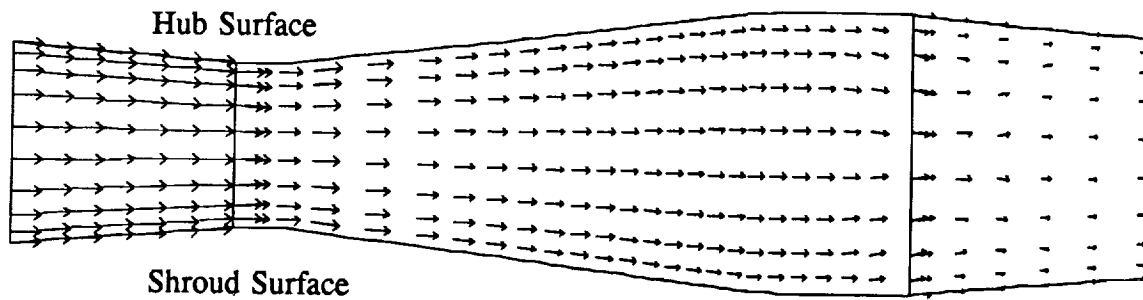


(c) Blade-to-blade Near Hub Surface

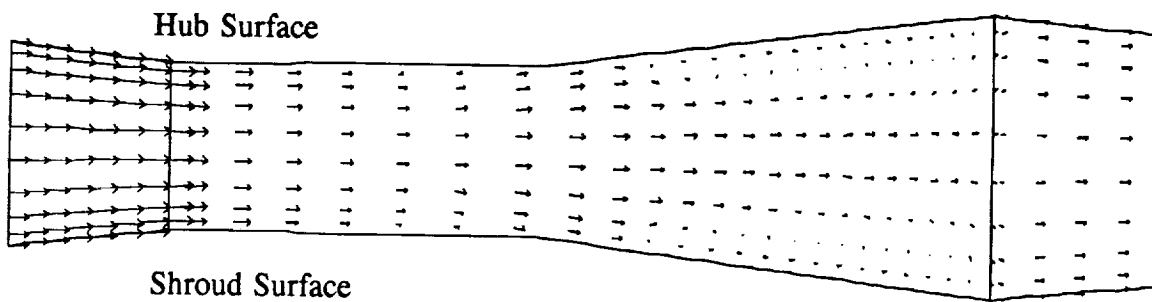


(d) Blade-to-Blade Near Shroud Surface

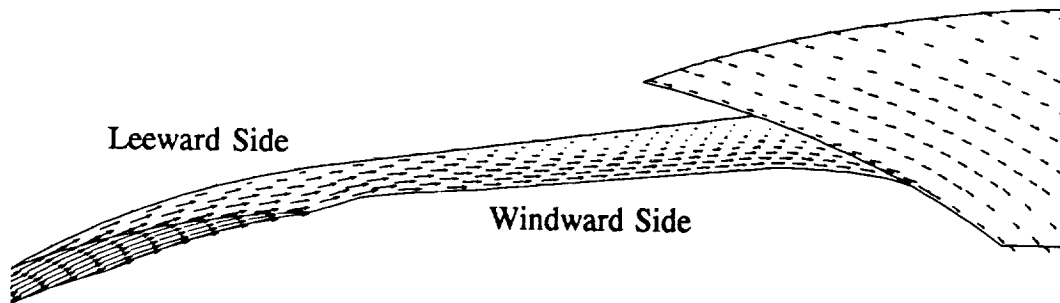
Figure 35 Velocity Vectors of the Consortium Vaned Diffuser Test Case #5



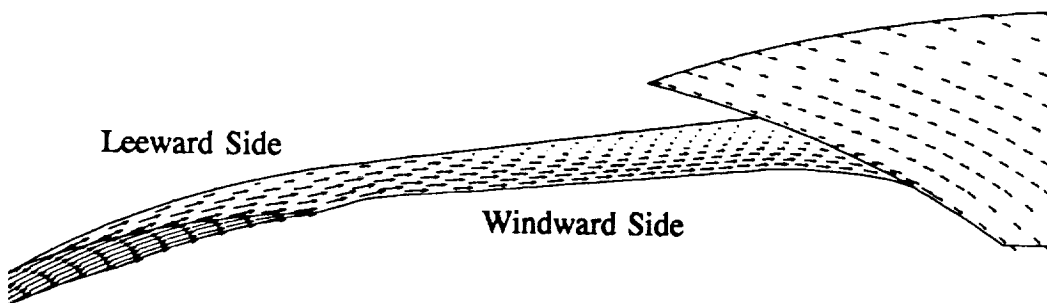
(a) Hub-to-Shroud Near Windward Surface



(b) Hub-to-Shroud Near Leeward Surface

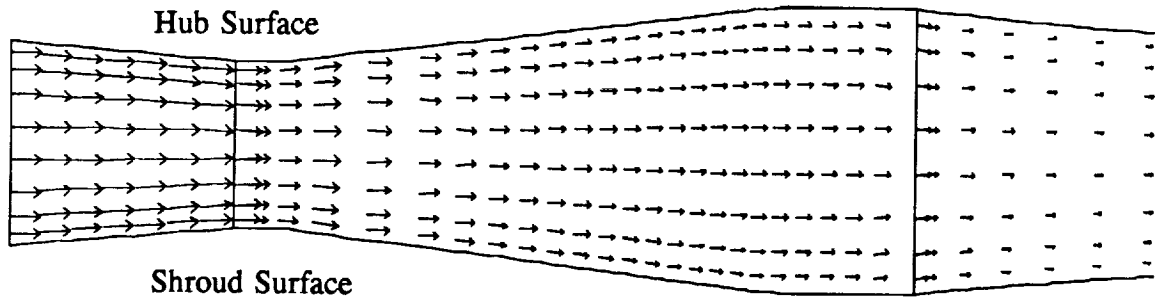


(c) Blade-to-blade Near Hub Surface

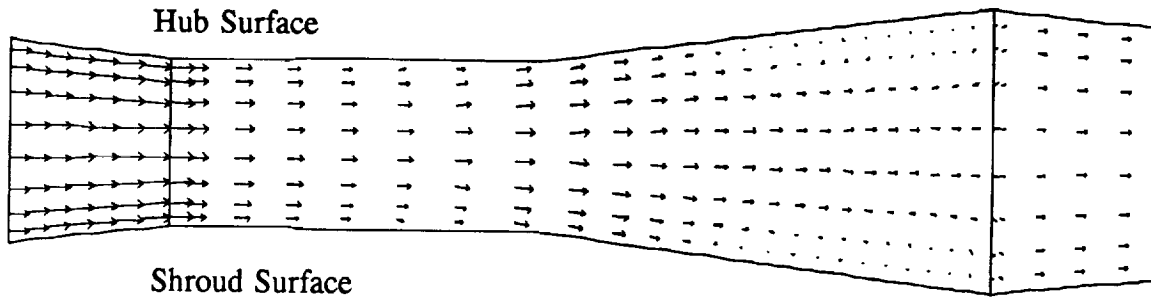


(d) Blade-to-Blade Near Shroud Surface

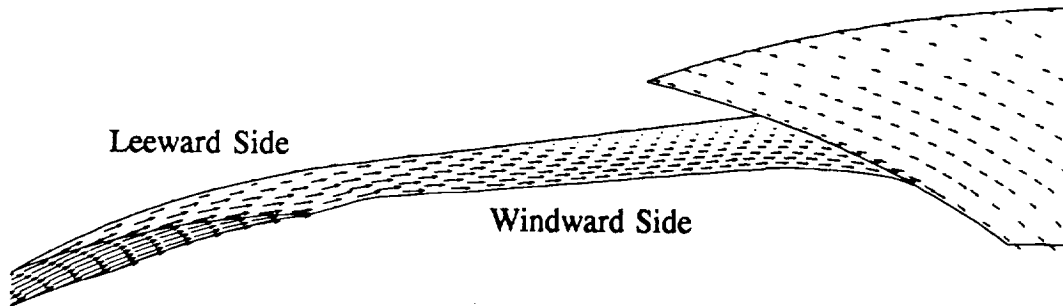
Figure 36 Velocity Vectors of the Consortium Vaned Diffuser Test Case #6



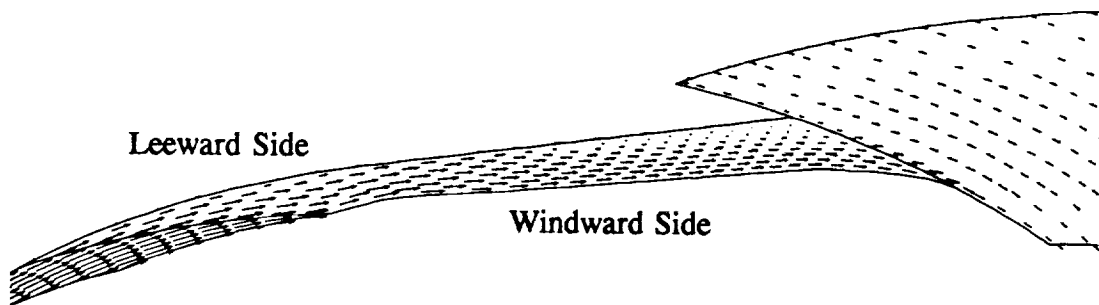
(a) Hub-to-Shroud Near Windward Surface



(b) Hub-to-Shroud Near Leeward Surface



(c) Blade-to-blade Near Hub Surface



(d) Blade-to-Blade Near Shroud Surface

Figure 37 Velocity Vectors of the Consortium Vaned Diffuser Test Case #7

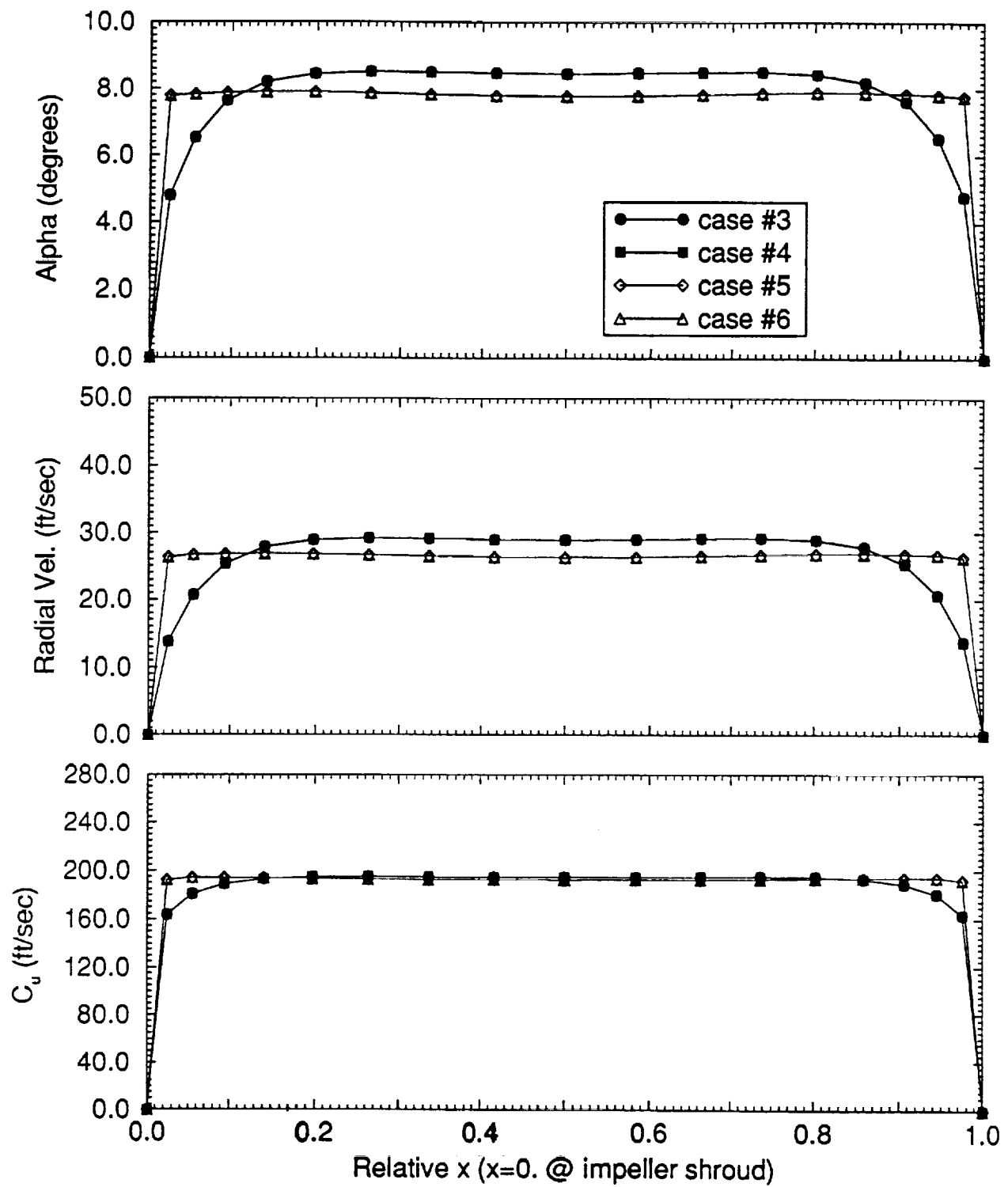


Figure 38 Circumferentially Averaged Inlet Velocity Profiles and Flow Angles

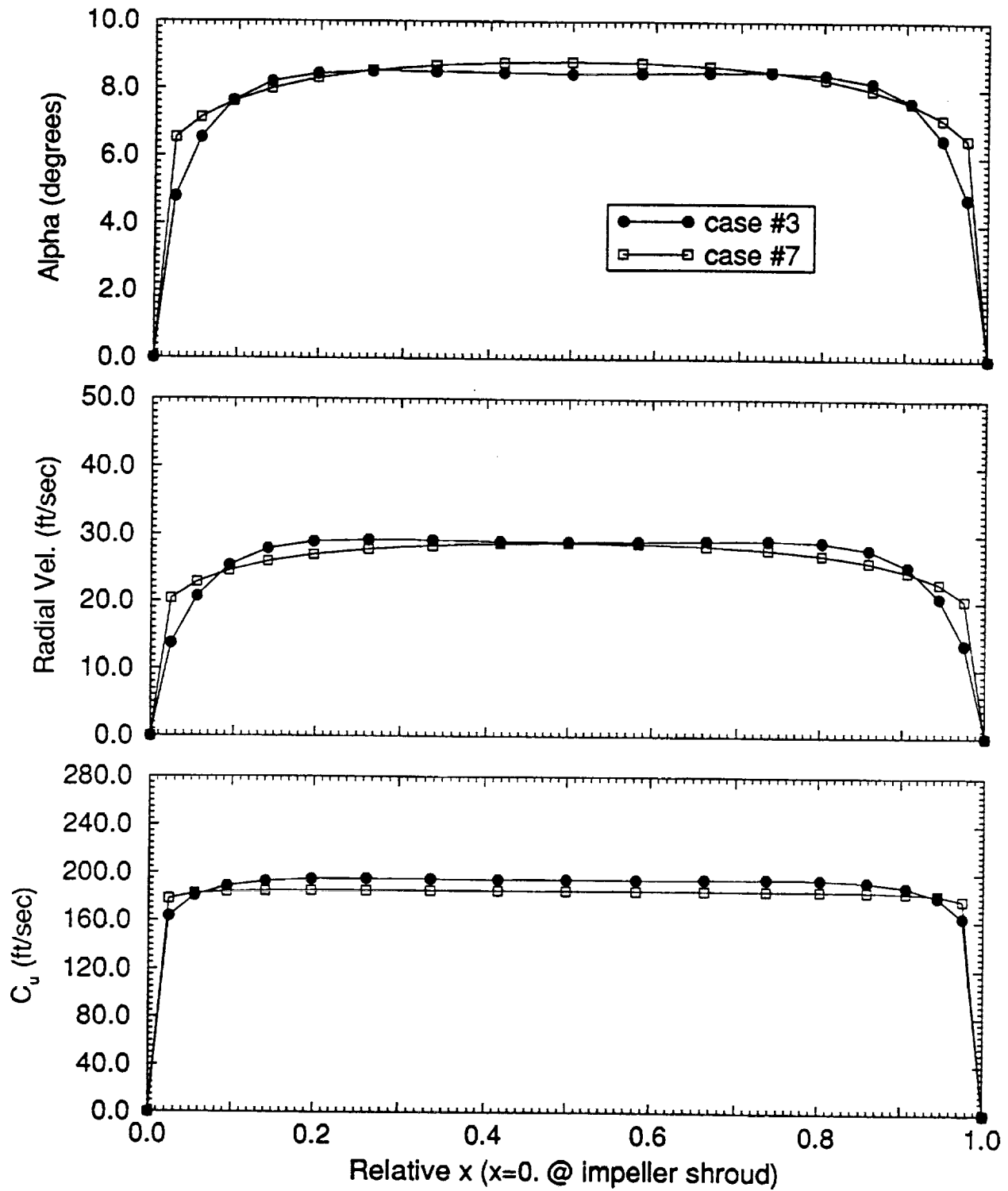


Figure 38 The Effect of Inlet Turbulence Kinetic Energy on Inlet Flow Profiles

The upstream boundary condition was shown to have an effect on the boundary layer thickness of the flow (and so the flow angle) entering the diffuser, and thus influenced the flow separation in the diffuser passage. As can be seen in Fig. 38, the upstream slip hub/shroud boundary condition (cases #5 & #6) generated a much thinner boundary layer and so a smaller flow angle into the diffuser passage than that with the fixed hub/shroud wall boundary condition (cases #3 & #4). Consequently, a larger flow separation was calculated in cases #5 & #6. According to this observation, another test case (#7) with a larger inlet turbulent kinetic energy was simulated. The result as shown in Figure 39 indicates that larger inlet turbulence intensity created a larger shear stress and retarded the tangential velocity more such that the flow angle into the diffuser passage was increased. However, the change was insignificant, and it is because the increase of turbulent kinetic energy with a factor of ten only contributes three times amplification of the eddy viscosity. A test case with larger inlet turbulence length scale may provide more insight into the effect of inlet turbulence conditions. The diffuser performance for various boundary conditions is plotted as shown in Figure 40. It is obvious that the case with smaller flow separations has higher static pressure rise and smaller total pressure loss. Conversely, higher inlet turbulence intensity results in lower static pressure rise and larger total pressure loss. However, the differences are so small that the diffuser performance can be concluded to be insensitive to the boundary conditions. The averaged static pressure ratio and total pressure loss between the diffuser exit plane and the impeller exit plane for the consortium baseline vaned diffuser with various boundary conditions are also listed in Table 9. It can be seen that the total pressure loss through the vaned diffuser is small for all cases.

Table 9 The Calculated Diffuser Performance of the Consortium Baseline Vaned Diffuser

	case #1	case #2	case #3	case #4	case #5	case #6	case #7
Static pressure rise	31.6%	33.3%	32.4%	32.5%	30%	30%	30.1%
Total pressure loss	13.5%	12.5%	11.2%	11.2%	13.3%	13.3%	13.6%

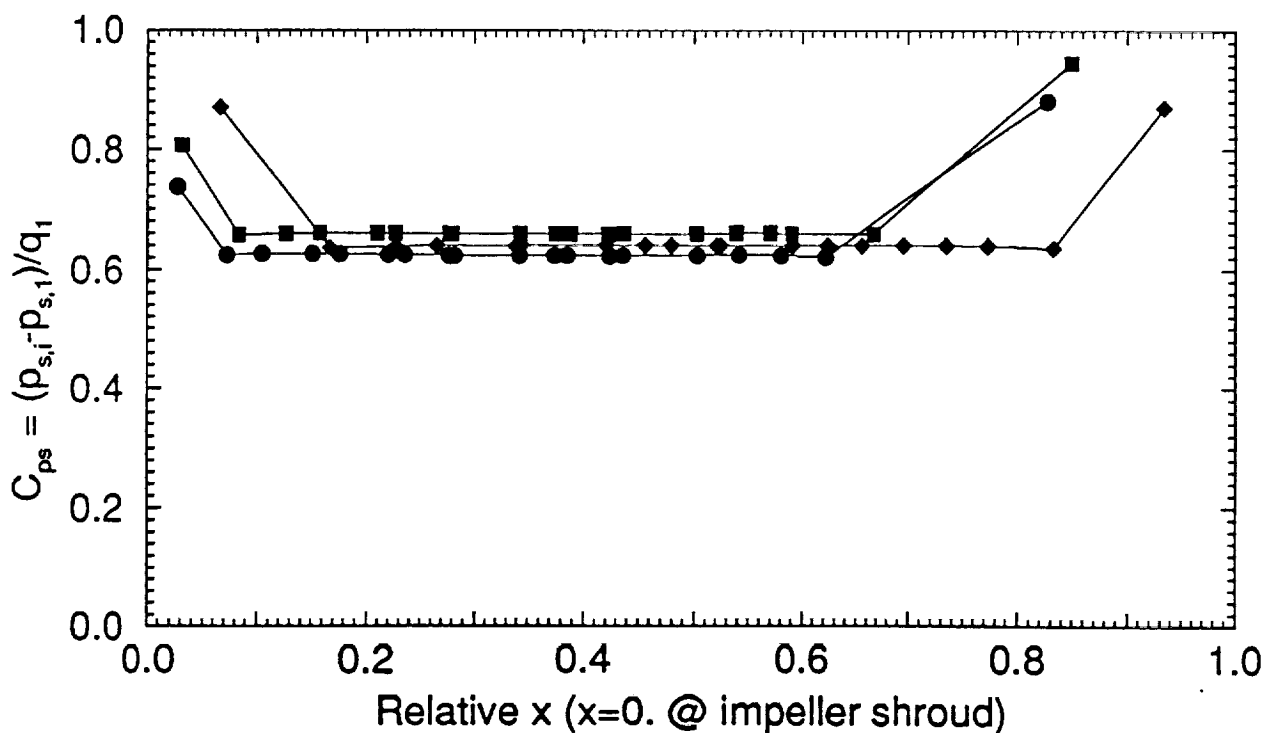
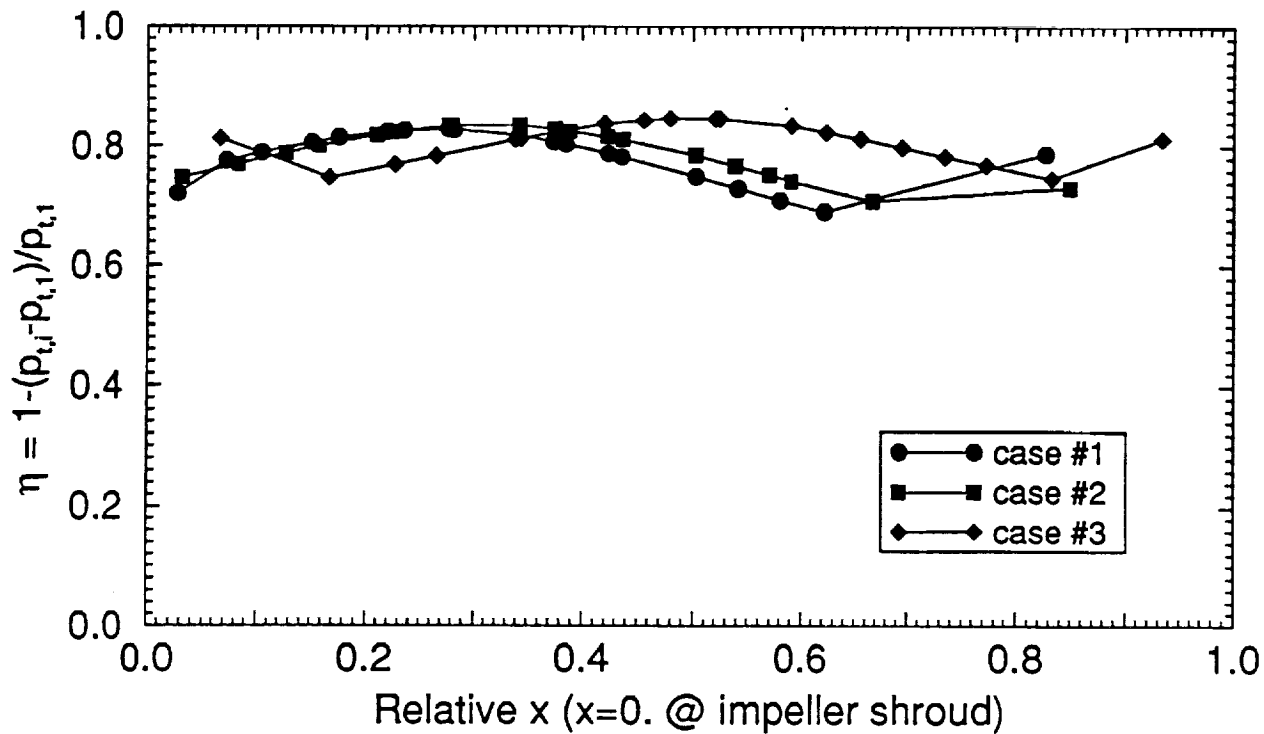


Figure 40 Circumferentially Averaged Diffuser Performance for Various Boundary Conditions

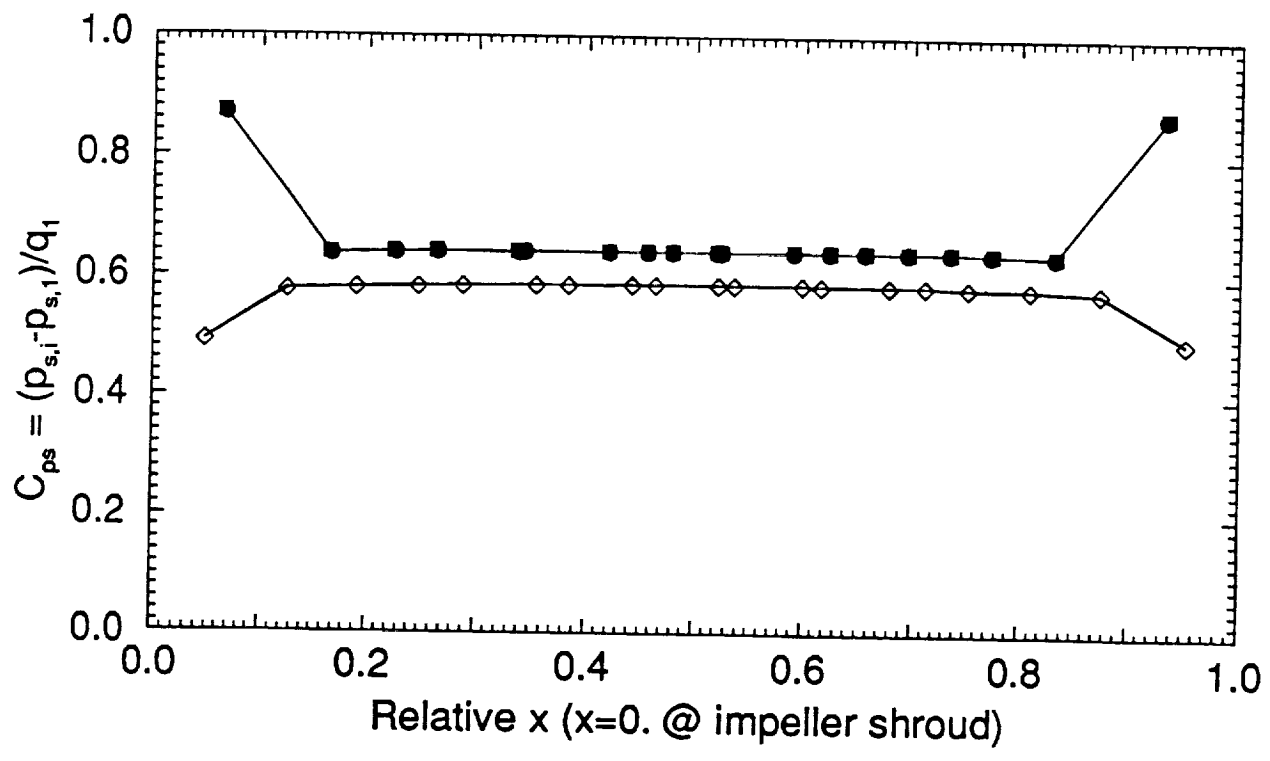
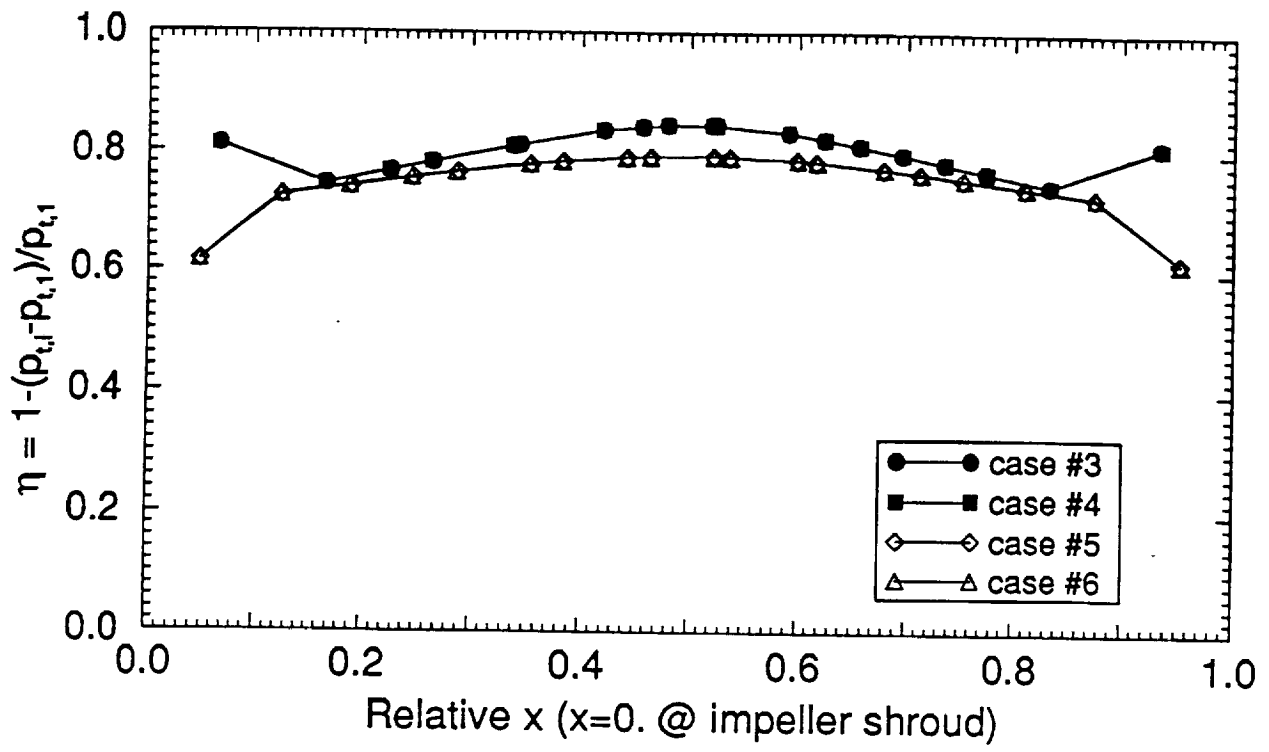


Figure 40 Continued

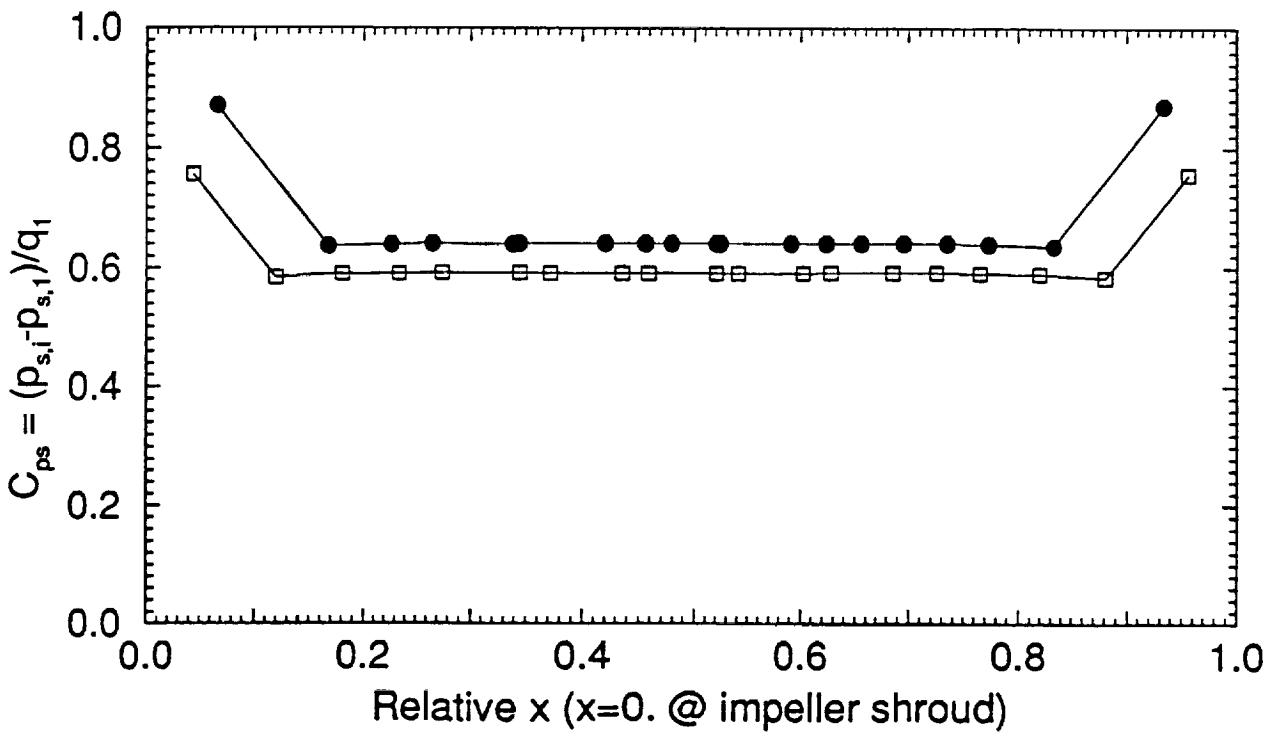
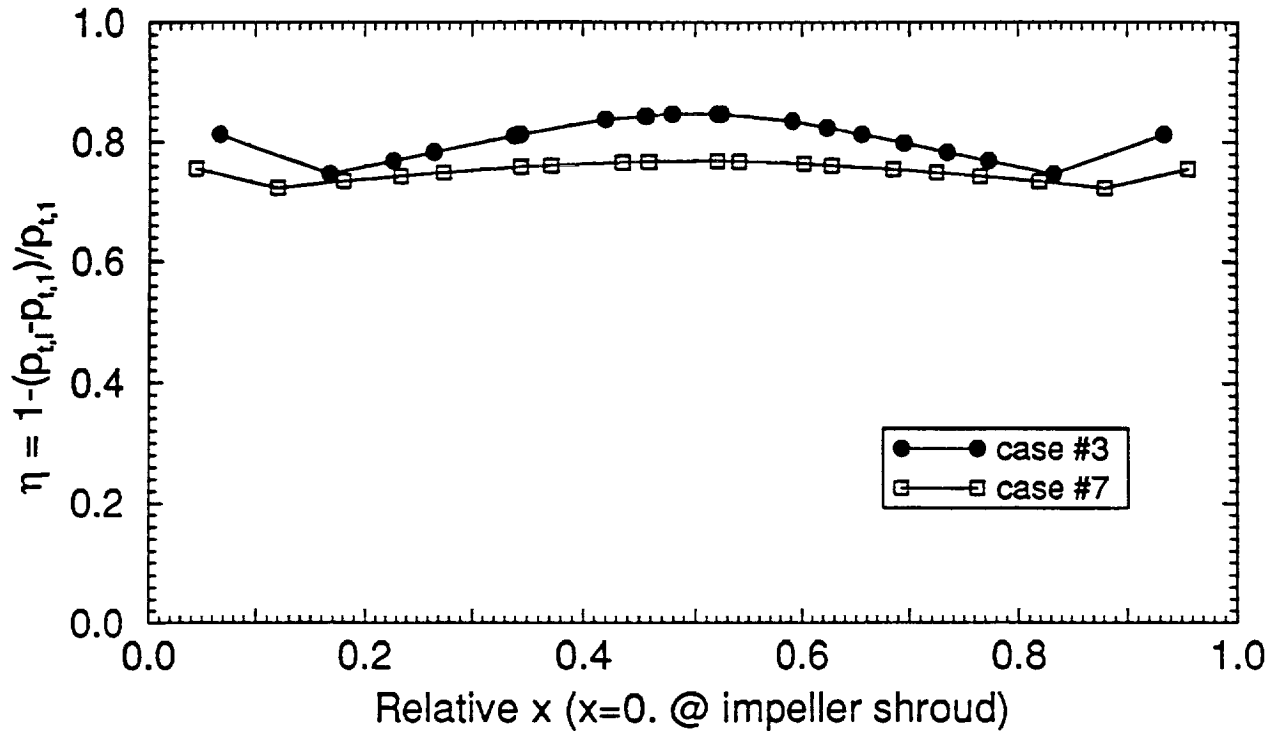


Figure 40 Continued

## 7.0 CONCLUSIONS AND RECOMMENDATIONS

An effective and robust CFD pump model was developed, based on the FDNS flow solver, as an analytical tool for the pump design. Numerical simulations using the present CFD pump model have been benchmarked with the experiments from Rocketdyne for the pump inducer and SSME HPFTP impeller flows. The CFD pump model also has been used to analyze the consortium impeller and diffuser, and the results used to provide recommendations for improved design. The FDNS flow solver has been proved to be an efficient CFD pump model due to its very compact numerical structure (requiring small memory) and fast turnaround computing time. In spite of minor deficiencies caused by the grid meshes and by the numerical techniques, the present model is useful as a pump design tool.

For the inducer test case, the numerical calculation predicts general flow features and provides good agreement with the test data except at the downstream region. The inaccuracy of predicting the downstream wake can be improved by using a very tight grid system in the tip clearance region and downstream of the inducer blade trailing edge. In addition, the turbulence model can be improved in order to accurately predict tip leakage flows of the unshrouded inducer.

The numerical simulations of the consortium impeller demonstrated the advantages of effectively using CFD analyses in the design process. Several parametric studies on various geometric features, which included TANDEM blade concept, impeller exit blade lean, the chord length of the partial blade, and the circumferential location of the partial blade leading edge, were conducted by the pump consortium members. The results of the TANDEM blade study were included in this report. An advanced concept design impeller was designed based on the results concluded from the parametric study. The numerical results indicated that the performance of the advanced concept impeller was greatly increased comparing to the baseline impeller. Hence, the present CFD pump model was proved to be an efficient analytical tool for pump design.

For the SSME HPFTP impeller test case, the present pump model qualitatively predicts the characteristics of impeller discharge flows. A more uniform flow split at the exit of impeller blades can be predicted if a grid refinement is made to resolve the bluntness of the blade leading edge. Nevertheless, the accuracy in predicting the impeller discharge flow into the diffuser, which is roughly located between test plane #2 and plane #3, is most critical in the impeller design. The numerical simulation shows good agreement with the test data at plane #3. To improve the detailed flow comparison near the impeller exit, several modifications can be made to the numerical analysis, such as 1) more grid points for the impeller discharge cavity, 2) inclusion of the trailing edge thickness of impeller blades, and 3) proper boundary conditions for cavity surfaces at the impeller discharge. Furthermore, it was found through the validation process of the proposed CFD pump model, the current non-staggered grid technique has a minor problem of slow convergence rate near the converging stage in computing the impeller flow. This may be due to the fact that the non-staggered grid scheme lacks numerical cross-stream damping which is critical in the pressure-driven impeller flow. Historically, during the FDNS developing process, a staggered grid methodology was employed and tested, such a grid can maintain a relatively small convergence oscillation in a flowfield with large cross-stream gradients. Hence, a staggered grid approach may be considered in simulating the impeller flow, even though such a scheme is known to produce more artificial damping.

Another minor deficiency of the present pump model is that the periodic boundary condition is treated explicitly, i.e. the periodic boundary is not linked to the flowfield in the matrix solver for the governing equations. This is caused by the numerical framework of the present model, where the velocity components in the Cartesian coordinates are solved sequentially (explicitly). This deficiency prevents the present model from simulating an unsteady pump problem with periodic boundary conditions, and might slow down the convergence rate. There are two ways to implement an implicit periodic boundary condition in the present pump model. The first one is to modify the present pump model to solve the governing equations for those two velocity vectors in the periodic direction simultaneously such that the matrix coefficients of those two velocity components can be linked in the whole computational domain; however, the required computer memory will be increased. The second way is to modify the

present pump model to solve the velocity components in the cylindrical coordinates. It is also concluded from the present study that though the turbulence model used in the present pump model is not very sensitive to the near-wall grid spacing, a convergence oscillation might occur if the spacing is too large.

The numerical results of vaned diffuser study revealed that the diffuser performance is very insensitive to the boundary conditions because it is a pressure-driven flow. However, the effect of boundary conditions is critical in simulating detailed flow structure such as the location and the size of flow separation and diffuser exit flow angle.

Despite some deficiency of the present pump model, the turn-around time is short and the required computer memory is small such that the present pump model is a very good analysis tool in the design process. This can be seen from the result of pump consortium impeller flow analysis, and its impact on the impeller design.

## REFERENCES

1. Chen, Y. S., "Compressible and Incompressible Flow Computations with a Pressure Based Method," AIAA Paper 89-0286, AIAA 27th Aerospace Sciences Meeting, Jan. 9-12, 1989.
2. Chen, Y.S., "FDNS, A General Purpose CFD Code, User's Guide-- Version 3.0," ESI-TR-93-01, Engineering Sciences, Inc., Huntsville, AL, May, 1993.
3. Cheng, G.C., Chen, Y.S., Garcia, R., and Williams, R.W., "Numerical Study of 3-D Inducer and Impeller for Pump Model Development," AIAA Paper 93-3003, AIAA 24th Fluid Dynamics Conference, Orlando, Florida, July, 1993.
- ✓ 4. Chen, Y.S., and Kim, S.W., "Computation of Turbulent Flows Using an Extended k-ε Turbulence Closure Model," NASA CR-179204, 1987.
5. Liakopoulos, A., "Explicit Representations of the Complete Velocity Profile in a Turbulent Boundary Layer," AIAA Journal, 22, pp. 844-846, June 1984.
6. Monson, D.J., Seegmiller, H.L., McConnaughey, P.K., and Chen, Y.S., "Comparison of Experiment with Calculations Using Curvature-Corrected Zero and Two Equation Turbulence Models for a Two-Dimensional U-Duct," AIAA Paper 90-1484, AIAA 21st Fluid Dynamics, Plasma Dynamics and Lasers Conference, June 18-20, 1990.
7. Anon., "CFD Code Validation Inducer Data," Data Presented by Rocketdyne in the NASA/MSFC Pump Stage Technology Team Meeting, Jan. 1991.
8. Chen, Y.S., Cheng, G.C., and Williams, R.W., "Inducer Analysis/Pump Model Development," 9th Workshop for Computational Fluid Dynamic Applications in Rocket Propulsion, April, 1991.
9. Williams, R.W., "Pump Stage Technology Team Inducer Code Validation Velocity and Performance Comparison," Pump Team Meeting, NASA/MSFC, Oct. 1991.
- ✓ 10. Cheng, G.C., Chen, Y.S., and Williams, R.W., "CFD Analysis of Pump Consortium Impeller," NASA CP-3163, Part 1, 1992.
- ✓ 11. Cheng, G.C., Chen, Y.S., Garcia, R., and Williams, R.W., "CFD Parametric Study of Consortium Impeller," NASA CP-3221, Part 1, 1993.
12. Garcia, R., McConnaughey, P., and Eastland, A., "Computational Fluid Dynamics Analysis for the Reduction of Impeller Discharge Flow Distortion," AIAA Paper 94-0749, AIAA 32nd Aerospace Sciences Meeting & Exhibit, Jan. 10-13, 1994.

- ✓13. "NRA Pump CFD Code Validation Tests Status Summary," Data Presented by Rocketdyne in the NASA/MSFC Pump Stage Technology Team Meeting, Apr. 1992.
- ✓14. Brozowski, L.A., "Pump CFD Code Validation Tests-- Test Series 1 Summary Report," Rocketdyne Report RI/RD 92-175 under NASA Contract NAS8-38864, October, 1992.



# Report Documentation Page

1. Report No.	2. Government Accession No.	3. Recipient's Catalog No.	
4. Title and Subtitle  INDUCER ANALYSES/PUMP MODEL DEVELOPMENT		5. Report Date March, 1994	6. Performing Organization Code
		8. Performing Organization Report No. SECA-FR-94-12	
7. Author(s)  Gary Cheng		10. Work Unit No.	11. Contract or Grant No. NAS8-38868
9. Performing Organization Name and Address SECA, Inc. 3313 Bob Wallace Avenue, Suite 202 Huntsville, AL 35805		13. Type of Report and Period Covered Contractor - FINAL	
		14. Sponsoring Agency Code	
12. Sponsoring Agency Name and Address George C. Marshall Space Flight Center Marshall Space Flight Center, AL 35812			
15. Supplementary Notes  R. Garcia/Technical Monitor			
16. Abstract <p>Current design of high performance turbopumps for rocket engines requires effective and robust analytical tools to provide design information in a productive manner. The main goal of this study was to develop a robust and effective computational fluid dynamics (CFD) pump model for general turbopump design and analysis applications. A finite difference Navier-Stokes flow solver, FDNS, which includes an extended k-ε turbulence model and appropriate moving zonal interface boundary conditions, was developed to analyze turbulent flows in turbomachinery devices. In the present study, three key components of the turbopump, the inducer, impeller, and diffuser, were investigated by the proposed pump model, and the numerical results were benchmarked by the experimental data provided by Rocketdyne. For the numerical calculation of inducer flows with tip clearance, the turbulence model and grid spacing are very important. Meanwhile, the development of the cross-stream secondary flow, generated by curved blade passage and the flow through tip leakage, has a strong effect on the inducer flow. Hence, the prediction of the inducer performance critically depends on whether the numerical scheme of the pump model can simulate the secondary flow pattern accurately or not. The impeller and diffuser, however, are dominated by pressure-driven flows such that the effects of turbulence model and grid spacing (except near leading and trailing edges of blades) are less sensitive. The present CFD pump model has been proved to be an efficient and robust analytical tool for pump design due to its very compact numerical structure (requiring small memory), fast turnaround computing time, and versatility for different geometries.</p>			
17. Key Words (Suggested by Author(s))  turbopump, inducer flowfield		18. Distribution Statement  unclassified - unlimited	
19. Security Classif. (of this report) unclassified	20. Security Classif. (of this page) unclassified	21. No. of pages 71	22. Price